UNIVERSITÀ
DEGLI STUDI
FIRENZE

Scuola di Ingegneria

Dipartimento di Ingegneria Industriale (DIEF)

DOTTORATO DI RICERCA IN INGEGNERIA INDUSTRIALE

indirizzo "Energetica e Tecnologie Industriali ed Ambientali Innovative"

CICLO XXVI

S.S.D. ING-IND/09

Development of numerical tools for the analysis of advanced airblast injection systems for lean burn aero-engine combustors

PhD Candidate: Ing. Andrea Giusti

Tutor: Prof. Ing. Bruno Facchini

Academic Supervisor: Dr. Ing. Antonio Andreini

Industrial Supervisor: Ing. Fabio Turrini

PhD School Coordinator: Prof. Ing. Maurizio De Lucia

2011-2013

UNIVERSITÀ
DEGLI STUDI
FIRENZE

Scuola di Ingegneria

Dipartimento di Ingegneria Industriale (DIEF)

Dottorato di Ricerca in Ingegneria Industriale

indirizzo "Energetica e Tecnologie Industriali ed Ambientali Innovative"

CICLO XXVI

S.S.D. ING-IND/09

Development of numerical tools for the analysis of advanced airblast injection systems for lean burn aero-engine combustors

PhD Candidate: Ing. Andrea Giusti

Tutor: Prof. Ing. Bruno Facchini

Academic Supervisor: Dr. Ing. Antonio Andreini

Industrial Supervisor: Ing. Fabio Turrini

PhD School Coordinator: Prof. Ing. Maurizio De Lucia

2011-2013

chiudi gli occhi e prova a sognare,
se apri le braccia ti accorgerai che sai ancora
volare

close your eyes and try to dream,
if you open your arms you'll realize it's still possible
to fly

The research leading to these results has received funding from the European Union Seventh Framework Programme (FP7/2007-2013) under grant agreement n°265848 and was conducted within the FIRST (Fuel Injector Research for Sustainable Transport) project. The permission for the publication is gratefully acknowledged by the author. More information about the FIRST project can be found on the website: http://www.first-fp7project.eu/.

Quando si arriva alla fine di un percorso è bello fermarsi un po' a ricordare, ricordare da dove sei partito, guardarsi allo specchio e capire chi sei diventato... Il primo giorno di elementari, io e mio fratello, con quello zaino enorme ancora vuoto ma con tanta voglia di imparare e ancora prima seduto sul divano insieme a babbo che mi insegna a leggere i titoli di giornale. Mamma che mi accompagna a scuola e che mi ascolta mentre ripeto la lezione per l'interrogazione girando intorno al tavolino. Le corse per i campi per arrivare puntuale, i miei maestri di vita, tanta voglia di scoprire. E le superiori e quando mi arrabbiavo perché volevo imparare molto di più. E poi l'Università, gli amici che ho conosciuto, le persone che mi hanno aiutato a diventare grande.

È bello ricordare da dove sei partito, guardarsi allo specchio e capire chi sei diventato... sono sempre lo stesso, con la voglia di imparare e l'entusiasmo di quando ero bambino, con la serenità che la mia famiglia mi ha saputo dare e con lo zaino pieno di tutte le cose che ho imparato, che mi hanno insegnato.

Un grazie particolare ed estremamente sentito al Prof. Bruno Facchini, per tutto quello che mi ha dato in questi anni. Sento di aver ricevuto molto più di quanto sia riuscito a restituire, sarebbe bello un giorno poter ricambiare. Vorrei ringraziare allo stesso modo l'Ing. Antonio Andreini, la mia guida in questi anni di Dottorato, che mi ha permesso di avvicinarmi a tutte queste cose belle che qui vorrei raccontarvi, e molte altre ancora, rinnovando di giorno in giorno la mia voglia di conoscere e scoprire. Anche a lui voglio dire che avrei voluto dare molto di più. E poi l'Ing. Cosimo Bianchini stimolo continuo in tante discussioni. Gran parte del lavoro qui riportato è sicuramente frutto delle nostre conversazioni. Un ringraziamento speciale va all'Ing. Fabio Turrini, per i suoi sempre preziosi consigli tecnici, per i suggerimenti stimolanti, per avermi ricordato che siamo ingegneri, per aver scommesso su di me. Infine vorrei ricordare tutti i miei compagni di ufficio, persone veramente speciali. I calcoli lanciati fino a tardi, i fine settimana in mezzo ai miei numeri, li ricordo con il sorriso.

Preface

When I started my PhD I found very interesting to read an old paper [1], written in 1978, where the author tried to give an overview of the progress and the problems in aircraft combustor design with some recommendations for future research. In this picture of the future engine, liquid hydrocarbons were expected to continue to be the primary propulsion fuel, for reasons related to passenger security, weight and size of the engine, with some improvements in fuel flexibility. Lean burn operation of the combustor was recognized as one of the most effective solution to reduce luminous radiation, smoke problems and nitrogen oxide emissions. The success of the future engine was entrusted to the ability of designers to develop premixing and pre-vaporization techniques able to overcome problems related to flashback, preignition and fuel residence time. As regards combustor wall cooling, the concept of transpiration and the use of thermal barriers were recognized as the most interesting techniques for new generation engines. In these years much of the objectives outlined in this paper have been reached and at the same time, because of the more and more stringent regulations concerning pollutant emissions, new objectives have been introduced. However, with great surprise, some of the fields and technical strategies that were recognized as possible roads for future research are still active fields of investigation. Different final targets, which in most of the cases have become increasingly stringent, have been defined and new technical solutions have been proposed in order to overcome problems and limits not considered before that naturally arise during research in an unexplored field. Today, lean burn technology is considered one of the most effective solutions to meet low emission requirements with a lot of research efforts and investments to improve the use of this

technology in new generation aero-engines.

The research activity leading to the results presented in this work was carried out in the Heat Transfer and Combustion (HTC) group at the University of Florence, directed by Prof. Bruno Facchini and Dr. Antonio Andreini, where I worked during my PhD course. The HTC group has distinguished itself throughout the years for the research in the field of cooling and combustion systems for gas turbine applications. As far as aero-engines are concerned, the long-time collaboration with the industrial partner Avio Aero has allowed participation to the most important European research projects related to lean burn combustor design so that University of Florence can now be recognized as one of the most important contributors to the scientific and technical knowledge concerning lean burn technology development and application.

A quick picture of the most important research activities on aero-engine combustor design carried out in the recent years include experimental and numerical investigations on effusion cooling systems, which can be considered a practical implementation of transpiration cooling, evaluation of acoustic dissipation properties of multi-perforated liners, development of low-order models to be used in the combustor design. Great attention has also been devoted to the study of new solutions for the cooling of the first stage of the turbine which with the increase of the turbine inlet temperature has become one of the most critical components of the aero-engine.

The activities carried out during my PhD can be classified into two main topics that can be considered fundamental for the development of new generation lean burn aero-engine combustors. The engine emissions are strongly related to the combustion process and to the flame dynamics. Since liquid fuel are used, in order to properly predict the flame behaviour it is important to have reliable tools able to accurately describe all the processes related to fuel dynamics such as injection, primary and secondary atomization and evaporation. The first field explored in my research regards the development of numerical tools for the analysis of lean burn injection systems. This activity was performed within the framework of the European project called FIRST (Fuel Injector Research for Sustainable Transport, 7th framework programme) which aims at investigating physical phenomena related to primary atomization and soot formation and

at developing tools able to account for the complex processes that characterize advanced injection systems usually based on prefilming airblast configurations. This is the main subject of this dissertation. I do not want to disclose more things and I invite the reader to go through this document to understand the main aspects faced during this activity.

As said above, during the development of lean burn aero-engines new challenges have been met. One of them is undoubtedly related to the control of the so called thermoacoustic instabilities, that is unstable phenomena related to a coupling between the acoustic field and heat release fluctuations of the flame, which could become a critical issue when a combustor operates in the lean burn regime. The presence of such instabilities during the combustor operation may reduce the life of combustor components and even irreparably damage them with serious problems for the engine life and security of passengers. Thus, the development of proper tools able to predict the thermoacoustic behaviour of a lean combustor is of great interest for the the design of low emission engines.

The second topic faced during my PhD was the development of numerical tools for the thermoacoustic analysis of lean burn aero-engine combustors. The activity led to the building of a full model of an annular combustor [2]. Several aspects were deeply investigated ranging from definition of proper acoustic boundary conditions to the mathematical description of the relationship between heat release rate fluctuations and acoustic field. Models for the description of acoustic absorption properties of multi-perforated liners, typical of many aero-engine combustors, were evaluated and compared to experimental data collected during the KIAI (Knowledge for Ignition, Acoustics and Instabilities) European project. These models were also applied to the simulation of the full-annular combustor highlighting the stability effect induced by the presence of multi-perforated liners [3]. Formulations for the description of the coupling between flame dynamics and acoustics in a system equipped with a lean burn injection system were assessed [4] and new formulations and possible approaches to make the modelling more physically consistent [2, 5] were proposed following the developments of the LEMCOTEC (Low EMissions COre-Engine TEChnologies) European project. The analysis was performed considering a tubular combustor configuration for

which experimental measurements of pressure spectra at different operating conditions are available. Lastly, the transfer matrix modelling approach for the description of the injection system was introduced in the model developing a numerical strategy for the computation of the transfer matrix. These achievements will be the object of forthcoming publications.

The main problem in the thermoacoustic analysis of aero-engine lean burn combustors has been identified in the lack of proper tools capable of describing the coupling between the acoustic field and the flame heat release fluctuations which in aero-engines is further complicated by the presence of liquid fuels. Atomization, evaporation and in general the dynamics of droplets could interact with the acoustic fluctuations acting as a driving mechanism for combustion instabilities. In order to make the contents more homogeneous, the results obtained in the thermoacoustic research will not find space in this dissertation and the interested reader is addressed to the references indicated above to find out more.

Before starting my dissertation, I would like to express my gratitude to Prof. Bruno Facchini and Dr. Antonio Andreini for offering me the possibility to give my contribution in this exciting research field and for allowing me to participate to the European Projects and many other activities. I think that all these experiences have allowed me to be a better engineer and a better man. Then, I also would like to thank all the partners and the people involved in the FIRST project for their scientific and financial support, for all the things I learnt during this project. The value of this experience is really invaluable. Last but not least, I would like to remember Eng. Fabio Turrini, Technical Manager of Combustors Product Engineering at Avio Aero. I think that when research is performed in the engineering field the final target, that is the application in a technical system, should never be forgotten. Therefore, I would like to thank him for the coordination of the work and technical advices received in many discussions we had throughout these years.

I don't want to bore you anymore, it's time to start!

Florence,
28th November 2013

Abstract

The liquid fuel preparation has a strong impact on the combustion process and consequently on pollutant emissions.However, currently there are no validated and computational affordable methods available to predict the spray breakup process and to reliably compute the spray distribution generated after primary breakup. This research activity, carried out within the framework of the European project FIRST (Fuel Injector Research for Sustainable Transport), is aimed at developing reliable tools to be used in the industrial design process able to describe the processes involved in liquid fuel preparation in advanced injection systems based on prefilming airblast concept.

A multi-coupled solver for prefilming airblast injectors which includes liquid film evolution and primary breakup was developed in the framework of OpenFOAM. The solver is aimed at improving the description of the complex physical phenomena characterizing liquid fuel preparation and spray evolution in advanced airblast injection systems within the context of typical RANS (U-RANS) industrial calculations. In this kind of injectors, gas-phase, droplet and liquid film interact with each other, thus, in order to properly predict spray evolution and fuel distribution inside the combustor, proper tools able to catch the most important interactions among the different phases are necessary. A steady-state Eulerian-Lagrangian approach was introduced in the code together with up-to-date evaporation and secondary breakup models. Particular attention was devoted to the liquid film primary breakup and to the interactions between gas-phase and liquid film. A new primary breakup model for liquid films, basically a phenomenological model which exploits liquid film and gas-phase solutions for the computation of spray characteristics after breakup, was developed and implemented in the code. Different

formulations for the computation of droplet diameter after breakup were evaluated and revised on the basis of recent experimental findings. The multi-coupled solver was validated against literature test cases with detailed experimental measurements and eventually applied to the simulation of an advanced prefilming airblast injector based on the PERM concept in a tubular combustor configuration.

The proposed approach allows us to better describe the fuel evolution in the injector region leading to a more comprehensive and physically consistent description of the phenomena regulating liquid fuel preparation compared to standard approaches which neglect the presence of liquid film and its interaction with both droplets and gas-phase.

Contents

Nomenclature

Symbols

AFR	Air-fuel ratio
Bi	Biot number
B_M	Spalding mass transfer number
C_D	Drag coefficient
$\mathscr{D}$	Mass diffusivity, m^2/s
D	Reference diameter, m
d	Droplet diameter, m
	Diameter, m
FAR	Fuel-air ratio
G	Group combustion number
h	Atomizing edge thickness, m
h_s	Sensible enthalpy, J/kg
h_t	Total enthalpy, J/kg
h_v	Latent heat of vaporization, J/kg
K_S	Equivalent sand-grain roughness, m
k	Turbulence kinetic energy, m^2/s^2
	Thermal conductivity, W/(m K)
k_v	Constant in the d^2-model, m^2/s
	Velocity constant
L	Length, m
La	Laplace number
Le	Lewis number
L_k	Knudsen layer thickness, m
m	Mass, kg
Nu	Nusselt number
Oh	Ohnesorge number

Pr	Prandtl number
p	Static pressure, Pa
q	Parameter in the Rosin-Rammler distribution
Re	Reynolds number
R_{ND}	Dimensionless surface roughness
r	Droplet radius, m
	Radial coordinate, m
S_A	Axial penetration, m
S_N	Normal penetration, m
S_R	Radial penetration, m
Sc	Schmidt number
Sh	Sherwood number
SMD	Sauter Mean Diameter, m
St_v	Stokes number
T	Temperature, K
t	Time, s
U	Velocity magnitude, m/s
V	Depth-averaged velocity, m/s
W	Molecular weight, kg/kmol
We	Weber number
X	Parameter in the Rosin-Rammler distribution, m
Y	Mass fraction
y	Droplet deformation
Z	Mixture fraction

Greek symbols

α_P	Volume fraction
Δh_f^0	Mass formation enthalpy, J/kg
δ	Film thickness, m
ε	Turbulence kinetic energy dissipation, m^2/s^3
Θ	Ratio of gas and fuel molecular weights
Λ_f	Film load, m^2/s
λ	Liquid thermal conductivity, W/(m K)
	Wavelength, m
μ	Dynamic viscosity, kg/(m s)
ν	Kinematic viscosity, m^2/s

ρ	Density, kg/m^3
σ	Surface tension, N/m
τ_v	Dynamical relaxation time, s
χ	Molar fraction
ω	Rate of turbulence kinetic energy dissipation, 1/s
	Angular frequency of oscillations, 1/s

Vectors

$\mathbf{F}$	Force acting on a particle, N
$\mathbf{g}$	Gravity acceleration, m/s^2
$\mathbf{n}$	Outward normal vector
$\mathbf{u}$	Gas-phase velocity, m/s
$\mathbf{V}$	Depth-averaged film velocity, m/s
$\mathbf{v}$	Particle velocity, m/s
$\boldsymbol{\tau}$	Shear stress, N/m^2

Subscripts

0	Initial value
b	Breakup
c	Critical
d	Droplet
eq	Equilibrium
ev	Evaporation
F	Fuel
f	Film
fs	Free surface
g	Gas-phase
I	Impact
imp	Impingement
in	Inlet
inj	Injector, injection
j	Jet
L	Liquid
lig	Ligament
lv	Liquid viscosity

max	Maximum value
n	Normal
neq	Non-equilibrium
opt	Optimal
P	Particle
p	Parcel
R	Relative (between gas-phase and particles)
ref	Reference value
S	Surface
sat	Saturation
$strip$	Stripping
t	Tangential
$turb$	Turbulent
v	Vapour
w	Wall
z	Axial
∞	Far away from the droplet

Miscellaneous

$\widetilde{(\bullet)}$	Frave-averaged quantity
$\overline{(\bullet)}$	Reynolds-averaged quantity
$(\bullet)'$	Fluctuation over the mean quantity
$(\bullet)''$	Fluctuation over the Favre-averaged quantity
$\Gamma(\bullet)$	Gamma function
$\|\|(\bullet)\|\|$	Magnitude of a vector
$\dot{(\bullet)}$	First time derivative
$\ddot{(\bullet)}$	Second time derivative
$\Delta(\bullet)$	Difference

Acronyms

CAB	Cascade Atomization Breakup
DES	Detached Eddy Simulation
EDC	Eddy Dissipation Concept
ETAB	Enhanced TAB

FIRST	Fuel Injector Research for Sustainable Transport
LES	Large Eddy Simulation
MCAB	Modified CAB
PDF	Probability Density Function
PERM	Partially Evaporating and Rapid Mixing
RANS	Reynolds Averaged Navier-Stokes
RMS	Root Mean Square
TAB	Taylor Analogy Breakup
U-RANS	Unsteady RANS
VOF	Volume Of Fluid

Introduction

Context and significance of the present research

Because of the increasingly stringent regulations on pollutant emissions, in particular NO_x (see ICAO-CAEP standards and ACARE Vision 2020 objectives [6]), in the last years aero-engine manufacturers have increased their efforts in the research and development of effective solutions for emissions abatement. The most critical component for the development of an environmentally-friendly engine is undoubtedly the combustor, the device into which the combustion process takes place and therefore the main responsible for pollutant emissions.

In aero-engine combustors the main contribution to NO_x emissions is given by the so called thermal NO_x which have an exponential dependence on temperature. Therefore the reduction of nitrogen oxide emissions requires the limitation of temperature in the combustion region which can be obtained through a careful control of the air-fuel mixture quality. Even though classical RQL technology has still relevant improvement potentials, with the expected next NO_x reduction targets lean combustion technology can be considered the most effective solution for modern gas turbines to meet emission requirements and allow a heavy reduction of nitrogen oxide emissions.

In lean burn combustion, the reduction of NO_x emissions is achieved by burning the fuel in lean conditions. In principle, if a lean homogeneous mixture is used, temperatures in the flame region can be drastically reduced compared to the values encountered in diffusion flames, where the fuel locally burns close to stoichiometric mixture. Since in the current vision of aircraft engine development, for reasons mainly related to safety and operability, liquid fuel still remains the main energy source, all the aspects related to liquid fuel

preparation and air-fuel mixing are critical aspects for the development of a lean burn combustors. The formation of a homogeneous mixture can be obtained only through a proper design of the injection system, therefore a significant portion of the research works in the lean combustion field is devoted to the development of advanced injectors able to control the quality of liquid fuel preparation and to promote a rapid mixing between air and fuel so that the combustion process can be moved towards lean premixed flames.

Many of the injection systems proposed in the recent years are based on prefilming airblast configurations. In this kind of injectors the fuel is spread out into a thin, continuous sheet which is driven along a prefilming surface by a co-flowing air stream until the atomizing edge is reached and primary atomization occurs. Droplets generated by the film breakup evolve inside the combustion chamber where the evaporation process and interactions with the gas-phase lead to the formation of the air-fuel mixture which eventually enters the combustion region. As a consequence a combustor equipped with prefilming airblast injectors is characterized by the presence of three distinct phases (gas-flow, liquid film and droplets) which interact with each other determining the global behaviour of the combustion process. Furthermore, in some injector configurations [7, 8] the liquid film could be generated by impinging droplets making the phenomena related to the interaction between droplets and wall/film important aspects to be considered for a reliable prediction of liquid fuel preparation. This could also be the case of the so called piloted airblast atomizers where a pilot injector is placed at the center of the airblast system and droplets injected through the pilot injector could impact the liquid film [9]. An example of aero-engine combustor equipped with an advanced piloted airblast injector is reported Fig. 1 together with a schematic representation of the most important phenomena regulating liquid fuel preparation in this kind of injection systems: the prefilming airblast configuration is coupled with a pressure atomizer (piot injector) and droplets injected through the pressure atomizer could reach the prefilming surface interacting with the liquid film.

Numerical methods and in particular CFD are widely used in the industrial design process, however available tools are not able to completely describe all the phenomena regulating liquid fuel preparation and evolution, in particular the complex interactions between

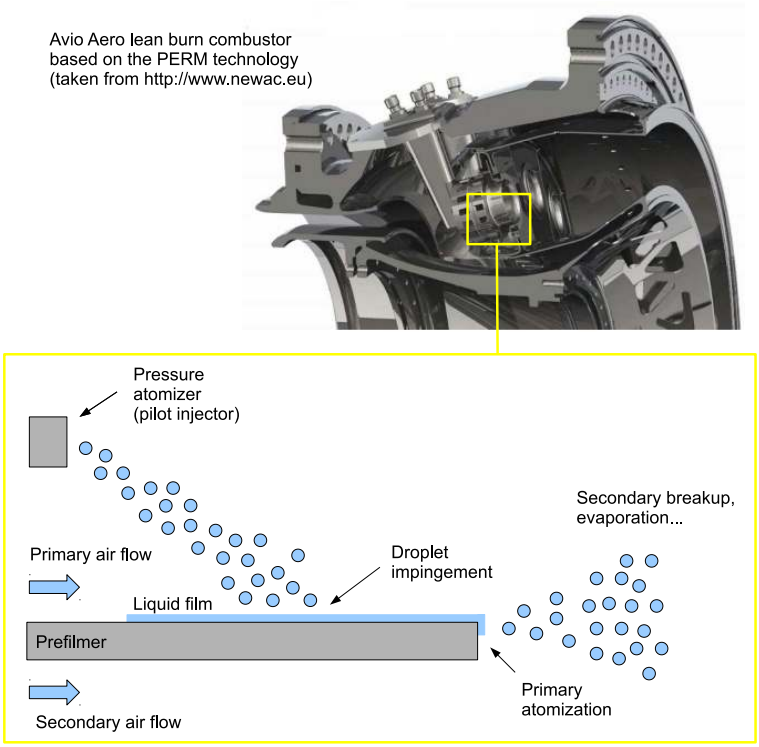

Figure 1: Schematic representation of a piloted airblast injection system.

droplets, liquid film and gas-phase, that characterize systems equipped with advanced prefilming airblast injectors. In order to appreciate the complexity of the phenomena encountered in aero-engine combustion scenarios, Fig. 2 shows a coarse sketch [10] of the most important interactions that can be found in turbulent spray flames generated by prefilming airblast injectors. The representation is not exhaustive and other interactions could be added to this sketch, however it is sufficient to demonstrate the strong coupling between the different phenomena. It goes without saying that a proper prediction of the performance of an aero-engine combustor and a reliable prediction of engine emissions require proper tools able to catch the most im-

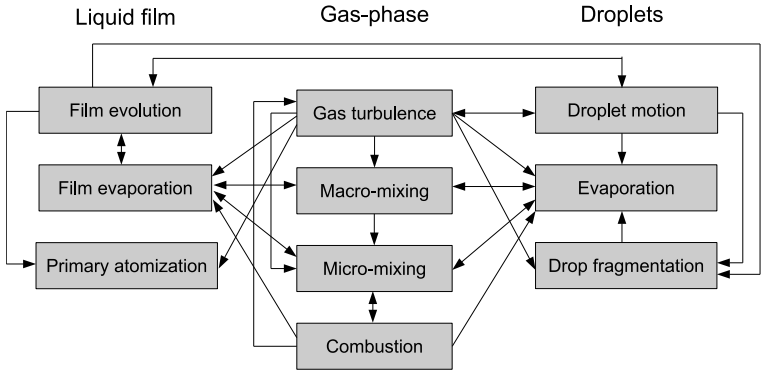

Figure 2: Interactions among gas-phase, droplets and liquid film in combustors equipped with prefilming airblast injectors (adapted from [10]).

portant interactions among the different phases. However, a detailed and accurate description of all the phenomena is usually not practicable in typical industrial approaches without the introduction of assumptions and simplified models.

Typical industrial computations of aero-engine combustors are usually performed using an Eulerian-Lagrangian approach [11] where the gas-phase is modelled in the Eulerian framework whereas the liquid fuel is predicted using a Lagrangian description. The gas-phase solution is usually obtained using the RANS approach where only the mean flow is solved and the turbulence effects on the mean field are reproduced using proper turbulence models. It should be noted that advanced time-resolved approaches for gas-phase simulation such as DES and LES, able to better describe the complex flow structures that characterize the flow field of typical combustion chambers [12, 13], could also be used. These approaches have demonstrated to be capable of properly predicting the most important flow structures and the interactions between gas-phase and Lagrangian droplets [14, 15], however they are still characterized by a very high computational cost to be extensively used in an industrial design process. Therefore, even though LES simulations are increasingly being used within the combustor design to investigate details of the

flow field, RANS simulations are expected to remain the main development tool for a long time and thus the improvement of RANS approaches is still of great interest. Another important issue in CFD simulations is related to the combustion modelling. The combustion process is a very complex phenomenon involving many intermediate species and interactions with turbulence and liquid phase. In order to reduce the computational effort, in industrial computations reduced chemical schemes with additional simplifying assumptions are usually adopted.

As regards the simulation of the Lagrangian phase, efficient models for the description of interactions between droplets and gas-phase have been developed throughout the years [16, 10]. However, in industrial calculations the primary atomization of the liquid fuel is not usually included in the simulation and droplet population generated by the primary breakup is assigned as a boundary condition [11, 17, 15, 14]. Because of the lack of detailed experiments and a comprehensive theory on primary atomization, the characteristics of droplet population imposed in the simulations are usually characterized by a high level of uncertainty which could not be tolerable in the design of modern lean burn combustors because the corresponding uncertainty in the prediction of combustor emissions is often of the same order of magnitude of the desired improvements. Furthermore, in the context of prefilming airblast injection systems, typical industrial computations [18, 19, 17] usually neglect the presence of the liquid film and its possible formation due to the interaction between droplets and solid walls, and droplets generated by the liquid film are simply introduced in the computational domain by means of an equivalent injector placed at the atomizing edge of the airblast system. This approach has several weaknesses and drawbacks:

- the interaction between liquid film and droplets is not considered: if droplets are absorbed by the liquid film, an additional fuel mass flow should be injected through the airblast atomizer;
- the characteristics of droplets generated by the liquid film atomization are imposed by the user and do not depend on the liquid film evolution over the prefilming surface disregarding, for example, changes in temperature due to heat transfer with solid walls as well as liquid film pre-vaporization which could

alter the fuel mass fraction distribution near the injection system;

- no general and common rules are used to impose the particle injection velocity.

Therefore, a proper representation of the liquid film evolution and its interactions with the other phases should be included in the simulation since they could have a great impact on both droplet evolution and combustion process [20, 21].

It should be noted that advanced approaches for the numerical simulation of liquid film evolution, primary breakup and droplet-film interactions could also be used. Many of them are based on methods, such as VOF/level-set, able to resolve the interface between liquid and gas-phase so that the complex unstable phenomena characterizing primary atomization and droplet impact can be directly simulated [22, 23, 24]. A very interesting approach is the one proposed in [25] where an embedded VOF method is used to predict the liquid film primary breakup and the characteristics of droplet population generated by the film fragmentation. The droplet population predicted in this way is then used as an input for a spray solver. The method is very interesting but it still requires improvements in order to give reliable predictions. Furthermore, in general, techniques aimed at resolving the interface between liquid film and gas-phase require very high mesh resolutions and advanced numerical methods so that they are characterized by a very high computational cost to be used in complex realistic configurations or more in general in an industrial design process [8]. However, if reliable correlations or models for the computation of the SMD of droplets generated by the airblast atomizer are not available, the VOF and related approaches could be interesting tools to numerically determine the main characteristics of droplet population generated by the primary breakup which could be exploited in simpler numerical approaches.

Considering the previous observations, it is clear that in the current application of CFD tools to industrial simulations of lean burn aero-engine combustors, the main uncertainty is related to the description of liquid fuel preparation and to the prediction of the characteristics of droplet population generated after primary breakup. The development of advanced combustion models and methods for

the gas-phase solution is still an important issue, however before developing efficient tools for the description of spray combustion, the prediction of liquid fuel preparation should be improved since it inevitably influences all the combustion process. Therefore, in order to improve the understanding of the physical mechanisms regulating the breakup process and more in general the reliability of industrial computations of aero-engine combustors, it is of great importance to develop proper tools able to better describe all the processes involved in liquid fuel preparation.

Objectives and present contributions

The main objective of this research is the development of numerical tools able to include in typical industrial computations based on RANS (U-RANS) approaches the most important physical processes characterizing the behaviour of advanced prefilming airblast injection systems in order to improve the reliability of the prediction of liquid fuel preparation. In particular, all the following phenomena have to be considered in the simulation:

- liquid film evolution over the prefilming surface;
- liquid film primary breakup;
- interaction between liquid film and droplets;
- interaction between liquid film and gas-phase.

Furthermore, great attention should also be devoted to the phenomena characterizing spray evolution and interactions with the gas-phase which could have an important effect on fuel distribution inside the combustion chamber. Since numerical tools are intended to be used in an *industrial* design context, the *computational cost* is an important aspect to be considered and therefore numerical approaches able to guarantee a good compromise between computational cost and reliability of the representation of the physical phenomena have to be selected.

Keeping in mind these aspects, a multi-coupled Eulerian- Lagrangian solver for reacting sprays including liquid film evolution and primary breakup was developed in the framework of the open source

code OpenFOAM starting from numerics and models implemented in the Version 2.0 of the code. The solver allows the main interactions among liquid film, gas-phase and disperse phase to be considered. Liquid film solution is based on the thin film approximation. Similar approaches in the past have been used to study the liquid film formation in internal engines [26] but applications to aero-engines and in particular to real prefilming injection systems are very limited. Thus, in this work the capabilities of such approaches in the prediction of liquid film evolution in gas turbine applications are assessed and evaluated. Furthermore, a specific primary atomization model for liquid films was introduced in the formulation. This is basically a phenomenological approach which exploits liquid film solution for the computation of injection mass flow rate and velocity and experimental correlations or theoretical models for the computation of droplet diameter so that a more reliable representation of the droplet population generated by the airblast injector can be obtained. In order to reduce the computational cost and to make the approach more suitable for industrial computations, a steady-state formulation of the solver was introduced in the code. Furthermore, spray interaction models were updated implementing recent models and formulations. This is the case, for example, of evaporation models and secondary breakup models. The developed models were validated using literature testcases and eventually applied to the simulation of an advanced airblast injection system in a tubular combustor configuration with the main aim of showing the improvements that can be obtained in the description of liquid fuel preparation in comparison with standard industrial approaches which neglect the presence of the liquid film.

As will be more clear during the dissertation, each class of injection systems is characterized by specific atomization mechanisms which depend on both geometrical configuration and operating conditions. In this research, a prefilming airblast injector developed by Avio Aero and based on the PERM (Partially Evaporating and Rapid Mixing) concept was taken as reference in the derivation and validation of numerical models. However, the use of the developed tools is not limited to this particular injector. Numerical models and solvers introduced in this research can be applied not only to similar injection systems but also in different classes of problems where interactions among gas-phase, liquid film and droplets are important aspects for

the description of the physical behaviour of the case under consideration.

The work leading to the results presented in this dissertation was carried out in the framework of the European project called FIRST (Fuel Injector Research for Sustainable Transport) which is mainly devoted to the study of primary atomization in configurations close to aero-engine injection systems and to the development of numerical models for the analysis of advanced injection systems.

Thesis outline

During this research activity the aspects related to liquid fuel preparation and spray evolution were analysed from both theoretical and numerical points of view. The main achievements are related to the development, implementation and validation of numerical tools suitable for industrial calculations of systems equipped with prefilming airblast injection systems. However, since the development of numerical models in strongly connected to the physics of the phenomena that have to be represented, in this thesis the description of numerical modelling will be generally supported with a comprehensive description of the physical processes involved in the simulation in order to make more clear the reasons that led to the choice of particular modelling strategies. The dissertation will be organized as follows.

Chapter 1. In order to better explain the context into which the numerical tools have been developed, low emission engines and lean burn technology are presented. The PERM injection system, used as reference in the derivation of the models developed in this research, is introduced in this chapter.

Chapter 2. Before describing the numerical models introduced in this research, the basic concepts of liquid fuel preparation will be presented. The main aim of this chapter is to give an introduction to primary and secondary atomization identifying the most important parameters for the description of these phenomena and the spray population generated after atomization. Phenomena related to droplet impingement will be also discussed.

Chapter 3. Numerical models used for the representation of spray dynamics in the context of Eulerian-Lagrangian simulations will be described. Different evaporation and secondary breakup models will be introduced and assessed by means of simulations of specific test cases. Particular attention will be devoted to the presentation and validation of a steady-state solver for reacting sprays developed during the research activity. Validation has been performed using literature test-cases for which experimental measurements for both gas-phase and droplet population are available.

Chapter 4. Liquid film modelling and interactions between liquid film and the other phases are introduced in the spray solver described in the previous chapter leading to the development of a multi-coupled approach (film, gas-phase, droplets) for the simulation of prefilming airblast injectors. This chapter is mainly devoted to the presentation of the implemented approach and to the validation of the film solver through literature test-cases reproducing the main interactions characterizing typical prefilming airblast injectors used in aero-engine applications. A first investigation about the development of liquid film in a PERM injector is also presented.

Chapter 5. Liquid film primary atomization modelling is the main subject of this chapter. The primary breakup model developed in this research is described with great detail giving more insight into the atomization mechanisms observed in recent experiments on prefilming airblast injectors. The developed model has been assessed and validated using experimental measurements performed in a PERM injection system at atmospheric conditions using water.

Chapter 6. The application of the developed numerical tools to the simulation of a PERM injection system in a tubular combustor configuration at different operating conditions is presented. In order to show the improvements in the description of liquid fuel preparation obtained with the multi-coupled approach introduced in this research, results obtained with the developed solver will be compared with numerical simulations performed with the standard industrial approach which neglects the presence of the liquid film and introduces the droplets generated by the liquid film atomization through a user-

defined injector placed at the atomizing edge. A detailed analysis of the effects of film modelling in both gas-phase and spray evolution is presented.

Chapter 7. A summary of the main achievements of this research is given together with conclusions and recommendations for future research.

Chapter 1

Technical background

This research activity is mainly focused on the development of numerical tools for the description of liquid fuel preparation in advanced airblast injection systems for lean burn aero-engine combustors. Before describing in detail the most important aspects related to liquid fuel atomization and spray evolution and the characteristics of the developed models, a preliminary introduction to aero-engine combustors is presented with particular attention to lean burn technology and typical injection systems used in lean burn aero-engines in order to give a picture of the technical context into which the research was carried out and the developed tools will be applied.

1.1 Low-emission combustors

The development of combustors for the next generation of aero-engines is mainly driven by the demand for low emission requirements, in particular NO_x (see ICAO-CAEP standards, Fig. 1.1, and ACARE Vision 2020 objectives [6]), which has to be satisfied together with the requirements for low pressure losses, high combustion efficiency, low weight and compact design [11], typical of aero-engine combustors. It is important to note that, in order to reduce the fuel consumption and thus CO_2 emissions, the future engine will be characterized by a further increase of operating pressure ratio and turbine inlet temperature. The current target for the European aviation is the development of Ultra High Pressure Ratio (UHPR) gas turbines, that

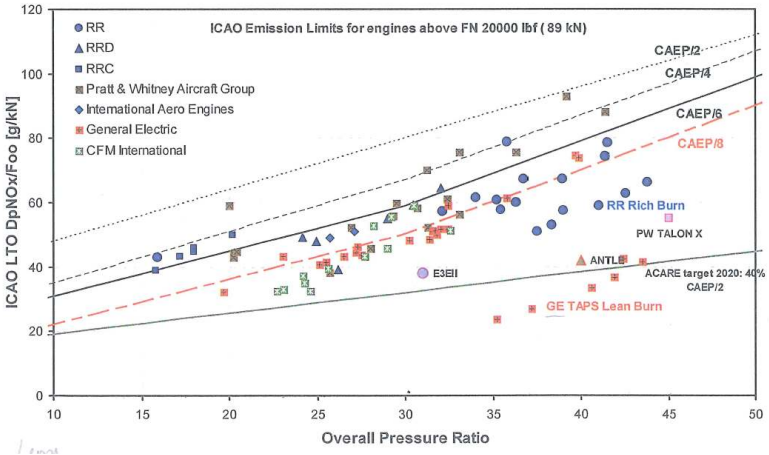

Figure 1.1: NO_x emission limits as a function of the take-off overall pressure ratio (taken from [13]).

is engines characterized by pressure ratios up to 70 [27]. However, the high pressure ratio together with the increase of the turbine inlet temperature would lead to an enhancement of NO_x emissions making the reduction of NO_x even more challenging.

Several factors could contribute to NO_x emissions, however in typical aero-engine combustors the formation of nitrogen oxides is mainly caused by high temperatures through the contribution of the so called thermal NO_x. According to the Zeldovich mechanism, the formation of thermal NO_x has an exponential dependence on temperature [28] and thus they are mainly produced in the vicinity of stoichiometric conditions where the flame reaches the maximum temperatures. Therefore, the limitation of NO_x emissions requires the reduction of temperatures in the combustion region and can be obtained through a careful control of the air-fuel mixture quality in order to move the local flame structure far away from stoichiometric conditions. As also shown in Fig. 1.2, in principle there are two possible operation zones to reduce NO_x, the rich burn and the lean burn modes. In the following, different strategies used in technical applications to limit pollutant emission will be presented. Regardless of the adopted strat-

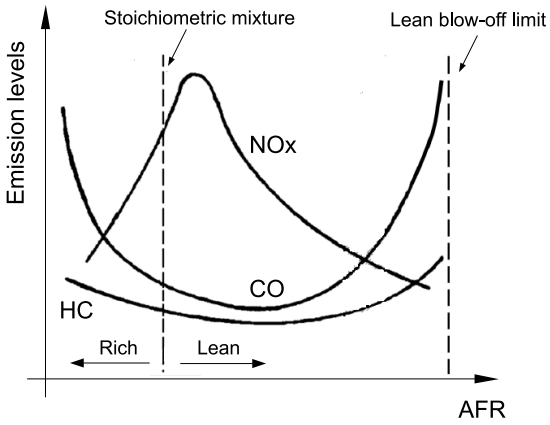

Figure 1.2: Dependence of NO_x on fuel-air ration.

egy, the combustor design has to ensure that stoichiometric condition is avoided as much as possible in all operating conditions [11].

1.1.1 RQL combustion

Most of the combustors used in aero-engine applications are usually based on the RQL (rich-burn, quick-quench, lean-burn) concept where both rich burn and lean burn modes are exploited. This technology can be considered the state of the art for aero-engine combustors. RQL combustors are characterized by a fuel rich primary zone (i.e. the region close to fuel injection), where NO_x formation rates are low due to the combined effects of low temperature and oxygen depletion [28], followed by a quenching zone and a lean burn region where the combustion is completed in lean conditions. The underlying principle behind the RQL combustor concept is illustrated in Fig. 1.3. In order to avoid the formation of stoichiometric mixture, the passage from rich to lean conditions should be very quick. Thus, the design of a rapid and effective quick-quench mixing section is of decisive importance to the success of the RQL concept.

Fig. 1.4 summarizes the main characteristics of a combustor based on the RQL technology. As discussed in [29], the rich zone provides

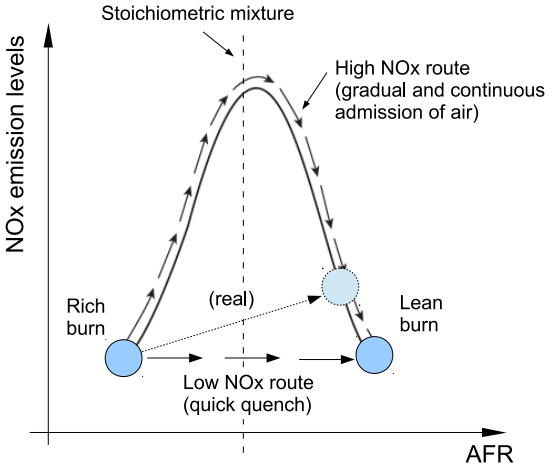

Figure 1.3: Principle of RQL combustion (adapted from [28]).

a high level of resistance to flame out, keeping the combustor alight at low power conditions where the combustor overall is running very lean. Furthermore, a proper design of dilution holes enables most of the soot produced in the rich zone at high power to be consumed. The most critical part of the combustor is the quenching zone. In the passage from rich to lean conditions, there will always be regions of the combustor where stoichiometric conditions could be reached. It is important to minimize the time spent by the mixture in these regions.

It is worth noting that some innovative configurations proposed in the recent years, such as the Pratt & Whitney TALON X combustor [30], where the quenching region is characterized by an improved design in order to optimize the mixing between dilution air and combustion products coming from the rich primary region, have demonstrated a good potential for NO_x reduction.

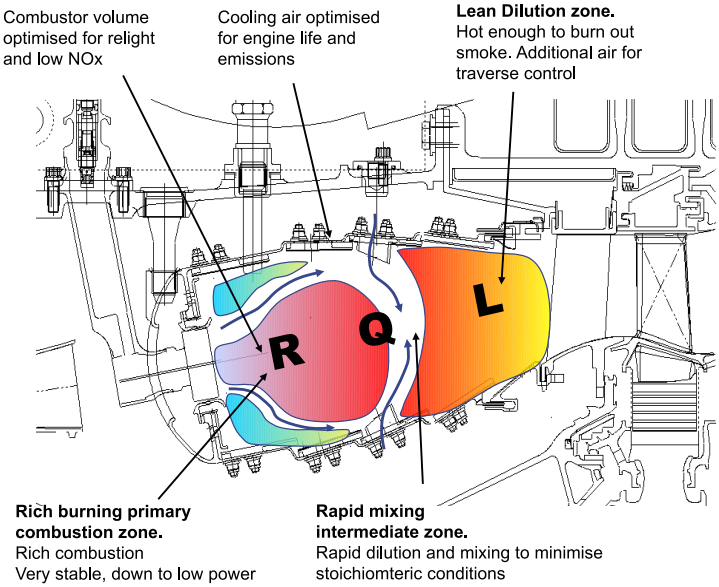

Figure 1.4: Main characteristics of a combustor based on the RQL concept (adapted from http://www.newac.eu).

1.1.2 Lean burn combustion

Even though classical RQL technology has still some improvement potentials, with the expected next NO_x reduction targets, the development of innovative combustion systems based on the so called lean burn combustion technology appears inevitable. Lean burn combustion can be considered the most effective solution for modern gas turbines to meet emission requirements and allow a heavy reduction of nitrogen emissions. As a consequence, in the recent years the most important manufactures have increased their efforts and investments in research projects aimed at making lean combustion a safe and efficient technology for aero-engines.

In lean burn combustors the reduction of NO_x emissions is achieved by burning the fuel in lean conditions and therefore lean combustion systems operate with an excess of air in the combustor primary

region. In order to avoid the formation of diffusion flames where the fuel locally burns at stoichiometric conditions, fuel and air should be accurately mixed before entering the combustion zone. Historically, lean burn combustion was firstly developed and successfully applied in gas-turbines for land applications. However the specific technologies developed for land-based applications, where gaseous fuel is used, cannot be directly exploited in aero-engine applications because of the presence of liquid fuel which further complicates the formation of a homogeneous mixture. Therefore new technologies have to be developed in order to ensure a careful control of liquid fuel preparation and a proper mixing of fuel with air.

A very promising technique to obtain an efficient air-fuel mixing is represented by Lean Premixed Pre-vaporized (LPP) systems where the liquid fuel is completely evaporated and mixed with air before entering the combustion chamber. This technology, in principle, has the greatest potential for NO_x reduction since allows the formation of a highly homogeneous air-fuel mixture. However, because of the inherent risks for flash-back and auto-ignition, especially at high operating pressures, LPP fuel preparation devices cannot be safely used at the operating conditions of typical aero-engine combustors [11] and therefore the current attention has been moved on to systems based on a direct injection of the fuel into the combustion chamber.

The injection system can be considered one of the most important component for the performance of a lean combustor. The aspects related to liquid fuel atomization, spray evolution and evaporation are important issues for the success and application of lean burn technology and therefore a significant portion of the research works in the lean combustion field is devoted to the development of advanced injectors able to control the quality of liquid fuel preparation and to promote a rapid mixing between air and fuel so that the combustion process can be moved towards lean premixed flames.

Injection configurations should be able to control both the quality of atomization and the characteristics of flow structures in the combustor primary region in order to generate a highly homogeneous air-fuel mixture and to ensure a proper stabilization of the combustion process. Differently from RQL combustors where the rich primary zone makes the combustion process intrinsically more stable, lean burn combustors operate near the lean blow-out limits and therefore

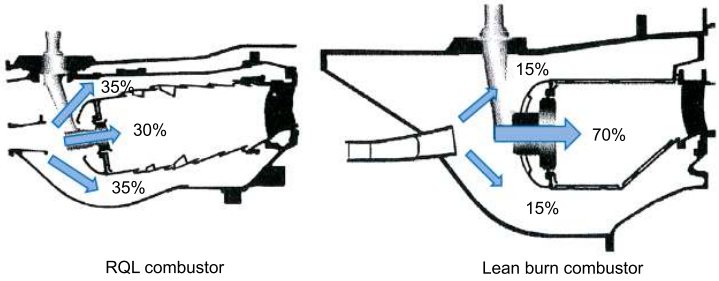

Figure 1.5: Typical air flow split in RQL and Lean Burn combustors.

proper strategies for flame stabilization should be adopted.

Fig. 1.5 shows a comparison between typical air flow split in RQL and lean burn combustors. In lean burn systems up to 70% of the air discharged by the compressor is used in the primary region and it is directly supplied through the injection system. Since for reasons mainly related to flame stabilization and limitation of the pressure drop across the injection system the velocity of the air flow entering the combustion chamber should remain unchanged, lean burn injection systems are characterized by a significant increase in the physical size with respect to typical injectors used in rich burn combustors. Furthermore, because of the small amount of air available for wall cooling, lean combustor liners do not usually have any additional mixing port downstream of the fuel injector and all the air-fuel mixing should be accomplished by the flow structures generated by the injection system. Therefore, the aerodynamic design of the injector is of paramount importance for the performance of lean burn systems.

It should be noted that air flows in the primary region of the combustor are not only useful for atomization and mixing but they also contribute to the stabilization of the combustion process. Flame stabilization in lean burn combustors is usually based on the formation of a swirl stabilized recirculation region [13, 31]. Therefore, in typical injector configurations the air passages usually consist in inclined channels able to generate a proper swirl component in the air flow. Advanced injection systems used in lean burn applications are usually based on the combination of multiple swirl passages in

order to satisfy the requirements for both high quality atomization and mixing and flame stabilization in the combustion region.

It is important to note that lean conditions in the primary region together with the rapid air-fuel mixing requirements could have an adverse effect on ignition, altitude relight and flame stabilization at low power [11]. Therefore, in order to achieve the full operability, lean burn combustors are usually equipped with piloting devices which generate moderately rich flames able to stabilize the combustion process, especially at low power conditions. Typical injection systems used in lean burn applications are usually based on an internally staged configuration where the pilot device and the lean burn main stage are arranged in the same configuration in order to have a very compact design. Fuel split between pilot and main stage as well as the particular staging strategy usually depend on the operating condition and the geometrical characteristics of the injection system.

Fig. 1.6 summarizes the most important characteristics of a combustor based on the lean burn technology whereas in Fig. 1.7 an internally staged lean burn injection system is compared with a typical injector used in RQL combustors. It is possible to note the difference in size between the two injectors with the lean burn system characterized by a greater dimension due to the large amount of air requested in the combustor primary region.

1.2 Injectors for aero-engine applications

In aero-engine applications, and in particular in lean burn combustors, a high quality atomization, where the liquid stream is disintegrated into fine droplets, is usually requested in order to promote a rapid fuel evaporation and mixing with the air flow. The atomization process requires the presence of a force, or more in general a physical interaction, able to disintegrate the bulk fuel into small droplets. Different types of injectors can be distinguished depending on the basic physical mechanism used to generate this disruptive force. Basically, two different types of injectors are used in aero-engine applications:

- pressure atomizers;
- airblast atomizers.

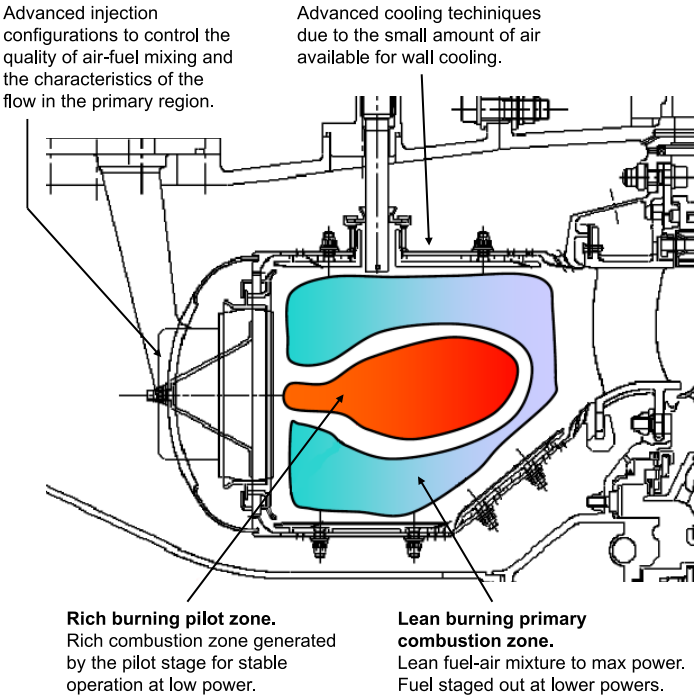

Figure 1.6: Main characteristics of a combustor based on the lean burn technology (adapted from http://www.newac.eu).

The atomization process in this kind of injectors is based on the same principle: the liquid stream and the gas-phase interact with each other with a high relative velocity which generates strong aerodynamic interactions leading to the fragmentation into droplets. In pressure atomizers a high velocity jet or sheet is injected into a low velocity medium whereas in airblast atomizers the liquid is subjected to a high velocity air-stream. Other types of injectors can also be found in technical applications, such as rotary atomizers, effervescent, ultrasonic, electrostatic injectors and many others. A detailed description of them with their advantages and drawbacks can be found in Lefebvre [32]. In the following, the basic concepts of fuel injection

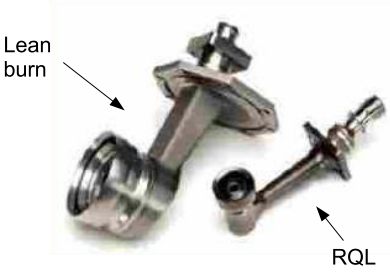

Figure 1.7: Comparison between lean burn and RQL injectors.

in pressure and airblast atomizers will be firstly presented, then the PERM injector, the reference configuration in this research, and other advanced injection systems suitable for lean burn applications will be introduced.

1.2.1 Pressure atomizers

Pressure atomizers are based on the conversion of pressure into kinetic energy to achieve a high relative velocity between the fuel and the surrounding gas. Various atomizers are based on this concept. The simplest configuration is the *plain orifice* (see Fig. 1.8) where the fuel is injected through a small aperture. Disintegration of the jet is promoted by an increase in fuel-injection pressure, which increases both the level of turbulence in the fuel jet and the aerodynamic forces exerted by the surrounding medium.

In order to improve the quality of the atomization, the so called *pressure-swirl* atomizer has been developed. In this injector, a swirling motion is imposed to the fuel in a swirling chamber so that, under the action of centrifugal forces, it spreads out in the form of a conical sheet as it leaves the orifice. The basic form of pressure-swirl atomizer is the *simplex* atomizer where the fuel is fed into a swirl chamber through tangential ports that give to the liquid a high angular velocity creating an air-cored vortex. The swirl chamber discharges the liquid by means of a final orifice through which the rotating fuel flows under the action of both axial and radial forces. The shape of the liquid at the exit of the orifice depends on the injection pressure. At

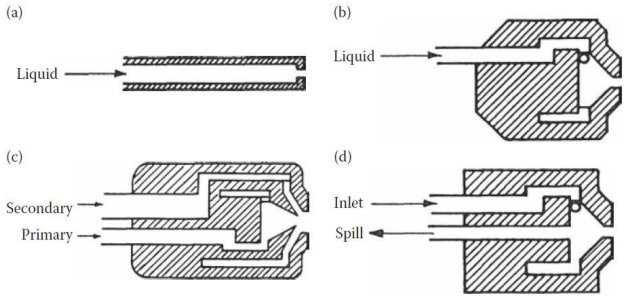

Figure 1.8: Schematic representation of pressure swirl atomizers (taken from [32]): (a) plain orifice; (b) simplex; (c) dual orifice; (d) spill return.

low injection pressures the liquid leaves the orifice in a form similar to a plain jet. As the pressure is increased a hollow conical sheet appears. Instability phenomena due to interactions between conical film and gas phase lead to the formation of ligaments which further disintegrate into droplets.

This basic configuration has been further improved in order to ensure a high quality of atomization in a wide range of flow rates. Examples of improved configurations are the *dual-orifice* atomizer (basically a combination of two simplex injectors) and the *spill-return* injector (a high injection pressure can be used in all conditions and the exceeding fuel is returned to the fuel tank through the spilling port).

1.2.2 Airblast atomizers

Differently from pressure injectors, airblast atomizers employ the kinetic energy of a flowing air-stream to disintegrate the fuel into drops. The simplest form of airblast atomizers is maybe the so called *plain-jet airblast* where a plain jet is subjected to a co-flowing high velocity air stream which makes the jet unstable leading to its fragmentation into small drops. However, in aero-engine applications, most of the airblast injectors are based on the so called *prefilming airblast* configuration. In this kind of injectors the fuel is first spread out into a thin

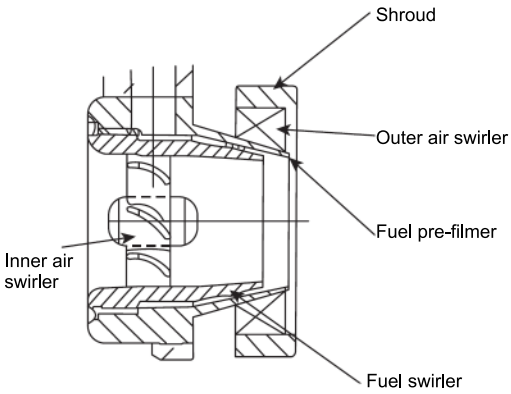

Figure 1.9: Example of prefilming airblast atomizer (taken from [28]).

continuous sheet which evolves along a prefilming surface under the action of a co-flowing air stream. As the liquid film reaches the atomizing edge it is subjected on both sides to high velocity air-streams which disintegrate the film into small droplets generally leading to a very fine atomization.

Fig. 1.9 shows an example of prefilming airblast injector for aeroengine applications where the liquid film directly interacts with the swirled flows used for flame stabilization. In this design, the atomizing air flows through two concentric air passages that generate two separate swirling air-flows at the nozzle exit. The fuel is injected through tangential ports onto a prefilming surface where it spreads onto a thin film. Then the film reaches the atomizing edge where the action of the two swirled air flows causes the disintegration of the liquid sheet into droplets.

An important design choice is whether the two swirling air-streams should be co-rotating or counter-rotating. In order to perform a proper choice, it should be considered that the swirled structures are not only useful to obtain a fine atomization but, as previously discussed, they also influence the stability of the combustion process through the generation of a strong vortex core which recirculates hot combustion products in the flame region. In co-rotating configura-

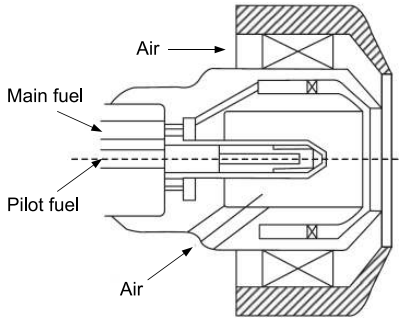

Figure 1.10: Example of a piloted airblast atomizer (taken from [34]).

tions, the two air flows support each other in the creation of a strong recirculation zone whereas the advantage of counter-rotation is that it promotes a stronger shearing action between liquid sheet and air flows which could lead to an improvement of atomization quality. However, since the two swirl components are in opposite directions, the resulting swirl strength may reduce flow recirculation in the primary combustion zone. This drawback can be alleviated by making one of the two swirled flows, usually the outer, much stronger than the other [28].

Airblast atomizers have many advantages compared to pressure atomizers, especially in their application to combustion systems operating at high pressures. The main advantages include finer atomization and little changes in performance over a wide range of operating conditions [33]. Therefore, many injection configurations used in modern lean burn combustors are based on airblast atomizers [11]. The main limits of airblast systems appear during engine startup where lean blowout may occur together with a poor atomization quality due to the low velocity air streams. In order to overcome these drawbacks, in some injection systems the prefilming airblast atomizer is used in combination with a pressure atomizer in a configuration which is often referred to as *piloted airblast* system [32] (see Fig. 1.10). At low fuel flows, most of the fuel is supplied through the pilot injector leading to a fine atomization and a more efficient combustion. On the other hand, at high loads the fuel is mainly injected

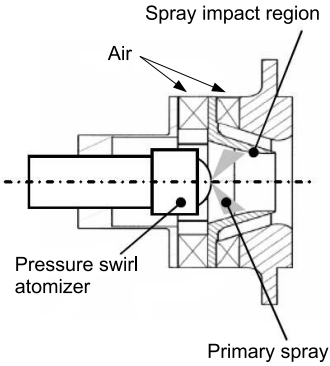

Figure 1.11: Impinging airblast configuration (taken from [35]).

through the airblast atomizer exploiting the advantages of this type of injectors.

Furthermore, in some airblast designs the liquid film could also be generated by the impingement of droplet injected through a pressure atomizer (see Fig. 1.11). These configurations (sometimes called swirl-cups) usually consist in a double-swirl system with a pressure atomizer located at the center of the inner swirler [11, 35, 36, 37, 38]. Droplets injected through the pressure atomizer first breakup and partially evaporate, then they impact onto the lip that separates the two swirled flows creating a liquid film which is eventually atomized by the high velocity air-stream [39].

1.2.3 Advanced configurations for lean burn applications

As discussed in Section 1.1.2, the performance of a lean burn combustor is strongly connected to the ability of the injection system to generate a highly homogeneous mixture and to ensure a proper stabilization of the combustion process. Therefore, injection systems proposed for lean burn applications are usually based on advanced configurations designed as internally staged injectors with a pilot and a main stage and multiple swirling channels and efficient atomization

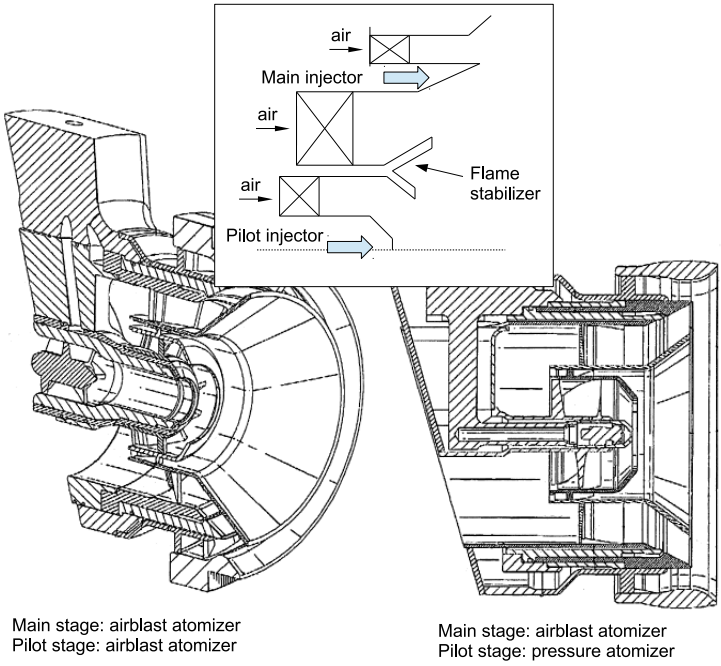

Figure 1.12: Rolls-Royce LDI injector design (adapted from [40]).

systems.

Fig. 1.12 shows an example of advanced injection system based on an internally piloted configuration. The main fuel injection consists in a prefilming airblast system where the fuel is distributed over a large surface area resulting in a thin fuel layer exposed to high velocity flows generated by two axial swirlers. Flow passages and injector geometry are optimized in order to achieve a rapid evaporation and mixing in short distances, before the fuel reaches the flame anchoring location [11]. The fuel rich pilot stage, located at the center of the airblast system and surrounded by a third swirler, is required for engine startup, low power operation, and stabilization of the main stage, preserving the turn-down ratios of rich burn combustors for operability, especially for transient manoeuvres during adverse weather

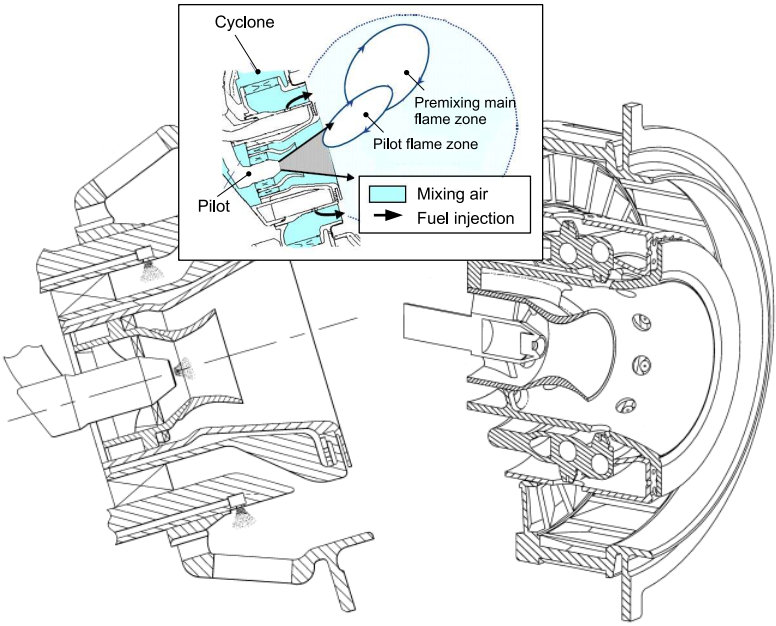

Figure 1.13: TAPS internally staged fuel injector concept (adapted from [42, 43, 44, 45]).

conditions such as hail and rain [41]. As shown Fig. 1.12, the pilot atomizer could consist whether in a pressure atomizer or in an airblast injector (in this case an additional air passage is located in correspondence of the injector axis).

Although the focus of this dissertation will be on systems based on airblast configurations, it should be noted that configurations different from prefilming airblast injectors can also be found in gas turbine applications and in particular in lean burn combustors. An example is the injection system exploited in the GE-TAPS (Twin Annular Premixing Swirler) combustor [42]. Fig. 1.13 shows a schematic representation of this configuration which is based on an internally staged pilot injection with a lean direct multi-point injection for the main stage operation. Air passages are based on a multi-swirler arrange-

ment specifically designed to achieve proper spray quality and flow field characteristics in the downstream region. In the configuration presented in Fig. 1.13, the pilot stage consists in a simplex pressure atomizer surrounded by two co-rotating swirlers whereas the main mixer consists of a radial inflow swirler (cyclone) and a cavity where the main fuel is injected by discrete transverse jets [42]. Different configurations for the main stage injection have been proposed with the main aim of obtaining a faster and more efficient mixing (some examples are shown in Fig. 1.13).

It is important to note that the examples reported here do not cover all the possible configurations that can be found in technical literature. Lean burn technology is a very active research field and new injection strategies and geometrical configurations are being developed [46, 47] and maybe in the next future increasingly efficient solution will be exploited in modern aero-engines.

1.2.4 PERM injection system

The development of numerical tools performed in this research has taken as reference an advanced lean burn injection system developed by Avio Aero based on the PERM (Partially Evaporating and Rapid Mixing) concept. Fig. 1.14 a schematic representation of the functioning concept of the PERM injector whereas in Fig. 1.15 an example of aero-engine combustor exploiting the PERM technology is reported.

The PERM injection system is basically a double swirler airblast atomizer developed in order to achieve partial evaporation inside the inner duct and rapid mixing within the combustor, optimising the location and the stability of the flame. A film of fuel is generated over the inner surface of the lip that separates the two swirled flows. As the film reaches the edge of the lip, through the action of the primary flow, primary atomization occurs: fine droplets and rapid mixing are promoted by the two co-rotating swirled flows generated by the double swirler configuration. Furthermore, in order to ensure a stable operation of the lean burn system, especially at low power conditions, the airblast injector is coupled with a hollow cone pressure atomizer (pilot injector), located at the centre of the primary swirler, which generates a pilot flame to stabilize the combustion process in

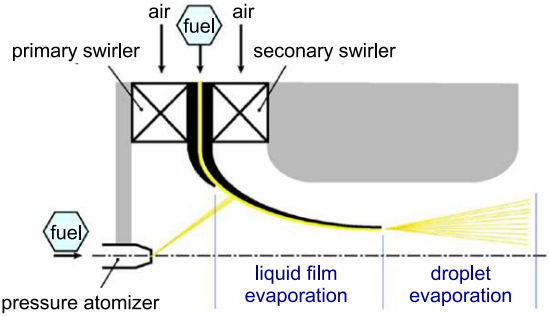

Figure 1.14: PERM functioning concept (taken from the website http://www.newac.eu).

a configuration similar to the piloted airblast described above. The pilot injector is usually active within the entire operating range with a variable fuel split between pilot and main stage.

It is important to note that in some operating conditions, in particular at idle or more in general at low pressure with a high pilot/main fuel split, droplets injected through the pressure atomizer could reach the lip promoting the formation of the liquid film. In these cases the aspects related to the modelling of wall/film-droplet impact are fundamental to determine the amount of fuel added to the liquid film by droplet impingement or droplets generated as a consequence of the impact with the film surface.

1.3 Concluding remarks

The injection system is the most important component of a lean burn aero-engine combustor since it directly controls the fuel distribution inside the combustion chamber and the quality of air-fuel mixture determining the characteristics of the combustion process and engine emissions. Therefore, in order to develop a combustion system based on the lean burn technology it is fundamental to consider all the aspects related to liquid fuel preparation, from injection and atomization to evaporation and mixing with the gas-phase.

In the remainder of this dissertation all the aspects related to liq-

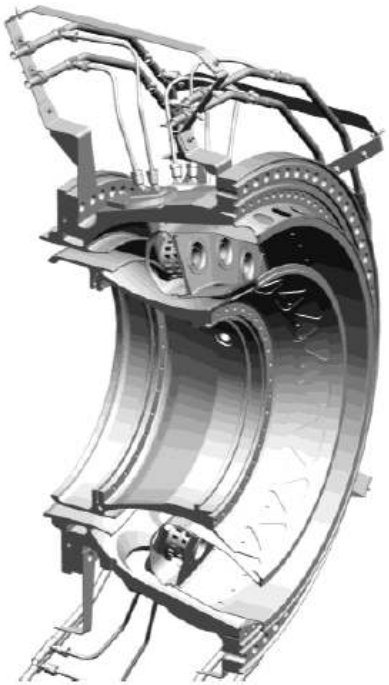

Figure 1.15: Lean burn aero-engine annular combustor exploiting the PERM injection system (Avio Aero).

uid fuel atomization and spray evolution will be analysed with great detail and a numerical approach able to include in typical industrial computations the most important phenomena regulating liquid fuel preparation in advanced airblast injectors will be presented. The configuration taken as reference for the development of the numerical tools proposed in this research is the PERM injection system presented in this chapter. This configuration is based on a prefilming airblast injector with a pilot atomizer placed at the center of the airblast system. In this kind of injector liquid fuel preparation is regulated by the complex interactions between liquid film, droplets and gas-phase and in order to properly predict the air-fuel mixing all

the aspects related to film evolution, primary breakup, interactions between liquid film and droplets and spray evolution have to be properly modelled.

Chapter 2

Atomization and sprays

Combustion efficiency and pollutant emissions are strongly influenced by the quality of liquid fuel preparation the characteristics of liquid droplets generated through the atomization process and in order to develop a combustion system based on the lean burn technology it is important to carefully analyse all the aspects related to liquid atomization and spray evolution. In this chapter the basic concepts of atomization are introduced together with a brief description of droplet impingement phenomena which could be important in the injection configuration considered in this work. Furthermore, useful quantities for the description of droplet population generated after breakup are presented.

2.1 Some definitions

Before presenting the most important aspects of liquid fuel preparation, some basic quantities and definitions should be introduced. First of all, the word *spray* will be used to generically indicate a population of droplets whereas a group of droplets with the same characteristics, in terms of diameter, velocity and thermodynamic properties, will be referred to as *parcel*. As explained in Section 3.1, the concept of parcels is very useful in the development of numerical codes as it allows the reduction of computational costs related to the description of spray evolution.

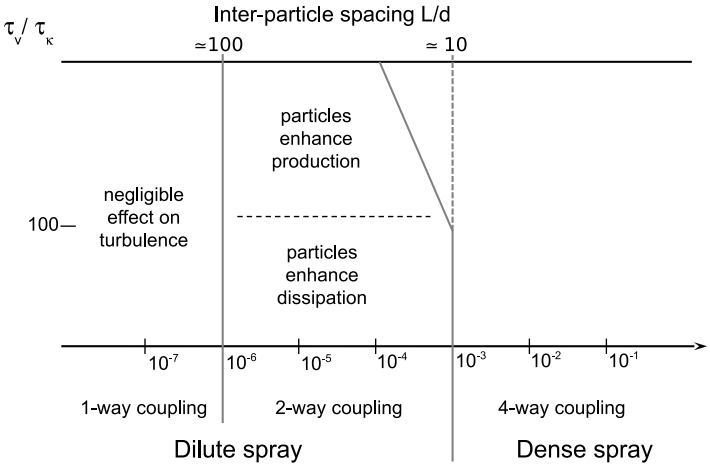

Figure 2.1: Interaction regimes between droplets and gas phase.

2.1.1 Interaction regimes

A very interesting quantity for the description of a spray is the volume fraction α_P, that is the ratio between the volume occupied by the droplets and the total volume of the mixture.

$$\alpha_P = \frac{\sum_{i=1}^{N} V_{d,i}}{V} \tag{2.1}$$

where N is the total number of droplets. This quantity is very useful to give a first classification of multi-phase flows involving sprays. In particular, it is possible to distinguish different regimes for the interaction between droplets and gas phase (see Fig. 2.1) which have a direct consequence in the numerical modelling.

As also described in [48, 49, 50], for volume fractions less than 10^{-6}, particle motion is influenced by the continuous phase but there is practically no feedback from the dispersed phase to the carrier phase. This regime is known as *one-way coupling* and in this case numerical simulations could neglect the effects of droplet motion into

the gas phase.

For particle volume fractions in the range from 10^{-6} to approximately 10^{-3}, the influence of droplet on the gas phase is not negligible and in order to properly describe the multi-phase flow a *two-way coupling* approach should be used. For volume fractions less than 10^{-3}, the inter-distance between droplets can be considered very high and the spray is termed *dilute*. Because of the high spacing between particles, in the dilute regime droplets are supposed to not interact with each other and thus no collision model is needed and models developed for single droplets can be safely used to describe the dynamics of each droplet inside the spray.

Finally, for volume fractions greater than 10^{-3} the spray is considered *dense* and a *four-way coupling* which includes particle-particle interactions is required. This regime is typical of the regions very close to the injector exit where primary breakup occurs and proper numerical treatments should be used.

2.1.2 Useful non-dimensional numbers

During the spray formation and evolution, and more in general in multi-phase flows, the liquid is subjected to many interactions with the gas-phase and boundary walls. In many cases it could be very useful to perform an order of magnitude analysis in order to determine what are the prevailing interactions. Such analysis allows us to introduce some non-dimensional groups. Since a multi-phase flow is considered, in addition to typical gas-phase properties, quantities related to the liquid phase should also be considered since they have a great importance in many physical processes such as evaporation and breakup.

An important dimensionless group is the so called *Weber number* which represents the ratio between momentum force and surface tension force [32]:

$$We = \frac{\rho_g U_R^2 L}{\sigma} \tag{2.2}$$

where L is a length scale parameter, typically the droplet diameter, and U_R is the relative velocity between the liquid and the gas-phase.

This number is widely used in the breakup theory since it gives a measure of the relative importance between aerodynamic interactions and surface tension.

Another useful dimensionless number is the *Ohnesorge number* which relates the internal viscous force to inertia and surface tension forces:

$$Oh = \frac{\mu_L}{\sqrt{\rho_L \sigma L}} \tag{2.3}$$

where L is a characteristic length scale. This dimensionless group is generally used to describe the effects of liquid viscosity in the atomization process.

Finally, in the study of droplet dynamics it could be useful to introduce the *particle Reynolds number* defined as:

$$Re_P = \frac{\rho_g d\|u - v\|}{\mu_g} = \frac{\rho_g d U_R}{\mu_g} \tag{2.4}$$

where d is the particle diameter and U_R is the relative velocity between the droplet and the carrier phase.

2.1.3 Relaxation times

The relaxation time is a characteristic time in the transient of a particle from an initial condition to a final state. Let's consider, for example, a droplet subjected to the action of the drag force exerted by the surrounding air flow. The particle dynamics is described by the Newton's second law:

$$m\frac{dv}{dt} = C_D \frac{\pi d^2}{8} \rho_g (u - v)\|u - v\| \tag{2.5}$$

where C_D is the drag coefficient. In the case of low Reynolds numbers ($Re_P < 1$), the drag coefficient is equal to $C_D = 24/Re_P$ and the previous equation can be rearranged in the following linear form:

$$\frac{dv}{dt} = C_D \frac{3}{4} \frac{\mu_g Re_P}{\rho_P d^2}(u - v) = \frac{1}{\tau_v}(u - v) \tag{2.6}$$

which for an initial droplet velocity equal to zero has the general solution:

$$v = u(1 - e^{-t/\tau_v}) \tag{2.7}$$

A new quantity, the so called *dynamical relaxation time*, τ_v, has been introduced. It represents the time required for a particle to reach the 63% of the gas phase velocity. This results is valid only at low Reynolds numbers. For higher Reynolds numbers, the equation of droplet dynamics cannot be written as in Eq. 2.6. However the same expression for τ_v is used by replacing the drag coefficient with a proper expression for high Reynolds numbers (see Section 3.4.1). The general expression for the dynamical relaxation time is:

$$\tau_v = \frac{4}{3}\frac{\rho_P d^2}{\mu_g Re_P C_D} \tag{2.8}$$

which in the case of $Re_P < 1$ becomes:

$$\tau_v = \frac{\rho_P d^2}{18\mu_g} \qquad (Re_P < 1) \tag{2.9}$$

In a similar way, relaxation times can also be introduced for other physical phenomena related to particle dynamics (for example evaporation and thermal heating) [50, 51].

The dynamic relaxation time allows us to define a new non-dimensional quantity, the *Stokes number* defined as:

$$St_v = \frac{\tau_v}{\tau_g} \tag{2.10}$$

where τ_g is a characteristic time of the gaseous phase. For turbulent flows the characteristic time will be the temporal integral scale of turbulence whereas for a periodic unsteady flow (coherent structures) this time will be represented by the period of vortices [50].

2.2 Atomization process

As discussed Section 1.2, typical injection systems used in gas turbine applications consist in pressure and airblast atomizers usually combined in more complex configurations in order to achieve a high quality air-fuel mixture and the full operability of the aero-engine combustor. In such systems the fuel is usually injected in the form of a plain jet or a thin sheet which disintegrate into small droplets in a process that is often referred to as *primary breakup*. This process is confined near the injection system and it has to be distinguished from the so called *secondary breakup* which describes the further breakup of droplets into smaller ones. As also described in [28], both these processes determine the detailed characteristics of the fuel spray in terms of droplet velocities and drop-size distributions. In the following, primary and secondary atomization phenomena will be described in more detail with the main aim of giving an introduction to the basic concepts of liquid fuel preparation which will be useful in the derivation of the numerical tools introduced in this research.

2.2.1 Primary atomization

Primary atomization is a very complex phenomenon affected by many parameters and different breakup mechanisms can be distinguished depending on the geometrical configuration and operating conditions. In the following, primary breakup will be described through a literature review of the most important mechanisms characterizing injection configurations used in aero-engine applications. The main objective is to give an overview of the complex physical phenomena regulating the breakup process identifying the most important characteristics of liquid disintegration. A detailed description of all possible cases is beyond the scope of this chapter thus in the following selected configurations will be considered. First of all, classical atomization mechanisms of the liquid jet are described, then liquid sheets are considered. Some considerations about primary breakup will be given again in Chapter 5 where a primary breakup model for a particular class of injectors will be introduced. The reader interested in a more comprehensive analysis is addressed to specific literature [32, 52] and to the references mentioned in the following.

2.2.1.1 Liquid jets

Classical theories on jet atomization are based on the unstable growth of disturbances which lead to the jet fragmentation. It is important to point out that disturbances are intrinsically present in jet dynamics since they naturally arise as the liquid flows through the injection system or because of the interaction with the gas-phase.

The first theoretical study on jet breakup was performed by Rayleigh [53] who considered a laminar jet, with an initial diameter equal to d_j, issuing from a circular orifice and subjected to surface disturbances. He found that symmetric disturbances characterized by an optimal wavelength $\lambda_{opt} = 4.15 d_j$ are likely to increase over time finally causing the breakup of the jet into ligaments which eventually become spherical droplets with a diameter, d, equal to:

$$\lambda_{opt} \frac{\pi}{4} d_j^2 = \frac{\pi}{6} d^3 \rightarrow d = 1.89 d_j \tag{2.11}$$

Later, as discussed in [28], Weber extended the Rayleigh's theory including the effect of liquid viscosity through the Ohnesorge number introduced in Section 2.1.2. According to Weber's theory, the expression for the optimal unstable wavelength is given by:

$$\lambda_{opt} = \sqrt{2}\pi d_j (1 + 3Oh)^{0.5} \tag{2.12}$$

where the characteristic length scale in the Ohnesorge number is the diameter of the cylindrical jet:

$$Oh = \frac{\mu_L}{\sqrt{\rho_L \sigma d_j}} \tag{2.13}$$

It follows that:

$$\lambda_{opt} \frac{\pi}{4} d_j^2 = \frac{\pi}{6} d^3 \rightarrow d = \left(\frac{3\pi}{\sqrt{2}} \right)^{1/3} d_j (1 + 3Oh)^{1/6} \tag{2.14}$$

In addition to liquid viscosity, another important quantity which strongly affects the atomization process is the initial velocity of the

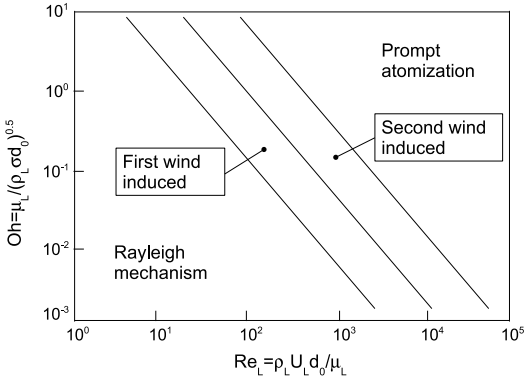

Figure 2.2: Classification of jet breakup regimes (reproduced from [32], d_o is the orifice diameter).

jet issuing from the orifice. The phenomena described by Rayleigh and Weber's theories are representative of jet breakup only at low liquid velocities. As the relative velocity between the liquid and the air is increased, aerodynamic interactions between the two fluids become more intense generally leading to smaller droplets. According to recent experimental findings, the following classification of breakup regimes is proposed [54] (see also Fig. 2.2 where the different jet breakup regimes are reported as a function of the liquid Ohnesorge and Reynolds numbers):

- *Rayleigh mechanism*: at low velocities the breakup mechanism studied by Rayleigh prevails. The jet disintegration is due to the growth of symmetric oscillations under the action of the surface tension which, for disturbance wavelengths greater than a minimum value, is able to amplify their amplitude. Droplets generated with this mechanism have a fairly uniform size with diameters that are roughly twice the initial jet diameter. The term *varicose* is usually used to describe this breakup regime due to the particular geometric conformation of the jet characterized by rotationally symmetric disturbances.

- *First wind-induced breakup*: the surface tension effect is magnified by the relative velocity between the jet and the gas-phase

which reduces the optimum wavelength for jet breakup resulting in smaller drop sizes.

- *Second wind-induced breakup*: with a further increase in jet velocity, droplets are produced by the unstable growth of small waves on the jet surface caused by interaction between the jet and the surrounding gas. The waves become unstable and detach from the jet surface in the form of ligaments that finally disintegrate into droplets that are much smaller than the initial jet diameter. Breakup occurs several diameters downstream of the nozzle exit.

- *Prompt atomization*: the jet disintegrate completely at nozzle exit and droplet diameters are much less than the jet diameter.

In the previous discussion the case of a liquid stream injected into an air flow has been considered. However, in particular injector configurations a plain jet subjected to a co-flowing air stream could also be encountered. In this case, also called air-assisted cylindrical jet, different breakup mechanisms can be observed as described in [52]. Considering a liquid jet issuing from a cylindrical orifice with a coaxial air-stream, the following regimes can be distinguished:

- *Rayleigh mechanism*: for very low relative velocities between the co-flowing air stream and the liquid jet ($We_j < 25$, with $We_j = \rho_g(U_g - U_j)^2 d_j/\sigma$) the jet breakup follows a mechanism similar to the one described by Rayleigh. Droplet diameters are of the order of jet diameter. Two different sub-regimes can be distinguished with axisymmetric deformation (as observed for liquid jets in a still medium but with shorter breakup lengths) and non-axisymmetric structures.

- *Membrane-type breakup*: this regime ($25 < We_j < 70$) is characterized by the development of thin liquid sheets, which form Kelvin-Helmholtz waves and break into droplets of much smaller diameter than in the previous regime. The morphology of the jet becomes similar to that of a thin liquid sheet.

- *Fiber-type breakup*: this case ($100 < We_j < 500$) is identified as the formation of thin liquid fibres that peel off the jet and disintegrate through a mechanism similar to the non-axisymmetric

mode observed at low relative velocities. Farther downstream, the main liquid core becomes wavy and breaks into ligaments from which new fibres are peeled off. The diameters of the drops are very small and generally increase with the downstream distance.

- *Digitation*: in some experiments [55] another mechanism characterized by the development of digitations (ligaments) on the crests of an axisymmetric perturbation has also been observed. These ligaments subsequently disintegrate following a non - axisymmetric Rayleigh-type mechanism (the digitations-type breakup regime is observed at the same We_j of the membrane-type breakup regime [52]).

In Fig. 2.3 a representation of the different breakup regimes of air-assisted cylindrical jets is reported.

2.2.1.2 Liquid sheets

Several injection systems, ranging from pressure-swirl atomizers to airblast atomizers (for a description of these types of injectors see Section 1.2), discharge the liquid in the form of a liquid sheet. Depending on the injector configuration, the liquid sheet can have the shape of a flat, annular or conical sheet. Furthermore, in some cases a high velocity liquid sheet is injected in a quiescent medium whereas in other situations the opposite happens with a high speed air flow acting upon the liquid sheet.

As for the liquid jets, one of the most important parameters that regulates the atomization process is the relative velocity between the liquid and the gas-phase. Different atomization mechanisms can be found depending on the particular configuration. As an example, the case of a flat sheet emerging from a rectangular slit and surrounded on both sides by a gas flow is considered [56, 52]. In the absence of air stream ($U_g = 0$), the liquid sheet converges down to a point where the two rims developing on the sheet edges coalesce. Increasing liquid velocity, effects related to turbulence appear leading to perforations of the liquid sheet. However these phenomena are not accompanied by any drop formation. When a high-speed gas stream is added, the significant shear generated at the interfaces with the low-velocity

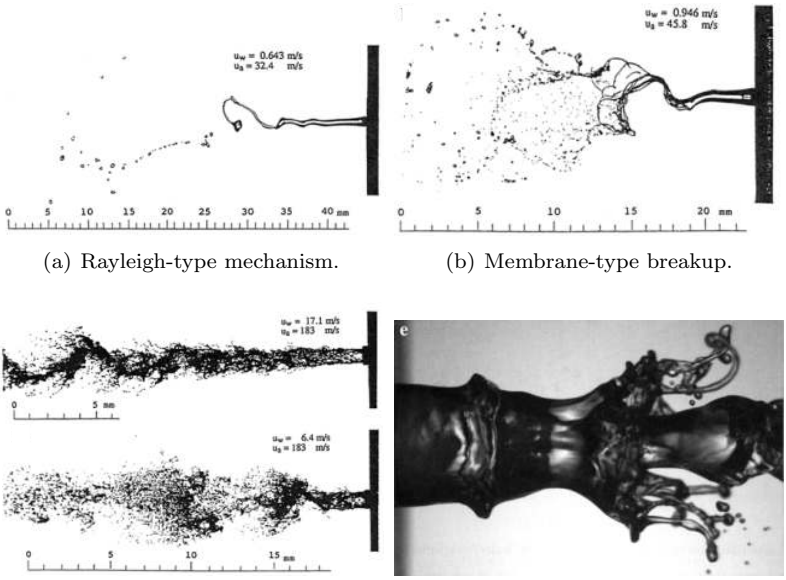

(a) Rayleigh-type mechanism.

(b) Membrane-type breakup.

(c) Fiber-type breakup.

(d) Digitation [55].

Figure 2.3: Breakup regimes for air-assisted cylindrical jets (taken from [52]).

liquid sheet, in particular in the region close to the nozzle, causes the growth of instabilities which lead to the formation of longitudinal and transverse waves on the liquid sheet. The amplitude of these waves quickly grows resulting in the sheet disintegration. Different regimes can be observed as summarized in the following:

- *Cellular breakup regime*: at low U_g/U_L, the sheet oscillates in a mixture of sinusoidal and dilational waves with low amplitude growth. The liquid sheet penetration is high and the spray angle is small. The growth of both spanwise and streamwise ligaments gives rise to liquid cellular structures which lead to the disintegration of the liquid sheet.

- *Stretched streamwise ligament regime*: when the relative veloc-

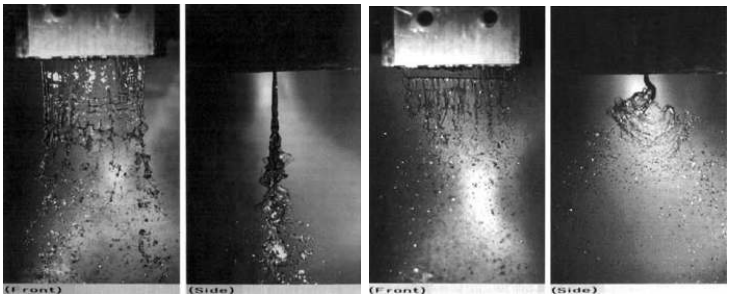

(a) Cellular breakup regime. (b) Stretched streamwise ligament regime.

Figure 2.4: Breakup of air-assisted flat sheets (taken from [52]).

ity increases ligaments formed in the flow direction predominate over the formation of spanwise ligaments. Above this, the liquid flow is subject to a strong lateral sinusoidal oscillation which is the cause of a high spray angle. The sheet breakup length is short and droplets are mainly generated trough the disintegration of ligaments.

- *Prompt atomization*: for further increases of U_g/U_L ratio, the streamwise ligaments recede to the nozzle tip. No intact liquid sheet length is visible and breakup in longitudinal ligaments occurs at the nozzle exit.

Fig. 2.4 shows experimental visualizations of the first two breakup regimes described above.

As for the liquid jets, theoretical stability analyses have also been performed for liquid sheets (a liquid sheet moving in a quiescent medium is often considered). A good review of them is presented in reference [57] where also the cases of conical and annular sheets are considered. According to these works, the liquid sheet breakup mechanism is usually described as a combination of the following steps [58, 59]:

- The aerodynamic interaction between liquid and air gives rise to the formation of waves on the liquid surface.

- Unstable wavelength grows over time leading to the formation of ligaments or liquid clusters.

- Ligaments fragment into droplets with a mechanism similar to the capillary breakup described by the Rayleigh theory.

The stability analysis is able to give the dimension of the most unstable wavelength which is used to derive expressions for ligament diameter. Finally, the application of Rayleigh theory allows us to compute the diameter of droplets generated after atomization starting from ligament diameter. The resulting expressions are usually quite simple and suitable for implementation in numerical models [59, 60]. However, it is important to point out that the aforementioned description of the liquid sheet primary breakup process is very simple and in some cases could not be representative of the actual breakup process.

2.2.1.3 Some remarks

As can be deduced from the previous description, the atomization process is a very complex phenomenon where small scale interactions could play an important role in determining droplet characteristics after breakup. Furthermore, disintegration mechanisms are also dependent on the particular injection configuration making the development of an unified theory on atomization very difficult. Therefore, numerical models developed to describe the atomization process are usually strongly case-dependent. This particular characteristic of the primary breakup process has also influenced this research work where specific models for a prefilming airblast injector have been developed.

The development of a theoretical (physical-based) model for primary atomization requires a deep knowledge of the breakup mechanism. Unfortunately, the physics of primary breakup is still not completely understood and therefore most of the models are based on a phenomenological description or rely on simplified theoretical instability analyses.

The main parameter affecting atomization in the configurations presented in this section is the relative velocity between the liquid and the air flow and the quality of atomization usually increases with

an increase of the relative velocity. For higher values of the relative velocity all the experiments reveal a similar trend irrespective of the particular liquid configuration. When the relative velocity is very high, the liquid jet or sheet is disintegrated by the vigorous interaction with the surrounding air immediately downstream of the injection location. This atomization regime is often referred to as *prompt atomization* in order to underline that the atomization process takes place very close to the injection system. As reported in [28], an essential feature of this mode of atomization is that the rapid and violent disruption of the fuel ensures that the ensuing drop sizes are largely independent of the initial fuel dimension (jet diameter or sheet thickness). Furthermore, the atomization process also appears to be independent of viscosity, which cannot affect a process that occurs very rapidly. Prompt atomization is often observed at operating conditions encountered in gas-turbine applications.

2.2.1.4 Factors influencing atomization

As previously discussed, the most important quantity influencing atomization in configurations typical of pressure and airblast atomizers is the relative velocity between the liquid flow and the gas-phase. A higher relative velocity usually improve the quality of atomization. However, several other factors may influence the atomization process such as the liquid viscosity and the geometrical configuration of the injection system. The most important factors can be summarized as follows [32]:

- injector geometry;
- liquid properties;
- gas medium properties.

The geometry of the injection system determines the interaction between liquid fuel and gas phase and it is the main responsible for the spray characteristics and distribution pattern inside the combustion chamber. Great attention has to be devoted to the design of the geometrical features in order to ensure a reliable operation of the injection system. The shape and the basic characteristics of the atomizer are usually determined by the physical mechanism chosen

to generate the disruptive force that leads to droplet formation (see Section 1.2). Low cost, light weight, easy of maintenance and removal for servicing, ability to provide a good atomization over a wide range of fuel flow rates are typical requirements to be considered in the improvement of basic injection configurations and the development of new ones.

The most important liquid properties influencing atomization are the surface tension and the dynamic viscosity. The first one can be viewed as a force that tends to pull the liquid in the configuration of minimum surface energy (a sphere in the absence of external forces) preventing the formation of new liquid surface. Thus, in equilibrium configurations, it can be considered a factor that acts against the disruption (this is the case for example of secondary atomization) whereas if the liquid is not in an equilibrium configuration, the surface tension could become an important factor in the liquid deformation and possible disintegration (this is for example the case of capillary instability of free liquid jets [61]). On the other hand, liquid viscosity has an adverse effect on atomization because it opposes any change in liquid geometry. Furthermore the viscosity also influences the flow inside the injector. An increase of liquid viscosity generally leads to a deterioration of the quality of atomization with an increase of droplet diameter and a delay in droplet formation. Finally, liquid density has only a marginal effect on the breakup phenomenon.

Properties of the medium into which the liquid is injected also influence the atomization process. Pressure and density appear the most important quantities to be considered in the atomization, however their effect is strongly connected to the type of injector. For example, in airblast atomizers an increase in density leads to an improvement of the atomization quality whereas in pressure swirl atomizers two opposing effects appear. As in airblast injectors, an increase of density causes stronger aerodynamic interactions determining smaller droplet diameters and lower breakup lengths, however the spray angle decreases.

2.2.2 Secondary atomization

A droplet moving in a gaseous phase is subjected to aerodynamic forces which could lead to droplet deformation and fragmentation.

The breakup of a droplet into smaller entities is usually referred to as *secondary atomization*. Many studies can be found in literature about secondary atomization. A good review of them is presented in reference [62]. In the following some basic concepts will be presented.

2.2.2.1 Critical Weber number

Simple considerations about droplet stability can be drawn by considering a single droplet subjected to a moving air flow. The critical condition for drop breakup is reached when the aerodynamic force (that is the drag force) is equal to the surface tension force [28]:

$$C_D \frac{\pi}{8} d^2 \rho_g U_R^2 = \pi d \sigma \tag{2.15}$$

Rearranging this equation, a critical Weber number can be found allowing us to give a measure of the maximum diameter of stable droplets that can be found in a spray:

$$\left(\frac{\rho_g U_R^2 d}{\sigma}\right)_c = We_c = \frac{8}{C_D} \rightarrow d_{max} = \frac{We_c \sigma}{\rho_g U_R^2} \tag{2.16}$$

For low-viscosity fuels, experimental data on C_D suggest a value for We_c of around 12. In order to account for the influence of liquid viscosity, the expression for critical Weber number can be modified through the introduction of the Ohnesorge number (see Section 2.1.2). According to Brodkey [63], the following expression is proposed:

$$We_{c,lv} = We_c + 14\left(\frac{\mu_L}{\sqrt{\rho_L \sigma d}}\right)^{1.6} = We_c + 14Oh^{1.6} \tag{2.17}$$

As shown by Eq. 2.17, an increase in liquid viscosity usually leads to a higher critical Weber number. However the effect of viscosity on the critical Weber number is relevant only at high liquid viscosities.

2.2.2.2 Secondary breakup regimes

According to experimental findings, different breakup regimes can be observed as shown in Fig. 2.5. Transition between the different

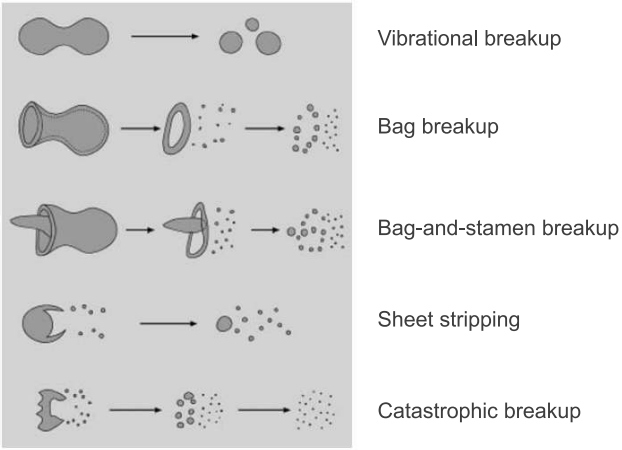

Figure 2.5: Secondary breakup regimes (adapted from [62]).

regimes depends on both droplet Weber number ($We = \rho_g U_R^2 d/\sigma$) and Ohnesorge number which, as previously stated, introduces the effects of liquid viscosity. However, for very low Ohnesorge numbers the dependence on liquid viscosity is negligible and transition between different regimes can be properly described on the basis of the sole Weber number. Typical values of the Weber number for the breakup regimes identified in Fig. 2.5, for $Oh < 0.1$, are [62]:

- vibrational breakup (We < 12);
- bag breakup ($12 <$ We < 50);
- bag-and-stamen breakup ($50 <$ We < 100);
- sheet stripping ($100 <$ We < 350);
- catastrophic breakup (We > 350).

Significant deformation starts at a Weber number of unity. This deformation, caused by the interaction between the droplet and the gas flow, is resisted by the surface tension and viscous forces. If the aerodynamic forces are large enough, above a certain value of the Weber

number, the droplet deformation leads to breakup. The first regime, the vibrational breakup, is not always observed and consists of oscillations at the natural frequency of the drop. The droplets generated after breakup have sizes comparable to those of the parent droplet. In the bag breakup regime, the droplet deformation leads to the formation of a thin hollow bag attached to a thicker toroidal rim. The bag disintegrates first generating a large number of small droplets, followed by the toroidal rim which results in a smaller number of large fragments. The bag-and-stamen breakup (also called multimode breakup) is similar to the bag breakup, but with the addition of a stamen oriented anti-parallel to the direction of the drop motion. As in the bag breakup, the bag is the first to disintegrate, followed by the rim and the stamen. In sheet stripping, a film is generated on the droplet surface from which small droplets are continuously torn off. This results in a cloud of small droplets and, in some cases, a core whose size is comparable to that of the parent droplet. Finally, for very large Weber numbers, the catastrophic regime appears. The drop surface is corrugated by waves of large amplitude and long wavelengths. Very small droplets are usually produced.

For $Oh > 0.1$, because of the effect of liquid viscosity, the critical Weber numbers that distinguish the different regimes may change. Typical expressions for the critical Weber number as a function of the Ohnesorge number have the same form of Eq. 2.17. Some indications about transition between the different regimes as a function of both We and Oh numbers can be found in references [62, 48].

2.2.2.3 Effect of turbulence

It should be noted that the gas-phase turbulence could have an important effect on droplet breakup. Turbulent fluctuations may have length scales of the same order of magnitude of droplet size inducing pressure gradients across the droplet which may cause droplet to disintegrate. Turbulence fluctuations can be one of the main cause of vibrational breakup. Moreover, air flow turbulence could determine a randomness of the breakup process where the Weber number based on the mean velocity could not be so representative since because of turbulence droplets experience different local velocities which determine different breakup behaviour. Also the inner turbulence of the

liquid, generated during the primary atomization process, could have an impact on droplet secondary breakup. In order to directly account for the effect of gas-phase turbulence Hinze [64] proposed an analysis based on a turbulent Weber number computed by considering the square of the RMS of turbulent velocity fluctuations ($\overline{u'}$) within the length scale which has the size of the droplet:

$$We_{c,turb} = \frac{\rho_g \overline{u'}^2 d}{\sigma} \tag{2.18}$$

According to this theory, the critical Weber number over which a droplet may disintegrate is much lower than the one observed for laminar flows as also observed by Prevish and Santavicca [65]. Hinze [64] proposed a value for $We_{c,turb}$ equal to 1.18 which is significantly lower than values found for laminar flows. It follows that in turbulent flows smaller stable diameters can be expected.

Despite these works, the influence of turbulence on droplet breakup is not completely understood and it is still an open field of research [62]. As shown in [48] the typical breakup regimes experimentally observed with a level of turbulence equal to 2%-3%, are similar to the ones described above and breakup models used in numerical solvers usually follow the previous classification.

2.3 Droplet impingement

In many devices and technical systems, interactions between droplets and walls or liquid films may occur. Interactions between droplets and solid walls are typical of internal engines but may also occur in gas turbines when droplets reach the liner walls. Furthermore, in the particular case of the PERM injection system described in Section 1.2.4 droplets injected through the pilot atomizer could reach the prefilming surface interacting with the liquid film or the solid surface if the film is not present. A proper characterization of droplet impingement is very important since it could have great influence on fuel distribution inside the combustion chamber affecting the flame behaviour. Therefore several works aimed at determining the characteristics of droplet impingement can be found in literature. A good review of them is presented in reference [66].

The impingement phenomena are influenced by many parameters ranging from droplet properties to surface characteristics. First of all, different phenomena may occur depending on whether the surface is wet or dry with the further effect of surface roughness. Furthermore, the surface temperature could also have an important effect determining different impact mechanisms. Droplet diameter, temperature and velocity, impact angle as well as fluid properties such as dynamic viscosity, density and surface tension are also important factors. As a common practice [67], the number of parameters can be reduced through the introduction of dimensionless parameters. In the case of droplet impingement, the most important non-dimensional numbers to be considered are the impact Weber number, We_I, defined through the droplet incident normal impact velocity v_I, and the droplet Laplace number, La, together with non-dimensional groups related to surface roughness and film thickness:

$$We_I = \frac{\rho_d v_I^2 d}{\sigma} \tag{2.19}$$

$$La = \frac{\rho_d \sigma d}{\mu_d^2} \tag{2.20}$$

On the basis of these dimensionless numbers, different interaction regimes can be distinguished. Fig. 2.6 shows a first classification proposed by the Bai and Gosman [68] of the different regimes for both dry and wetted surfaces at sub-boiling temperatures. The main parameter affecting the droplet impingement is the impact energy expressed through the impact Weber number (the effect of surface roughness, film thickness and Laplace number was not considered due to the lack of adequate experimental information). As described in references [66, 21], when the energy at impact is very low, the impinging droplet adheres to the wall in a nearly spherical form (*stick* regime). As the impact energy increases, *spread* regime occurs where the droplet spreads out to form a wall film for a dry wall or merges with the pre-existing liquid film for a wetted wall. It should be noted that in wetted surfaces the stick and spread regimes are separated

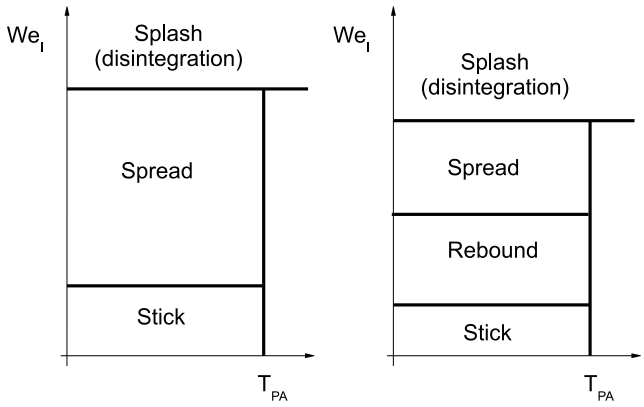

(a) Dry surface. (b) Wetted surface.

Figure 2.6: Droplet impact regimes at sub-boiling temperatures [68].

by the *rebound* regime: at low impact energy the air trapped between the droplet and the liquid film causes low energy losses and results in bouncing. According to the Bai and Gosman classification [68], rebound regime is not present for dry surfaces at sub-boiling temperatures (rebound is observed for dry surfaces only at high wall temperatures, see Fig. 2.7, where the contact between liquid droplet and hot surface is prevented by the formation of a vapour film) even if in other classifications [66, 69] rebound at low temperatures is also introduced for dry surfaces. At very high impact energy, the droplet disintegrates immediately after impact in a process which is often referred to as *splash*. In the splash regime a crown is formed which disintegrates into smaller droplets with a fraction of the mass that could be deposited on the wall.

Recent investigations about droplet dynamics during the impact with a dry surface [69] have observed that in the spread regime a liquid lamella forms which spreads and recoils until all the energy is dissipated. At moderate impact velocities, the rim of the lamella may destabilize at the beginning of the spreading phase and form regular structures called fingers, which grow ahead of the contact line and breakup during the last stages of spreading leading to the formation of

small droplets (this particular phenomenon is often called *fingering*). As the impact energy increases the so called *prompt splash* occurs where the droplet disintegrates within the first instants after impact. This is the disintegration mechanism which is usually recognized as the limit between spread and splash regimes described above and is distinguished from the *corona splash* where the formation of a liquid crown after impact is observed. In this discussion the effect of the surface roughness has not been considered. However, surface roughness could interact with the fluid structures which develop during the impact determining not negligible effects on the impact dynamics.

When the surface is covered by a liquid film, the impinging phenomena become even more complex. The impact behaviour may be affected by the ratio of film thickness to droplet diameter δ/d_0 as well as by the surface roughness amplitude through the parameter $R_{ND} = R_a/d_0$. According to Tropea and Marengo [70], the following cases can be distinguished:

- *very thin film*[1] ($L_R/d_0 < \delta/d_0 < 3R_{ND}^{0.16}$): droplet behaviour depends on surface conformation.
- *Thin film* ($3R_{ND}^{0.16} < \delta/d_0 < 1.5$): there is only a weakly dependence of droplet impact behaviour on surface topography.
- *Thick film* ($1.5 < \delta/d_0 < 4$): droplet impact is no longer dependent on surface topography but the dependence on the film thickness still remains.
- *Deep pool* ($\delta/d_0 > 4$): the impingement behaviour does not depend on surface topography nor on film thickness.

The Bai and Gosman classification presented in Fig. 2.6 could be representative of the thin film regime, usually encountered in engine applications. Therefore, this classification could be further improved considering the effect of film thickness and surface roughness. Furthermore, recent numerical and experimental investigations [71, 66] have revealed additional phenomena related to the dynamics of droplet-film interaction. Possible phenomena include deposition

[1] L_R is a length scale of roughness defined by Tropea and Marengo [70] to quantify the effect of surface roughness in addition to the mean roughness.

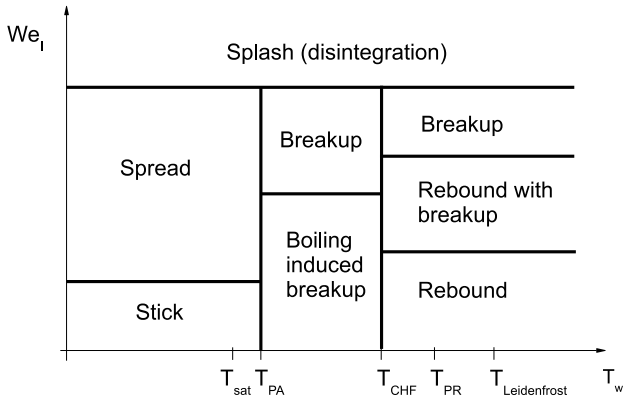

Figure 2.7: Impact regimes and transition conditions for a dry heated wall at fixed Laplace number and surface roughness (adapted from [21]).

and coalescence with the film, bounce or rise of a droplet ejection cascade (impact at small Weber numbers), formation of a crater on the liquid film at the droplet impact region (moderate Weber numbers) up to corona splash, splashing crown destruction by film fluctuations, uprising of central jet breakup and film jetting with subsequent breakup. A detailed description of the different mechanisms can be found in the review by Yarin [71].

As said above, also the surface temperature has a strong impact on droplet impingement behaviour. As an example, Fig. 2.7 shows droplet impact regimes on dry surfaces at different wall temperatures. The temperature values reported in the abscissa of Fig. 2.7 are the classical values used to identify different evaporation regimes of a droplet placed on a heated surface [66]. The pure adhesion temperature, T_{PA}, and pure rebound temperature, T_{PR}, are usually expressed as functions of the wall and particle material combination. As described in [21], in the *boiling-induced breakup* regime the droplet disintegrates due to rapid liquid boiling on the hot wall (the wall temperature is near the Nakayama temperature T_N). In the *rebound with breakup* regime the droplet rebounding on the hot surface causes the fragmentation into two or three droplets whereas in the

breakup regime the droplet first undergoes a large deformation which leads to the formation of a radial film on the hot surface and then the thermo-induced instability within the film causes the fragmentation of the liquid film.

It is important to point out that typical investigations on droplet impingement have been performed considering a single droplet impact which is very useful to understand the basic mechanisms. However, when a spray is considered, impact structures generated by neighbouring droplets could affect the droplet impingement dynamics which therefore could differ from the single droplet mechanism. Furthermore, in the case of a wetted surface, impinging droplets could influence the film dynamics as well as film dynamics could affect the impact behaviour and the characteristics of droplets generated after droplet-film interaction. Very little research is available in this field and further investigations are required in the future to give more insight into these important aspects.

2.4 Representation of droplet population

Because of the random nature of the atomization process, the population of droplets generated by the typical injectors used in gas turbine applications are characterized by a wide range drop sizes. The characteristics of the spray have a strong impact on the combustor behaviour since they directly influence the evaporation process and thus the fuel distribution inside the combustion chamber. In the following mathematical functions able to describe diameter distributions are introduced together with some measures of mean diameter and spray pattern.

2.4.1 Mean diameter

In order to compare the performance of different injectors, it is important to define some quantities able to describe the characteristics of droplet distributions. In many situations a representative mean diameter and a measure of the dispersion around it are sufficient.

Depending on the application, several definitions of the mean diameter can be found in literature. Considering a spray with a total

number of N droplets, a general definition of the mean diameter is given by the following expression:

$$D_{ab} = \left(\frac{\sum_{i=1}^{N} d_i^a}{\sum_{i=1}^{N} d_i^b} \right)^{\frac{1}{a-b}} \tag{2.21}$$

With this definition, D_{10} is the arithmetic average of the diameter of all spray droplets and D_{30} is the diameter of a droplet whose volume, if multiplied by the total number of droplets contained in the spray, is equal to the total liquid volume of the spray. Many other diameters can be defined in the same way. Among the various possible definitions, the D_{32}, usually called *Sauter mean diameter* (SMD), is generally considered the most appropriate in combustion applications, since it is the most relevant to the rates of evaporation and combustion [33]. SMD represents the diameter of a drop whose ratio between volume and surface area is equal to the volume-surface ratio of the entire spray.

$$D_{32} = \frac{\sum_{i=1}^{N} d_i^3}{\sum_{i=1}^{N} d_i^2} \tag{2.22}$$

Furthermore, D_c (where c is a real number between 0 and 1) is used to indicate the diameter such that the ratio between the volume of particles with diameter less than D_c and the total volume of the spray is equal to c. For example, $D_{0.632}$ is the drop diameter such that the 63.2% of the total liquid volume is contained in drops of smaller diameter. $D_{0.632}$ is equal to the parameter X of the Rosin-Rammler distribution (Eq. 2.23), introduced in Section 2.4.2. Finally D_{peak} is used to indicate the most probable diameter in a drop size frequency distribution curve.

Besides a mean diameter, it is also important to give a measure of the spreading of the spray. Several parameters can be identified, however in practical applications the difference between two different diameters (for example $D_{0.9}$ and $D_{0.1}$) or the dispersion parameter of a distribution function (such as q in the Rosin-Rammler formulation) are usually sufficient.

2.4.2 Mathematical distributions

In numerical simulations initial droplet diameters are often assigned as a boundary condition, thus it could be very useful to introduce mathematical formulations representing the distribution of droplet diameters to be directly exploited in numerical codes. In the absence of a comprehensive theory on the atomization process, the various functions that have been proposed are based on either probability or purely empirical considerations and are calibrated using experimental measurements. Typical formulations used in spray applications include normal, log-normal, chi-squared and Rosin-Rammler distributions. In general, the formulation that has to be chosen is the one that give the best fit with the experimental diameter distribution. In the following a brief description of the Rosin-Rammler distribution is given whereas more detail about the other formulations can be found in reference [32].

The Rosin-Rammler function [72] is an empirical distribution which may be expressed in the following form (cumulative distribution):

$$1 - Q = \exp\left[- \left(\frac{d}{X} \right)^q \right] \tag{2.23}$$

where Q is the fraction of the total volume contained in droplets of diameter less than d, X is the drop diameter such that 63.2% of the total liquid volume is contained in drops of smaller diameter and q is a measure of dispersion of drop sizes. The higher value of q, the more uniform is the spray, as also shown in Fig. 2.8.

The two parameters, X and q appearing in the definition of the Rosin-Rammler distribution, can be related to the most important definition of representative diameters through the following expressions:

$$\frac{D_{32}}{X} = \left[\Gamma\left(1 - \frac{1}{q} \right) \right]^{-1} \tag{2.24}$$

$$\frac{D_{peak}}{X} = \left(1 - \frac{1}{q} \right)^{\frac{1}{q}} \tag{2.25}$$

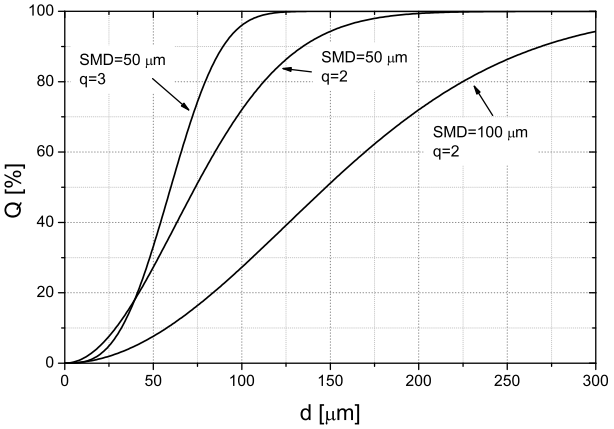

(a) Cumulative distributions.

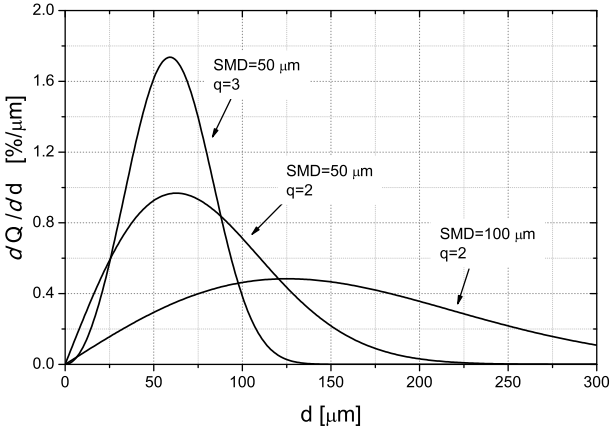

(b) Frequency distributions.

Figure 2.8: Examples of Rosin-Rammler distributions.

where $\Gamma(\bullet)$ is the gamma function. Experimental correlations for injectors [73] usually give the SMD thus, if the dispersion parameter is known (for most sprays q lies between 1.5 and 4.0), Eq. 2.24 can

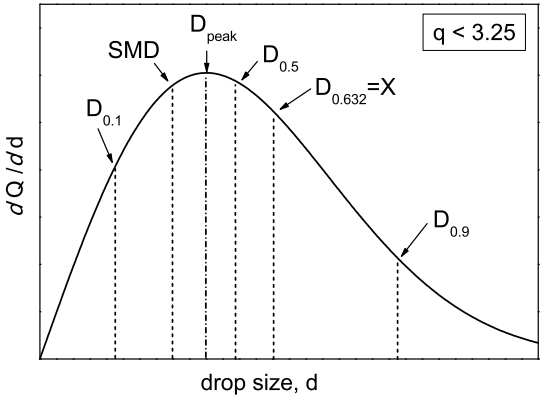

Figure 2.9: Location of various representative diameters along a Rosin-Rammler frequency distribution (reproduced from [32]).

be used to compute the parameter X. An example of location of the most representative diameters along the drop size frequency distribution curve is given in Fig. 2.9.

2.4.3 Spray global parameters

In addition to mean diameter and a measure of dispersion around it, it is important to define some quantities able to describe the spatial distribution of the spray inside the combustion chamber. Typical parameters used for pressure atomizers are the *spray penetration* and the *spray angle*.

Let's consider an injector with the axis placed along the z-direction, as shown in Fig. 2.10(a). The axial penetration S_A of the spray is defined as the distance from the injection location, computed along the injector axis, which contains a given amount of liquid mass (for example 95%). In a similar way, a normal penetration S_N can also be defined as the radius of the cylinder, whose axis lies along the injector axis, which contains a given amount of liquid mass. Finally, the radial penetration S_R could be defined as the radius of a sphere, with the center located at the injector exit, which encloses a given amount of the spray.

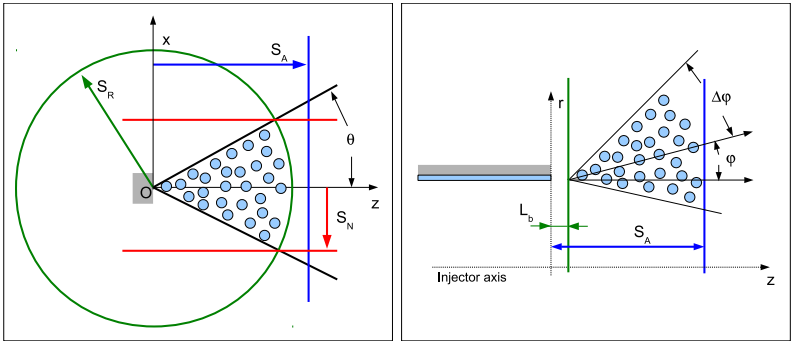

(a) Pressure atomizer. (b) Prefilming airblast atomizer.

Figure 2.10: Global parameters for pressure and airblast atomizers.

As shown in Fig. 2.10(a), the spray angle is evaluated as the angle of an imaginary cone, with the axis parallel to the injector axis and the vertex located at the injector exit, which contains a given amount of liquid mass (for example 99%). Some corrections can be applied in order to consider that the injector exit has usually the shape of a small circle and it does not discharge the liquid droplets in a single point.

Similar definitions can also be applied to prefilming airblast injection systems with some differences due to the particular configuration of the injector exit which delivers the fuel in the circular crown described by the annular atomizing edge. In this case, it is important to define an injection angle φ, that is the angle between the mean direction at which droplets are delivered and the injector axis (see Fig. 2.10(b)), and a spreading angle $\Delta\varphi$ around this value. Furthermore a spray axial penetration can also be introduced as the distance of a plane normal to the injector axis which encloses a given amount of the liquid mass (for example 95%). Finally the breakup length L_b is defined as the distance from the atomizing edge at which primary breakup is completed.

Chapter 3

Spray modelling

The design of lean burn combustors requires proper tools able to predict the liquid fuel evolution and distribution inside the combustion chamber. This research activity is mainly focused on the development of numerical tools to be used in typical industrial computations based on RANS (U-RANS) approach, thus in this chapter the basic concepts of spray modelling for standard RANS calculations are introduced. Furthermore the development and implementation of a steady-state Eulerian-Lagrangian solver for reacting sprays is discussed. Particular attention will be devoted to the presentation of models used to describe the interaction between gas-phase and droplets and to the validation of the developed solver.

3.1 Approaches for spray simulation

Multiphase flows involving sprays are very complex since many simultaneous physical processes have to be accounted for, e.g. primary and secondary breakup, interaction between droplets and turbulence, heat and mass transfer between particles and gas-phase, interaction of particles with each other. Fig. 3.1 shows a schematic representation of atomization process and spray formation with an indication of the regimes (defined in Section 2.1.1) that can be found in the different spray regions. Primary atomization occurs in the region close to the injection location. In the first stage of atomization the liquid is still a continuum distorted by the interaction with the gas flow. In this re-

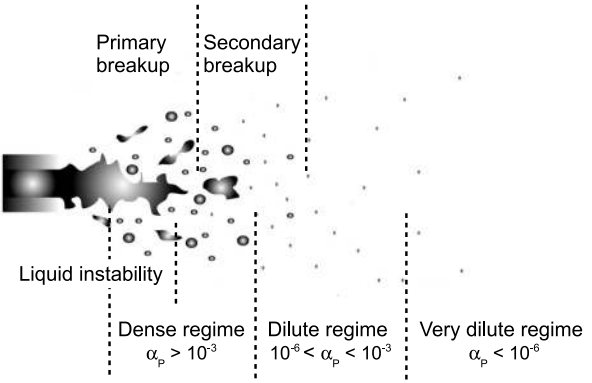

Figure 3.1: Sketch of atomization process and various flow regimes (adapted from [10]).

gion, very close to the injection location, the liquid flow dynamics can only be described by means of methods able to resolve the interface between the liquid and the gas-phase. Primary atomization leads to the formation of big droplets and ligaments which detach from the bulk liquid and move downstream. In the region near the injector, the volume fraction of these particles is very high and methods for dense sprays should be used (collisions between droplets cannot usually be neglected). Further downstream, droplets become much more dispersed and secondary atomization causes the disintegration of big fragments into smaller entities. At a sufficient distance from the atomizer, the spray can be considered dilute and approaches based on the two-way coupling are able to properly represent the spray evolution.

In standard industrial computations primary atomization and breakup phenomena occurring in the dense spray region and responsible for disintegration of ligaments are usually modelled through a primary breakup model which gives the characteristics of droplets to be injected downstream of the injector exit. Therefore, typical simulations are based on the *dilute spray* assumption. On the contrary, secondary breakup phenomena responsible for the further breakup of big droplets are usually included in the simulation through proper

secondary breakup models.

Several numerical methods can be used to simulate dispersed sprays [16, 49]. The most popular method is probably the Eulerian-Lagrangian approach where gas-phase is modeled as a continuum and solved following the Eulerian approach while particles are treated as discrete entities and tracked over the computational domain using a Lagrangian formulation. Interaction between gas-phase and particles is taken into account by means of simple models directly derived from basic physical principles. As said above, typical industrial computations are based on the dilute spray assumption, however proper collision models could be used to improve the physical description also in the spray dense region. The main drawback of the Eulerian-Lagrangian approach is related to the high number of droplets required to have statistically representative solutions that generally makes computational costs grow above affordable levels for industrial applications. In order to reduce computational costs, droplets are usually represented by numerical parcels, i.e. groups of droplets with the same properties.

The dispersed phase can also be modeled as a continuum in the so called Eulerian-Eulerian approach. This method is usually less time consuming, however it introduces many inaccuracies, basically related to the continuum hypothesis which does not allow different droplets to be distinguished from each other, which may not always be tolerable [48].

Another possible approach, the Probability Density Function method, uses a joint PDF transport equation to statistically describe the spray evolution [74]. The main advantage of the PDF approach is the ability to provide accurate droplet statistics in the whole domain whereas the Eulerian-Lagrangian approach gives reliable results only in those regions with high droplets concentrations. However the PDF approach requires a huge computational cost.

It should be noted that the previous classification is not exhaustive and other computational methods could be adopted, for example the SPH (Smoothed Particle Hydrodynamics) method [75, 76] which is being further developed during the FIRST project, or the ELSA (Eulerian-Lagrangian Spray Atomization) approach [77, 22] where a special treatment of primary atomization is included.

3.2 Development of a steady-state solver

One of the main aims of this research activity is to develop numerical tools suitable for industrial calculations. Thus, a good compromise between accuracy in the description of physical phenomena and computational cost has to be found. Despite the unsteady nature of droplet motion making the fully unsteady method the most straightforward way to model the spray behaviour, in many cases the industrial interest is on time-averaged quantities. The proposal of steady-state acceleration techniques for both reacting and non-reacting sprays is hence of primary interest, especially in gas-turbine applications where, differently from internal engines, the system often operates in stationary regime[1]. Therefore, a steady-state solver for reacting sprays has been introduced in the code. The Eulerian-Lagrangian modelling approach has been chosen due to the more physically consistent description of the interactions between droplets and gas-phase which follows basic physical principles, as described in Section 3.4.

In this section, mathematical and numerical modelling used in the steady-state approach developed in this work will be presented [78]. Before describing in detail the characteristics of the implemented solver, it is important to remember the basic features of the Eulerian-Lagrangian formulation:

- the gas-phase is solved in an Eulerian framework where conservation equations are applied to a control volume. In the case of fluid dynamics, conservation equations are usually numerically solved with the finite volume method [79]. The numerical domain is decomposed into a certain number of cells and conservation laws are applied to each one. This is the best choice for the description of a gaseous or liquid continuum since it implicitly allows the conservation of mass, momentum and energy fluxes.

[1] This does not mean that unsteady phenomena do not occur. Turbulent fields are always unsteady, however the mean field can often be considered stationary in a relative reference frame attached to solid walls. When also the mean flow is intrinsically non-stationary, unsteady approaches should be used for a more consistent solution of the flow field.

- A Lagrangian description is used for the spray. In the Lagrangian method, the dynamics of a certain amount of matter is followed over the space, thus this approach could be considered the natural choice to describe the evolution of a spray since it is composed by a finite number of particles that, differently from a continuum, move inside the domain without occupy all the volume. Trajectories are determined by volume force acting on the single particle and by the interactions with the continuum phase in which droplets are immersed.

It is important to point out that, in case of steady-state assumption, convergence of Eulerian-Lagrangian coupling could become an issue and the choice of convergence criteria is not straightforward. The reason is mainly related to the Eulerian-Lagrangian coupling source term fluctuations due to the stochastic formulation of many models describing the spray evolution, for example injection and turbulent dispersion models. In order to enhance numerical stability, under-relaxation of source terms is generally implemented [49] together with a proper strategy for parcel tracking able to generate source terms for a steady-state gas-phase solver with a low computational cost.

3.2.1 Droplet motion

Droplet dynamics is solved in a Lagrangian framework, thus numerical particles introduced in the computational domain are individually followed all over the domain during their evolution. The developed solver is based on the following assumptions:

- in order to reduce the computational cost, the spray is numerically represented by a cloud of parcels, where a parcel is a group of droplets with the same physical characteristics.
- The spray is assumed diluted so that no collision models are necessary and interaction between particles can simply be described using models derived for the single droplet.
- A two-way coupling is considered and the influence of spray evolution on the gas phase is accounted for by means of specific source terms in the conservation equations describing the gas-phase dynamics.

- Droplets are considered non rotating and spherical with non-sphericity accounted for by means of specific correction factors. In other words, droplets are treated as material points moving in the gaseous media (point droplet approximation).

Since the rotational speed is neglected, the particle dynamics is simply described by the Newton's second law which expresses a balance between forces acting upon a particle and its acceleration:

$$\frac{\mathrm{d}\mathbf{v}_p}{\mathrm{d}t} = \frac{1}{m_p}\sum_i \mathbf{F}_i \tag{3.1}$$

where $\mathbf{v}_p$ is the particle velocity and $\mathbf{F}_i$ represents a generic force acting upon the particle. In the implemented model, particle motion is determined only by drag, gravity and buoyancy forces. In this case Eq. 3.1 becomes:

$$\frac{\mathrm{d}\mathbf{v}_p}{\mathrm{d}t} = \frac{3}{4}\frac{\bar{\rho}}{d_p\rho_p}C_D\left(\widetilde{\mathbf{u}}-\mathbf{v}_p\right)\left\|\widetilde{\mathbf{u}}-\mathbf{v}_p\right\| + \frac{\rho_p-\bar{\rho}}{\rho_p}\mathbf{g} \tag{3.2}$$

where C_D is the drag coefficient, based on correlations for spheres, and $\bar{\rho}$ and $\widetilde{\mathbf{u}}$ are the carrier phase density and velocity derived from the gas-phase solution. All the other forces are neglected, in particular virtual mass, Basset, Saffman and Magnus forces [80, 16]. Basset forces are unsteady interactions due to acceleration of relative velocity between particle and gas-phase and for liquid or solid particles these forces could usually be neglected. The Saffman forces are related to the velocity gradients in the gas-phase and their effect could be important only in the injection zone and in regions close to the walls [51]. Finally, Magnus forces are generated by particle rotation and they are usually much smaller than drag forces.

During its life, a droplet may undergo heat transfer, evaporation, secondary breakup and interaction with gas-phase turbulence. Turbulent fluctuations could influence particle motion generally making the spray more dispersed in a phenomenon usually called turbulent dispersion. On the other hand, particles could also affect the gas-phase turbulence through the so called turbulent modulation as will

be better explained in Section 3.4.3. These phenomena are accounted for by means of specific interaction models.

The evolution of mass and energy of each parcel is computed by solving specific conservation equations. The mass and energy conservation equations for the single parcel can be written as [51]:

$$\frac{\mathrm{d}m_p}{\mathrm{d}t} = G_{ev} \tag{3.3}$$

$$m_p \frac{\mathrm{d}}{\mathrm{d}t}[c_{p,L}(T_p - T_{ref})] = \dot{Q}_p + G_{ev} h_v(T_p) \tag{3.4}$$

where G_{ev} is the mass evaporation rate, $c_{p,L}$ is the specific heat capacity of the liquid fuel, T_{ref} is the temperature of the reference state and h_v is the latent heat of vaporization. G_{ev} and $\dot{Q}_p$ are computed by means of specific evaporation and heat transfer models (see Section 3.4.2).

3.2.1.1 Numerical method

The Lagrangian tracking is performed following the approach described in [81]. A statistically representative number N_p of parcels is injected and their trajectories are computed by numerically integrating Eq. 3.2. Droplet injection is modeled by assigning droplet mass flow rate $\dot{m}_p$; thus, the total mass M_p of the representative sample is obtained starting from the Lagrangian time step by giving the number of time steps in which parcels are injected. The Lagrangian tracking starts from the injection location and proceeds until parcels either exit the domain or completely evaporate. The particle field in the whole domain is obtained by summing up the Lagrangian solution at each integration step. In this way, the whole history of the N_p parcels during the Lagrangian tracking is recorded. It is important to note that the assigned integration time step is actually decomposed into sub-integration time steps according to the relaxation times that characterize the physical phenomena related to droplet motion (heat transfer, boiling, drag and so on) and the time required to cross each computational cell.

Numerical integration of equations describing droplet dynamics is performed following the approach described in reference [51]. First of all, relaxation times are computed using the actual solution. In addition to the dynamical relaxation time defined in Eq. 2.8, relaxation time are also defined for evaporation and heat transfer processes (see [51] for further details). The actual integration time step is computed as the minimum of relevant time scales involved in parcel evolution:

$$\Delta t' = \min(\tau_x, \tau_{\Delta t_L}, \tau_c) \tag{3.5}$$

where τ_x is a generic relaxation time describing a characteristic time for the relevant physical processes, $\tau_{\Delta t_L}$ is the time necessary to complete the Lagrangian time step Δt_L imposed by the user and τ_c is the parcel residence time, that is the time that the parcel spends in the current cell of the gas-phase mesh. The new parcel position is computed by numerically integrating the parcel velocity with an explicit method:

$$\mathbf{x}_p^{(j)} = \mathbf{x}_p^{(j-1)} + \mathbf{v}_p^{(j-1)} \Delta t' \tag{3.6}$$

Then, equations describing parcel evolution are advanced in time. For example, in the case of momentum equation, the velocity at the j-th integration step is computed as:

$$\frac{\mathbf{v}_p^{(j)} - \mathbf{v}_p^{(j-1)}}{\Delta t'} = \frac{\widetilde{\mathbf{u}} - \mathbf{v}_p^{(j)}}{\tau_v^{(j-1)}} + \frac{\rho_p - \rho}{\rho_p}\mathbf{g}$$

$$\rightarrow \mathbf{v}_p^{(j)} = \left(\mathbf{v}_p^{(j-1)} + \widetilde{\mathbf{u}} \frac{\Delta t'}{\tau_v^{(j-1)}} + \frac{\rho_p - \rho}{\rho_p}\mathbf{g}\Delta t' \right) / \left(1 + \frac{\Delta t'}{\tau_v^{(j-1)}} \right) \tag{3.7}$$

where the gas-phase quantities are obtained by interpolating the gas-phase solution at the parcel location. Equations for mass and energy are solved using a similar approach (see reference [51]). At each integration step, source terms to be retrieved to the gas phase are computed. Table 3.1 summarizes expressions used for source term computation [16] (V is the volume of the computational cell).

Table 3.1: Source terms for the gas-phase.

Equation	$\mathbf{s_{p,k}}$
mass	$-\frac{1}{V}(m_p^{(j)} - m_p^{(j-1)})$
momentum	$-\frac{1}{V}[(m_p\mathbf{v}_p)^{(j)} - (m_p\mathbf{v}_p)^{(j-1)} - m_p\mathbf{g}\Delta t']$
energy	$-\frac{1}{V}[(m_p h_{s,p})^{(j)} - (m_p h_{s,p})^{(j-1)}]$
Y_F	$-\frac{1}{V}(m_p^{(j)} - m_p^{(j-1)})$

3.2.2 Gas-phase

The mathematical model for the continuous gas phase is represented by the Navier-Stokes equations, which state the laws of conservation of mass, momentum and energy. Unfortunately, in cases of industrial interest, the full numerical solution of the instantaneous balance equations is characterized by a very high computational cost due to the large number of time and length scales that have to be solved. Thus, a simplification is introduced by averaging the balance equations to describe only the mean flow field. In compressible flows, it has been found convenient to perform the averaging operation by means of the Favre (mass weight) average. A generic quantity Q is decomposed into $Q = \widetilde{Q} + Q''$ with the Favre-averaged value $\widetilde{Q}$ given by the following expression:

$$\widetilde{Q} = \frac{\overline{\rho Q}}{\overline{\rho}} \tag{3.8}$$

with:

$$\widetilde{Q''} = \frac{\overline{\rho(Q - \widetilde{Q})}}{\overline{\rho}} \tag{3.9}$$

where the overbar denotes the Reynolds averaged mean value. The application of the Favre-average to the Navier-Stokes equations, with additional simplifications due to steady-state assumption, leads to the following mathematical model used to solve the continuum phase [82]:

$$\frac{\partial \overline{\rho}\widetilde{u}_i}{\partial x_i} = S_{ev} \tag{3.10}$$

$$\frac{\partial \overline{\rho}\widetilde{u}_j\widetilde{u}_i}{\partial x_j} = -\frac{\partial \overline{\rho}\widetilde{u_j''u_i''}}{\partial x_j} - \frac{\partial \overline{p}}{\partial x_i} + \frac{\partial \overline{\tau}_{ij}}{\partial x_j} + \overline{F}_i + S_{m,i} \tag{3.11}$$

$$\frac{\partial \overline{\rho}\widetilde{u}_j\widetilde{Y}_k}{\partial x_j} = -\frac{\partial \overline{\rho}\widetilde{u_j''Y_k''}}{\partial x_j} - \frac{\partial \overline{J_j^k}}{\partial x_j} + \overline{\dot{\omega}}_k + S_{ev,k} \tag{3.12}$$

$$\frac{\partial \overline{\rho}\widetilde{u}_j\widetilde{h}_t}{\partial x_j} = -\frac{\partial \overline{\rho}\widetilde{u_j''h_t''}}{\partial x_j} + \frac{\partial}{\partial x_j}\left(\overline{J_j^h} + \overline{u_i\tau_{ij}}\right) + \overline{u_jF_j} + S_{h_t} \tag{3.13}$$

Energy equation (Eq. 3.13) has been written in terms of total generalized enthalpy, that is the sum of generalized enthalpy (formation plus sensible) and kinetic energy. However, sensible enthalpy is sometimes preferred. Following [83], the energy equation can be written in terms of sensible enthalpy as:

$$\frac{\partial \overline{\rho}\widetilde{u}_j\widetilde{h}_s}{\partial x_j} = \widetilde{u_i}\frac{\partial \overline{p}}{\partial x_i} + \overline{u_i''\frac{\partial p}{\partial x_i}} + \overline{\dot{\omega}}_T - \frac{\partial \overline{\rho}\widetilde{u_j''h_s''}}{\partial x_j} + \frac{\partial}{\partial x_j}\left(\overline{J_{s,j}^h}\right) + \overline{\tau_{ij}\frac{\partial u_i}{\partial x_j}} + S_h \tag{3.14}$$

where $\overline{\dot{\omega}}_T$ is the heat release due to combustion:

$$\overline{\dot{\omega}}_T = -\sum_k \Delta h_{f,k}^0 \overline{\dot{\omega}}_k \tag{3.15}$$

In the previous equations unclosed terms appear such as the Reynolds stresses $\widetilde{u_j''u_i''}$ which are usually computed using a turbulence model

(for example, under the Boussinesq assumption, the $k-\varepsilon$ or $k-\omega$ model), species $\widetilde{u_j'' Y_k''}$ and temperature $\widetilde{u_j'' T}$ turbulent fluxes which are usually closed using a gradient transport hypothesis. Laminar diffusive fluxes ($\overline{J_j^k}$ and $\overline{J_j^h}$ or $\overline{J_{s,j}^h}$) are neglected since they are usually very small compared to turbulent transport, assuming a sufficiently large turbulence level. Also the term $\overline{u_i'' \partial p / \partial x_i}$ is usually neglected in most RANS codes [83]. Finally species chemical reaction rates $\overline{\dot{\omega}}_k$ are computed by means of a proper combustion model whereas source terms due to the disperse phase (S_{ev}, S_m and S_h) derive from the solution of the spray. Further assumptions on fluid properties such as ideal gas equation of state, Newtonian modelling for viscous forces and constant transport properties are usually made in order to find the problem closure.

3.2.2.1 Numerical method

Conservation equations are resolved using the finite volume method. As regards the numerical implementation of the solution algorithm, a pure steady-state pressure-based solver exploiting SIMPLE loop [84] to solve for the pressure velocity coupling has been employed. Density variations are accounted for by solving the energy equation in terms of sensible enthalpy and assuming ideal gas behaviour. In the simulations presented in this dissertation, finite-volume discretization is achieved by means of Total Variation Diminishing or Self-Filtered Central Differencing schemes for the convective terms and central differencing for the diffusive terms [79]. Aspects related to spatial discretization and mesh resolution are very important for the success of a numerical simulation and the computational grids used in all the cases investigated in this work are the result of a mesh independence analysis.

3.2.3 Two-way coupling

The overall solution procedure consists in repeatedly solve disperse and continuous phase using the approaches described in previous sections. A basic iteration cycle can be considered composed by two different steps. First of all the Lagrangian tracking is performed using the most updated Eulerian flow field that is available. When a

parcel traverses a cell, mass, momentum and energy source terms are recorded and averaged with the source terms released by all the other particles. Thus, at the i-th Lagrangian tracking, source terms in a generic cell are computed as:

$$S_p^{(i)} = \frac{\dot{m}_p}{M_p} \sum_{k=1}^{\hat{N}} s_{p,k}^{(i)} \tag{3.16}$$

where $\hat{N}$ is the cumulative number of parcels traversing a cell and $s_{p,k}^{(i)}$ is the contribution of the k-th parcel to the source term computation. Then source terms are passed to the gas-phase and held constant during Eulerian computation. In order to improve convergence rates, Lagrangian tracking, and thus the update of the coupling source terms, is generally performed only after the under-relaxed Eulerian fields are solved a certain amount of times.

As previously mentioned and as also discussed in many references [49, 85], when the steady state formulation is considered, it is often important to use under-relaxation techniques in order to improve the computation stability of source terms. The classical approach to perform under-relaxation of particles/droplets source terms uses the following expression:

$$S^{(i)} = \alpha S_p^{(i)} + (1 - \alpha) S_p^{(i-1)} \tag{3.17}$$

where $S^{(i)}$ denotes the new computed generic source term at the i-th Lagrangian iteration, $S^{(i-1)}$ is the source term at the previous iteration and α is the under-relaxation factor (a real number between 0 and 1).

During the development of the solver a method based on moving average has also been implemented. From a purely mathematical point of view, the proposed approach consists in calculating source terms to be assigned to the Eulerian solver by averaging the last $\bar{N}$ solutions of the Lagrangian tracking. $\bar{N}$ should be large enough to smooth fluctuations of source terms and thus to obtain a really representative mean value. Furthermore, in principle, this approach could allow us to perform Lagrangian iterations with a smaller number of parcels being the representative population composed by all

the parcels considered in the $\bar{N}$ iterations. Let's consider the i-th Lagrangian iteration. Mean source terms at the end of the iteration are computed as:

$$\bar{S}_p^{(i)} = \frac{1}{\bar{N}} \sum_{k=i-\bar{N}+1}^{i} S_p^{(k)} \tag{3.18}$$

The main drawback of this approach is that $\bar{N}$ solutions of Lagrangian tracking have to be recorded for the computation of the moving average requiring a lot of memory resources. The moving average has been numerically implemented using the following strategy to save allocated memory. Besides $\bar{S}_p^{(i)}$ another mean value $\bar{S}_{\bar{N}/2}$ is computed. It represents the mean source terms in $\bar{N}/2$ Lagrangian iterations and this value is updated every $\bar{N}/2$ Lagrangian trackings. The moving average is evaluated as follows:

$$\bar{S}_p^{(i)} = \frac{1}{\bar{N}}(\bar{N}\bar{S}_p^{(i-1)} + S_p^{(i)} - \bar{S}_{\bar{N}/2}) \tag{3.19}$$

The use of this strategy to approximate the moving average allows us to not store all the data of the last $\bar{N}$ Lagrangian iterations but only two mean values. In particular the term $\bar{S}_{\bar{N}/2}$ allows us to avoid abrupt changes in source term values. Another possible strategy could be the use of an averaged value which considers all the Lagrangian solutions performed from the beginning of the simulation. In respect to a standard averaging procedure which considers all the Lagrangian iterations, the moving average approach let the effect of initial values be less significant; the sensibility to initial values could be further reduced by using a weighted moving average.

3.3 Unsteady solver

Although in an industrial context the main interest is usually on mean quantities, in some cases the temporal evolution of a phenomenon could be required. Time resolved simulations are usually much more computationally expensive than steady-state simulations, thus they

are used only when the interest is in time histories or in the transient from initial conditions to a steady-state behaviour or when the flow cannot be considered stationary and only unsteady solutions are physically consistent. The unsteady simulations performed in this work are based on an unsteady Eulerian-Lagrangian solver already present in the base version of the code. This solver has been further developed and integrated with all the models developed in this work (models for injectors and interaction models). In the unsteady approach no particular strategy is necessary for the coupling between gas and dispersed phases. Both phases are integrated in time with the same time step dt using a segregated approach: first tracking of parcels is performed by integrating parcel equations along dt, then source terms are computed and finally gas-phase equations are solved introducing an evolutive term (time-derivative) for each quantity and advancing in time the solution of dt. Unsteady gas-phase computations are based on PIMPLE algorithm which combines SIMPLE loop with the pressure implicit with splitting operator (PISO) algorithm to evaluate second pressure correction and update both pressure and velocity explicitly. In the unsteady simulations presented in this work, time discretization was generally achieved by means of first order or second order backward Euler schemes.

It should be noted that in both unsteady and steady-state computations the Lagrangian tracking is performed by solving the same equations. However the two approaches are very different from each other. In the steady-state approach, in each Lagrangian computation the evolution of a representative cloud of parcel is completely resolved: all the parcels are injected and tracked all over the domain until they completely evaporate or exit the domain (thus in each Lagrangian computation, once the Lagrangian time step dt_L is chosen, the integration is performed many times until all parcels have completed their evolution). The complete evolution history is then used for the computation of steady-state source terms. On the other hand, in the unsteady approach, each Lagrangian computation solves the tracking of parcels present in the domain for just one time step. The complete evolution of the spray is obtained only at the end of the simulation. Fig. 3.2 briefly summarizes the main characteristics of the global iteration loop used for the Eulerian-Lagrangian coupling in unsteady and steady-state computations.

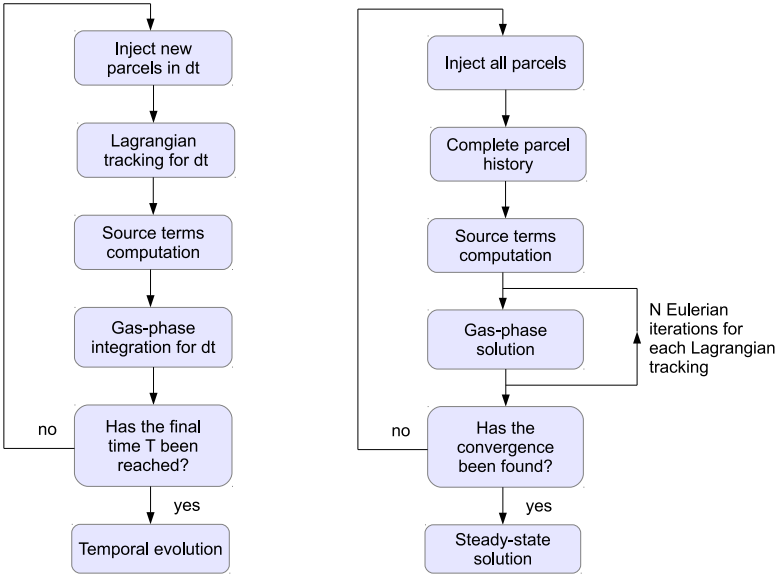

(a) Unsteady. (b) Steady-state.

Figure 3.2: Unsteady and steady-state solution algorithms.

3.4 Gas phase - droplet interactions

During their dynamics, droplets interact with the gas phase exchanging mass, energy and momentum. Since a dilute spray is considered, the inter-particle spacing can be assumed sufficiently high to make negligible the influence exerted on the droplet dynamics by the neighbour particles. For example, in the case of evaporation, if the inter-spacing is small the fuel mass evaporated from a particle could affect the evaporation of the near droplets since the evaporated fuel enhances the fuel mass fraction near the droplet surface. The dilute spray approximation allows us to neglect the interactions between different droplets and models developed for the single droplet can be applied to the whole spray. In the following, proper models to handle the most important interactions will be introduced.

3.4.1 Drag forces

Droplet and gas-phase exchange momentum through the so called *drag force* which represents the aerodynamic interaction between the two phases. The general expression used for the drag force is:

$$F_D = \frac{1}{2} C_D \frac{\pi d^2}{4} \rho_g \left(\widetilde{\mathbf{u}} - \mathbf{v}_p\right) \left\|\widetilde{\mathbf{u}} - \mathbf{v}_p\right\| \tag{3.20}$$

The drag coefficient C_D is computed using expressions derived for spheres with a further correction to capture the effects of particle distortion due to the interaction with the gas-phase[2] (the drag coefficient is highly dependent on the particle shape, thus it is desirable to take into account the effects of droplet distortion). In this work, the possible distortion of the droplet has been taken into account assuming that the drag coefficient varies linearly between the value of a sphere and the one of a disk [86]:

$$C_D = C_{D,sphere}(1 + 2.632y) \tag{3.21}$$

where y is a parameter varying between 0 and 1 which gives a measure of the distortion. This value is computed using the approach introduced in the TAB breakup model (see Section 3.4.4.1). As regards the drag coefficient of a sphere, the following expressions have been used [87, 88, 89, 90]:

$$C_{D,sphere} = \begin{cases} \frac{24}{Re_P}\left(1.0 + \frac{1}{6} Re_P^{2/3}\right) & \text{for } Re_P \leq 1000 \\ 0.424 & \text{for } Re_P > 1000 \end{cases} \tag{3.22}$$

3.4.2 Evaporation models

A reliable description of the spray evaporation process is fundamental for the prediction of the fuel distribution inside the combustion

[2]Particle shape may be significantly distorted and, if the distortion reaches a critical value, breakup may occur as discussed in Section 3.4.4.

chamber and the subsequent combustion process. As stated above, since a dilute spray is considered, models developed for single droplet evaporation can be used. Thus, in the following, single droplet evaporation models will be presented.

Droplet evaporation is characterized by the presence of many simultaneous processes [48]:

- Heat transfer between carrier phase and droplet.
- Mass transfer between gas-phase and droplet.
- Heat transfer by convection and conduction inside the droplet.
- Mass transfer inside the droplet (only for multi-component fuels).
- Phase change at the droplet interface.

In general, for a realistic model of droplet evaporation, all the transport processes, around and inside the droplet, should be taken into account. However models able to consider all the relevant phenomena are very complex and extremely expensive and cannot be used for the prediction of spray evaporation (such models are generally used for the investigation of the single droplet evaporation). If it is possible to identify some dominant transport processes, simplified models can be developed.

Simplifications are usually based on the droplet Biot number which gives a measure of the relative importance between external heat transfer from the gas-phase to the droplet and internal conduction (h is the heat transfer coefficient and λ_d is the fuel conductivity) [48]:

$$Bi = \frac{hd}{2\lambda_d} \tag{3.23}$$

If the Biot number is small ($Bi \to 0$) the heat conduction inside the droplet is predominant over the external heat transfer and the temperature inside the droplet levels out very quickly. In this case, the so called *uniform temperature models*, where the droplet temperature is considered uniform and thus no internal transport is solved, can be used. On the other hand, when the Biot number is very large

($Bi \to \infty$), the conduction process inside the droplet is very low and only the droplet surface can be considered heated by the external heat transfer. In this case, the *thin skin approximation* can be applied. For intermediate cases the conduction inside the droplet should be solved with a high computational effort.

In the conditions of interest for gas turbine applications the uniform temperature model generally leads to a reasonable description of the evaporation process [48] with a low computational cost. Therefore, in this work this class of evaporation models was considered.

3.4.2.1 Uniform temperature model

The uniform temperature model does not consider any temperature variation in the interior of the droplet (homogeneous temperature). Although the uniformity assumption, the temperature can vary during the droplet evolution as a consequence of the heat transfer with the gas-phase until a steady-state condition is reached. In the steady-state condition all the energy given to the droplet through heat transfer with the gaseous phase is completely used by the evaporation process and the temperature of the droplet does not vary. The temperature reached in the steady-state condition is usually called *wet bulb temperature*.

In order to derive the basic equations of the uniform temperature model, it is useful to decompose the domain into three different regions (see also Fig. 3.3):

- the gas-phase, which represents the region infinitely far from the droplet. The temperature and vapour concentration are those of the carrier phase.
- A layer located at the interface between liquid and gas, where transport processes can be observed.
- The droplet interior.

Under the main assumptions of spherical symmetry, single component fuel, absence of convection and quasi-steady behaviour of the gas-phase, the following equation describing, in spherical coordinates, the fuel mass fraction conservation from the droplet surface to the

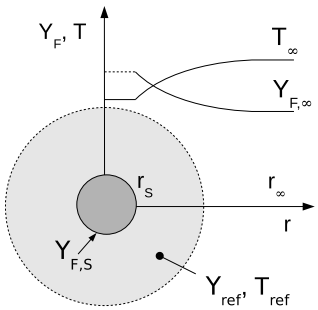

Figure 3.3: Regions considered in the uniform temperature model (adapted from [49]).

far-field can be written:

$$\begin{aligned} & r^2 \rho v \tfrac{dY_F}{dr} = \tfrac{d}{dr}\left(r^2 \mathscr{D} \rho \tfrac{dY_F}{dr}\right) \\ & Y_F = Y_{F,\infty} \qquad \text{for } r \to \infty \\ & Y_F = Y_{F,S} \qquad \text{for } r = r_S \end{aligned} \tag{3.24}$$

The solution of this equation leads to the following expression for the droplet evaporation rate [50]:

$$\dot{m}_d = -2\pi d \rho_{ref} \mathscr{D}_{ref} \ln(1 + B_M) \tag{3.25}$$

where ρ_{ref} and $\mathscr{D}_{ref}$ are the density and the mass diffusivity of the air vapour mixture at a reference condition. As suggested by Faeth [89], physical properties should be determined using the following reference temperature and composition [90] (1/3-rule):

$$\begin{aligned} T_{ref} &= T_d + 1/3(T_\infty - T_d) \\ Y_{ref} &= Y_{F,S} + 1/3(Y_{F,\infty} - Y_{F,S}) \end{aligned} \tag{3.26}$$

Furthermore, in Eq. 3.25 the Spalding mass transfer number B_M has been introduced:

$$B_M = \frac{Y_{F,S} - Y_{F,\infty}}{1 - Y_{F,S}} \tag{3.27}$$

$Y_{F,\infty}$ is derived from the gas-phase solution whereas further assumptions have to be used for the computation of the fuel vapour mass fraction at the interface. As reported in reference [91], two different choices are possible:

- Equilibrium assumption: the fuel vapour is in equilibrium with the liquid, thus the vapour partial pressure is equal to the saturation value at the droplet temperature ($p_{sat}(T_d)$) evaluated by means of the Clausius-Clapeyron equation.

$$Y_{FS,eq} = \frac{\chi_{S,eq}}{\chi_{S,eq} + (1 - \chi_{S,eq})\Theta} \tag{3.28}$$

  $\chi_{S,eq} = p_{sat}(T_d)/p_g$ is the equilibrium surface molar fraction and $\Theta = W_g/W_F$ is the ratio between molecular weights of gas-phase and fuel vapour.

- Non-equilibrium assumption: the non-equilibrium Langmuir-Knudsen law is incorporated through the definition of the vapor mole fraction at the droplet surface:

$$\chi_{FS,neq} = \chi_{FS,eq} - \Big(\frac{L_\kappa}{d/2}\Big)\beta \tag{3.29}$$

  where L_κ is Knudsen layer thickness defined as [91]:

$$L_\kappa = \frac{\mu_g \sqrt{2\pi T_d R/W_v}}{\alpha_e Sc_g p_g} \tag{3.30}$$

  α_e is the molecular accommodation coefficient (assumed equal to unity), R is the universal gas constant whereas the dimensionless evaporation parameter β is computed as:

$$\beta = -\left(\frac{3Pr_g\tau_v}{2}\right)\frac{\dot{m}_d}{m_d} \tag{3.31}$$

  where τ_v is the dynamical relaxation time for Stokes flows (Eq. 2.9). Finally, the fuel vapour mass fraction at the droplet surface is

computed with an expression equivalent to Eq. 3.28:

$$Y_{FS,neq} = \frac{\chi_{FS,neq}}{\chi_{FS,neq} + (1 - \chi_{FS,neq})\Theta} \tag{3.32}$$

In some cases it is useful to introduce the so called Sherwood Sh number:

$$Sh = \frac{-\left(\frac{\partial Y_F}{\partial r}\right)_{r_S}}{(Y_{F,S} - Y_{F,\infty})/2r_S} = 2\frac{\ln(1 + B_M)}{B_M} \tag{3.33}$$

which allows us to rearrange Eq. 3.25 in the following form:

$$\dot{m}_d = -\pi d \rho_{ref} \mathscr{D}_{ref} Sh B_M \tag{3.34}$$

Eq. 3.25 was derived under the assumption of negligible convective heat transfer. Abramzon and Sirignano [88] included the effect of both convection and Stefan flow by means of a corrected Sherwood number (B_M is computed using the equilibrium assumption [91]):

$$Sh = Sh^* \frac{\ln(1 + B_M)}{B_M} \tag{3.35}$$

$$Sh^* = 2 + \frac{Sh_0 - 2}{F(B_M)} \tag{3.36}$$

$$Sh_0 = 2 + 0.552 Re_P^{1/2} Sc_g^{1/3} \tag{3.37}$$

The function $F(B_M)$ represents the correction due to droplet evaporation and it was derived from the boundary layer theory:

$$F(B_M) = (1 + B_M)^{0.7} \frac{\ln(1 + B_M)}{B_M} \tag{3.38}$$

Finally, the evaporation source term G_{ev} used in the equation describing the evolution of a parcel is simply computed as (N_d is the number of real droplets contained in a parcel and can be easily computed starting from parcel mass, liquid density and parcel diameter):

$$G_{ev} = N_d \dot{m}_d \tag{3.39}$$

Another possible formulation for the computation of the droplet evaporation rate, widely used in commercial codes and also implemented in the base version of OpenFOAM, is the one derived from the work of Borman and Johnson [92, 51]:

$$\dot{m}_d = -\pi d \mathscr{D} Sh_0 \rho_v \ln\Big(\frac{p_g - p_{v,\infty}}{p_g - p_{v,s}}\Big) \tag{3.40}$$

where $\mathscr{D}$ is the mass diffusivity, Sh_0 is the previously introduced Sherwood number, p_g is the pressure of the gas mixture whereas $p_{v,s}$ and $p_{v,\infty}$ are the partial pressure of the fuel vapour at the droplet surface and far from it, respectively; ρ_v is the fuel vapour density.

3.4.2.2 d^2-model

The so called d^2-model [93] can be considered a special case of the uniform temperature model under the assumption of steady-state evaporation. In this model the droplet heat-up period is neglected and the droplet temperature is considered uniform and constant with a value equal to the wet bulb temperature.

Rearranging Eq. 3.25, the following relation can be obtained:

$$\frac{\mathrm{d}d^2}{\mathrm{d}t} = -\frac{8\rho_{ref}\mathscr{D}_{ref}}{\rho_d}\ln(1 + B_M) = -k_v \tag{3.41}$$

As a consequence of constant temperature assumption, $k_v = \text{const}$, meaning that the square of the droplet diameter decreases linearly with time. k_v is usually called *evaporation constant*. This model can be considered the limiting case of the uniform temperature model after the heat-up transient (see Fig. 3.4).

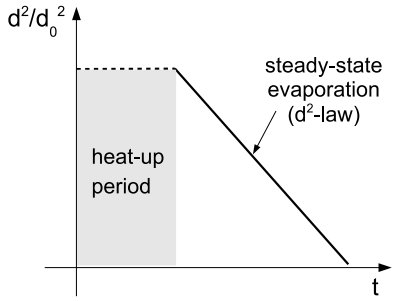

Figure 3.4: Schematic representation of heat-up period and steady-state evaporation.

3.4.2.3 Heat transfer

In the uniform temperature model, the droplet temperature is evaluated by numerically solving Eq. 3.4 during the Lagrangian tracking of the parcel. In order to solve such equation, the term representing heat transfer from the gas-phase to the droplet surface $\dot{Q}_p$ has to be modelled.

The convective heat transfer from the gas phase to the droplet is calculated from [92, 81, 51]:

$$\dot{Q}_d = \pi d k_g Nu f (T_\infty - T_d) \tag{3.42}$$

where f is a factor [91, 51] which corrects the amount of heat exchange due to the presence of mass transfer (Stefan flow):

$$\begin{aligned} f &= \frac{z}{e^z - 1} \\ z &= -\frac{c_{p,v}\dot{m}_d}{\pi d k_g Nu} \end{aligned} \tag{3.43}$$

$c_{p,v}$ is the fuel vapour specific heat at constant pressure, k_g is the gas-phase mixture thermal conductivity (evaluated at the reference condition) and Nu the Nusselt number evaluated using the Ranz-Marshall correlation [94]:

$$Nu = 2.0 + 0.6 Re_P^{1/2} Pr^{1/3} \tag{3.44}$$

with the Prandtl number defined as:

$$Pr = \frac{c_{p,g}\mu_g}{k_g} \tag{3.45}$$

A more general formulation which includes the definition of the so called *Spalding heat transfer number* can also be used as reported in references [88, 89]. Corrections to the Nusselt number for the presence of evaporation, similar to the one presented for the Sherwood number, can be also be applied to this formulation [88].

Finally, the heat transfer source term $\dot{Q}_p$ in the parcel energy equation (see Eq. 3.4) can be computed as:

$$\dot{Q}_p = N_d \dot{Q}_d \tag{3.46}$$

where N_d is the number of real droplets contained in a parcel (computed starting from parcel mass, liquid density and parcel diameter).

3.4.2.4 Assessment of single droplet evaporation models

The behaviour of the implemented evaporation models and their reliability in the description of the evaporation process of fuel of technical interest were assessed by performing numerical simulations of the single droplet evaporation and comparing numerical results with experimental measurements. Two different sets of experimental measurements were considered. A first assessment was performed using data published in [91] for hexane, then the experiments of Ghassemi et al. [95] for a kerosene droplet in a quiescent medium were considered. In the first case, droplet evaporation was predicted using the expression of Eq. 3.40 together with equilibrium assumption and the Ranz-Marshall correlation for heat transfer whereas for the kerosene droplet both this formulation and the Abramzon and Sirignano model were evaluated and compared with each other.

In order to perform comparisons with experimental, the evolution of droplet diameter against time is required. Therefore, simulations were performed using the unsteady version of the code, whose basic structure was already implemented in the base version of OpenFOAM (see Section 3.3). Fig. 3.5 shows the computational domain used in

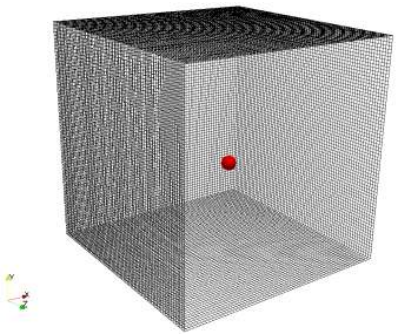

Figure 3.5: Computational domain used in the single drop simulation.

the simulation of single droplet evaporation. A droplet with initial diameter and temperature equal to d_0 and $T_{d,0}$ respectively is placed at the center of a cubic domain discretized by means of a hexahedral structured mesh. Initial conditions for the gas-phase are the same used in experiments. In case of a non-quiescent medium, the relative motion between droplet and gas-phase was replicated by imposing an initial velocity to the droplet and disabling forces acting on it (no drag and gravitational forces) in order to avoid changes in relative velocity due to dynamic interactions. Fuels have been modelled as mono-component liquids with thermophysical properties derived from experimental correlations found in literature [96, 91].

In Fig. 3.6 evaporation history of hexane droplet is compared with experimental data [91] in terms of temporal evolution of the squared diameter. After an initial transient heat-up period, the squared diameter decays with a constant rate meaning that a steady-state evaporation condition has been reached. Numerical results show a good agreement with experimental measurements. As regards the length of the heat-up period, in general it is a function of initial droplet size and temperature, droplet composition and ambient conditions.

Fig. 3.7 shows the evolution of the squared diameter and temperature of a kerosene droplet at a gas pressure equal to 1.0 MPa and different ambient temperatures. Also in this case, after an initial heat-up transient during which the droplet reaches an almost steady-state temperature, the decay rate of the squared diameter becomes

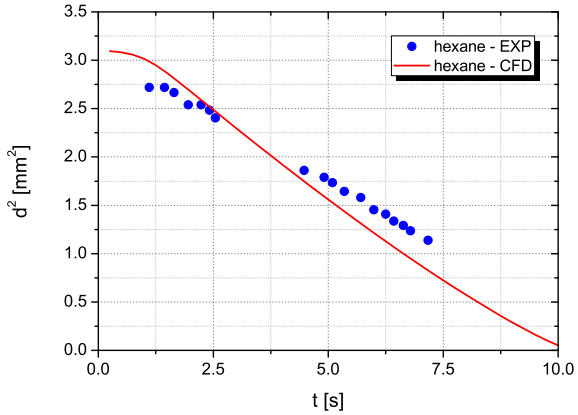

Figure 3.6: Temporal evolution of droplet squared diameter ($T_g = 437$ K, $T_{d,0} = 281$ K, $d_0 = 1.76$ mm, $Re_{P,0} = 110$, $p_g = 1.01$ bar).

constant as described by the d^2-law for steady state-evaporation. It should be noted that during the heat-up period the droplet diameter becomes greater than its initial value (the ratio d^2/d_0^2 is greater than one) as a consequence of changes in droplet temperature. This result is in agreement with both experimental measurements [95] and other numerical computations [96]. Furthermore, it should also be noted that temperature values at the end of evaporation are in good agreement with computational results presented in [96], as a confirmation of a reliable implementation of both evaporation and heat transfer models. In Fig. 3.8, comparisons with experimental data by Ghassemi et al. [95] are reported. Experimental measurements were performed in high temperature and pressure conditions, very close to typical gas turbine applications. Comparisons with experiments are performed in terms of the evaporation coefficient k_v of the d^2-law, extracted from the linear part of the numerical evaporation history curve using a least square regression. The experimental trend is quite well captured, especially at low ambient temperatures, with the evaporation rate which increases with both ambient temperature T_g and pressure p_g. Important discrepancies arise at high values of T_g, how-

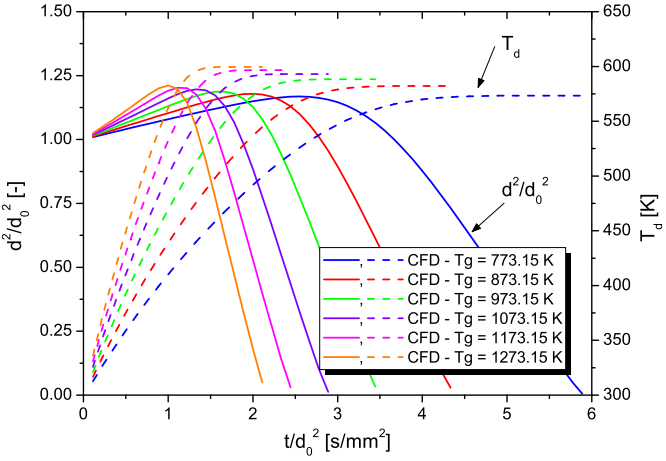

Figure 3.7: Evolution of droplet diameter and temperature at $p_g = 1.0$ MPa (Borman and Johnson [92] evaporation model).

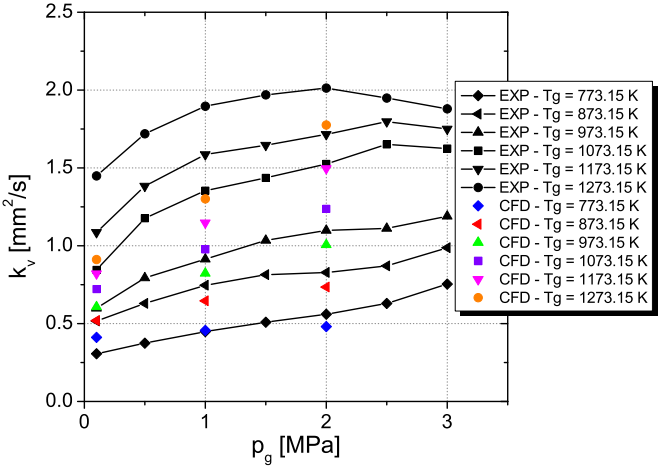

Figure 3.8: Evaporation rate at different ambient temperatures and pressures (Borman and Johnson [92] evaporation model).

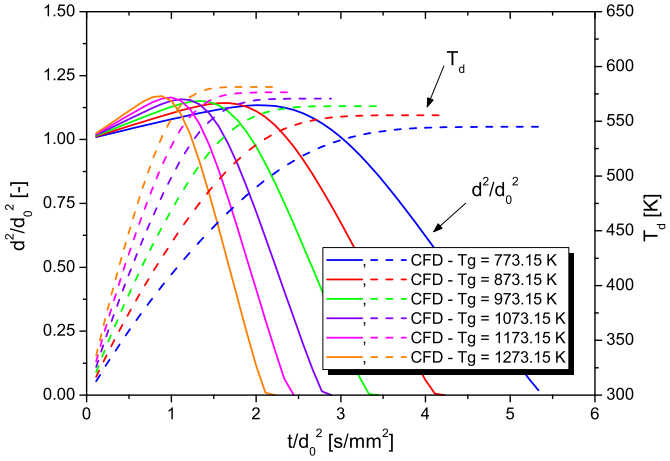

Figure 3.9: Evolution of droplet diameter and temperature at $p_g = 1.0$ MPa (Abramzon and Sirignano [88] evaporation model).

ever the obtained results can be considered satisfactory since in typical gas turbine applications (see Chapter 6) evaporation is completed near the injector exit where the gas-phase temperature remains in the range where a good agreement with experiments was obtained. The high values of evaporation rate observed in experiments at high temperatures could be due to the presence of radiative heat transfer which was not considered in the present numerical simulations.

Fig. 3.9 and Fig. 3.10 show the same results obtained with the evaporation model of Abramzon and Sirignano (see Eqs. 3.28 and 3.35). The evaporation constant k_v is slightly smaller than the values predicted with the Borman and Johnson [92] model, however, as shown in Fig. 3.9, this does not lead to higher evaporation times since simulations performed with the Abramzon and Sirignano model are also characterized by a smaller heat-up period.

It could also be interesting to compare the present results with data published in Lefebvre [32]. In Fig. 3.11 the steady-state evaporation constant of gasoline (JP 4), kerosene (JP 5) and diesel oil (DF 2) taken from [32] is reported. Generally speaking, these values are quite smaller compared to measurements performed by Ghassemi

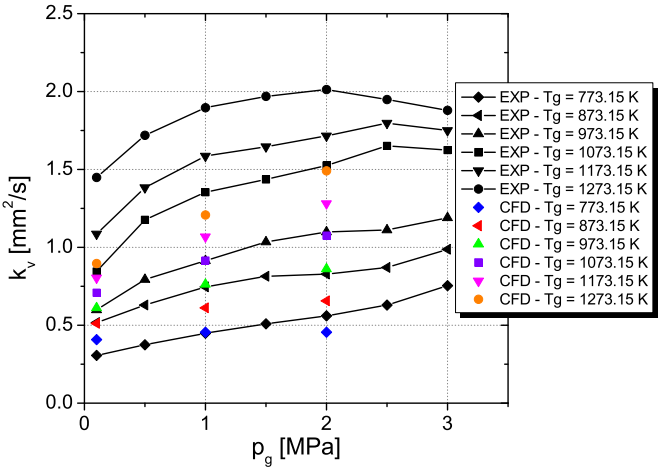

Figure 3.10: Evaporation rate at different ambient temperatures and pressures (Abramzon and Sirignano [88] evaporation model).

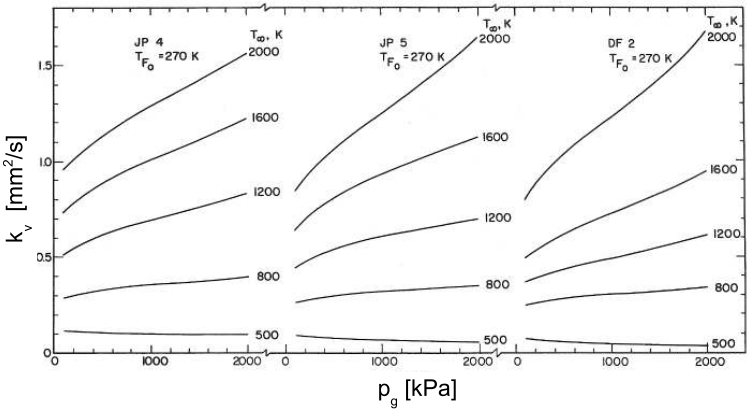

Figure 3.11: Effect of pressure and temperature on steady-state evaporation constant for gasoline (JP 4), kerosene (JP 5) and diesel oil (DF 2) - (taken from [32]).

et al. [95] and in fairly good agreement with numerical results obtained in the present work. It should be noted that the measuring of the evaporation constant is not so easy to be performed and the discrepancies between the results obtained in the different experimental investigations could be ascribed to different measurement techniques and experimental apparatus as well as differences in liquid properties which directly influence the determination of the evaporation constant.

3.4.3 Interaction with turbulence

Turbulent structures present in the flow may interact with the particles and, depending on the Stokes number (see Eq. 2.10), they could alter the particle trajectory determining the spreading of the spray jet in a process usually referred to as *turbulent dispersion*. Since in RANS computations only the mean flow is resolved, in order to predict a proper distribution of particles and thus a reliable fuel mass fraction field after evaporation, proper models able to introduce the effects of turbulent dispersion are required. Furthermore, as also shown in Fig. 2.1, in the two-way coupling regime particle dynamics could also promote the production or the dissipation of turbulence. This phenomenon, which is not yet clearly understood, is usually called *turbulent modulation*. Generally speaking, sufficiently small particles tend to follow the turbulent flow, thus the turbulent kinetic energy contained in these structures is used to accelerate the particles and dissipation of turbulence kinetic energy is enhanced. On the other hand, large particles do not follow the turbulent flow field due to their high inertia. In this case additional turbulence kinetic energy is generated since particles act as obstacles for the gas phase leading to the formation of wake structures and velocity gradients which enhance the local turbulence (it should be noted that experimental findings not always support this observations [97, 98]).

In this work the turbulent dispersion has been accounted for using a stochastic approach. The parcel tracking is performed by adding a turbulent fluctuation to the mean gas-phase velocity. In practice, at each Lagrangian time step, the gas-phase velocity considered for the parcel evolution is computed as:

$$\widetilde{\mathbf{u}}' = \widetilde{\mathbf{u}} + \mathbf{u}' \tag{3.47}$$

where $\widetilde{\mathbf{u}}$ is the mean velocity vector derived from the gas-phase solution whereas $\mathbf{u}'$ is a fluctuation imposed by the turbulent dispersion model. For this purpose, the turbulence is assumed to be isotropic with a Gaussian probability distribution in the fluctuating velocity whose standard deviation is given by $\sigma_{ij} = (2k/3)^{1/2}$ (k is the turbulence kinetic energy computed by means of turbulence models). This distribution is randomly sampled at the beginning of each Lagrangian time step giving the velocity fluctuation to be added to the mean field. The present implementation follows the strategy described in [99] where the fluctuating component $\mathbf{u}'$ is added to the mean gas-phase velocity only if the Lagrangian time step is less than the characteristic time of the turbulent fluctuation computed as:

$$\tau_{turb} = \min\left[\frac{k}{\varepsilon}, \frac{k^{3/2}}{\varepsilon}\frac{C_\mu^{3/4}}{U_R}\right] \tag{3.48}$$

where $C_\mu = 0.09$. Another possible strategy is the one proposed by Gosman and Ioannides [81] in their stochastic approach which is based on the definition of a time interval over which the droplet interacts with the randomly sampled velocity field. Considering the fluctuation representative of a turbulent eddy, the interaction time interval is computed as the minimum of the turbulent eddy lifetime and the residence time of the droplet in the eddy.

When the turbulent dispersion model is activated, the fluctuating gas-phase velocity $\widetilde{\mathbf{u}}'$, computed as in Eq. 3.47, directly replaces $\widetilde{\mathbf{u}}$ in the equation of droplet motion (Eq. 3.2).

As far as turbulence modulation is concerned, in the frame of this work no correction was adopted. In general, turbulence modulation is considered by adding source terms determined from the Lagrangian solution in the equations of the turbulence model. The reader interested in this topic is addressed to references [100, 101, 49] where models and applications are presented.

3.4.4 Secondary breakup modelling

As discussed in Section 2.2.2, during its evolution a droplet may disintegrate in smaller droplets because of the interaction with the

gas-phase. It is very important to consider this phenomenon in spray simulations since smaller droplets usually lead to higher spray evaporation rates affecting the fuel distribution inside the combustor. In the current implementation, the parcel undergoing breakup changes its diameter according to the breakup model but the parcel mass remains constant (new parcels are not generated and the tracking of the same representative particle is continued). Obviously the number of real droplets represented by the parcel changes according to the new diameter. In the following, the secondary breakup models considered in this work will be described.

3.4.4.1 TAB model

The first secondary breakup model considered here is the Taylor Analogy Breakup (TAB) model devised by O'Rourke and Amsden [102]. The droplet distortion, caused by the interaction with the gas phase, is described as a one-dimensional, forced, damped, harmonic oscillation similar to the one of a spring-mass system. The droplet deformation is defined as $y = 2x/r$, where x is the deviation of the droplet equator from its undeformed position. Assuming that the droplet viscosity acts as a damping force and the surface tension as a restoring force, it is possible to write the following equation [87]:

$$\ddot{y} + \frac{C_d \mu_p}{\rho_p r^2}\dot{y} + \frac{C_k \sigma}{\rho_p r^3} y = \frac{C_F \rho_g U_R^2}{C_b \rho_p r^2} \tag{3.49}$$

The integration of this equation leads to an expression for parcel deformation:

$$\begin{aligned} y(t) = We_C + \quad & \exp(-t/t_d)\Big[(y_0 - We_C)\cos(\omega t) \\ & + \tfrac{1}{\omega}\Big(\tfrac{dy_0}{dt} + \tfrac{y_0 - We_C}{t_d}\Big)\sin(\omega t)\Big] \end{aligned} \tag{3.50}$$

where $We_C = WeC_F/(C_k C_b)$, $We = \rho_g U_R^2 r/\sigma$ (Weber number based on droplet radius), $\omega^2 = C_k\sigma/(\rho_p r^3) - 1/t_d^2$, $1/t_d = C_d\mu_p/(2\rho_p r^2)$, $C_k = 8$, $C_d = 5$, $C_F = 1/3$ and $C_b = 0.5$.

Eq. 3.50 is solved with initial conditions $y_0 = 0$ and $\dot{y}_0 = 0$. If the distortion exceeds unity ($y > 1$), that is the deviation of the

particle equator from its equilibrium position has become larger than half the droplet radius, the parcel is assumed to breakup. The size of the child droplet is computed by equating the energy of the parent droplet to the combined energy of the child droplets obtaining the following expression for the droplet radius (with $K = 10/3$):

$$\frac{r_{child}}{r_{parent}} = \Big[1 + 0.4Ky^2 + \frac{\rho_p r_{P,parent}^3}{\sigma}\dot{y}^2\Big(\frac{6K-5}{120}\Big)\Big]^{-1} \tag{3.51}$$

After breakup, the deformation parameters y_0 and $\dot{y}_0$ of the child droplet are set equal to zero.

3.4.4.2 ETAB model

The Enhanced TAB model (ETAB) [103] uses the same droplet deformation mechanism described for the TAB model with a different law for the computation of the diameter of child droplets as the deformation y becomes higher than unity:

$$\frac{r_{child}}{r_{parent}} = \exp(-K_{br}t) \tag{3.52}$$

The breakup constant K_{br} depends on the breakup regime:

$$K_{br} = \begin{cases} k_1\omega & \text{for } We \leq We_t \\ \\ k_2\omega\sqrt{We} & \text{for } We > We_t \end{cases} \tag{3.53}$$

where $k_1 = 2/9$, $k_2 = 2/9$, $We_t = 80$ (critical Weber number for stripping breakup) and ω is computed as in the TAB model. The TAB model often leads to an underestimation of breakup times (droplets undergo breakup much closer to the atomizer). In order to overcome this limitation, a negative value can be used for $\dot{y}_0$, as described in [103].

3.4.4.3 CAB model

The Cascade Atomization and Breakup (CAB) model [104] is similar to the ETAB model and uses the same deformation law and the

same evolution equation for the computation of the droplet radius after breakup. The main difference is the definition of the breakup constant K_{br}. Three different regimes are defined:

$$K_{br} = \begin{cases} k_1\omega & \text{for } 5 < We < We_{t1} \\ k_2\omega\sqrt{We} & \text{for } We_{t1} < We < We_{t2} \\ k_3\omega We^{3/4} & \text{for } We > We_{t2} \end{cases} \tag{3.54}$$

with:

$$k_2 = k_1 \frac{\sqrt{1 - \frac{1}{2}\left(\frac{C_k C_b}{C_F We_{t1}}\right)}}{\operatorname{acos}\left(1 - \frac{C_k C_b}{C_F We_{t1}}\right)} \tag{3.55}$$

and

$$k_3 = \frac{k_2}{We_{t2}^{1/4}} \tag{3.56}$$

The model constants C_b, C_F and C_k are equal to the same constants of the TAB model whereas $k_1 = 0.05$, $We_{t1} = 80$ (critical Weber number for stripping breakup) and $We_{t2} = 350$ (critical Weber number for catastrophic breakup).

3.4.4.4 MCAB model

The Modified CAB (MCAB) model is an extension of the CAB model with an improvement in the description of the breakup process in the bag breakup regime [105]. The proposed modification is based on the observation that some of the model constants show a dependence on the injection Weber number (that is the Weber number of the droplet immediately after primary atomization). In particular, a great dependence is observed for the constant k_1, thus the following correlation

is proposed for the modification of the bag breakup coefficient:

$$k_1(We_0) = \begin{cases} k_1^{low} & \text{for } We_0 < We^{min} \\ k_{factor} We_0^{k_{power}} & \text{for } We^{min} < We_0 < We^{max} \\ k_1^{high} & \text{for } We_0 > We^{max} \end{cases} \tag{3.57}$$

where $k_1^{low} = 0.1$, $k_1^{high} = 0.01$, $k_{factor} = 6.7$, $k_{power} = -0.7$, $We^{min} = 55$, $We^{max} = 10000$ and the reference Weber number We_0 is computed as the maximum between the injection and the local Weber numbers in order to take into account the dependence mentioned above:

$$We_0 = \max(We_{inj}, We) \tag{3.58}$$

3.4.4.5 Evaluation of different secondary breakup models

The secondary breakup model is very important for the determination of spray penetration and in general fuel distribution in the combustion zone. The behaviour of the different breakup models was assessed by performing an unsteady simulation of the pilot injector of the PERM injection system in a tubular combustor configuration. The numerical domain consists in a sector of 90 degrees of the entire combustor. Fig. 3.12 shows a detail of the hexahedral computational mesh[3] in a region near the pilot injector. The computation was initialized using the gas-phase solution obtained in a RANS single-phase simulation of the system. Second order discretization schemes were used for convective terms in the gas-phase equations whereas a second order backward Euler scheme was employed for time discretization. As regards boundary conditions, a total temperature $T_{g,0} = 655$ K and a total pressure $p_{g,0} = 13.5$ bar were imposed at the inlet boundary whereas at the outlet boundary a static pressure equal to $p_g = 12.9$ bar was

[3]The mesh has been generated by Engin - Soft (EST) during the FIRST project.

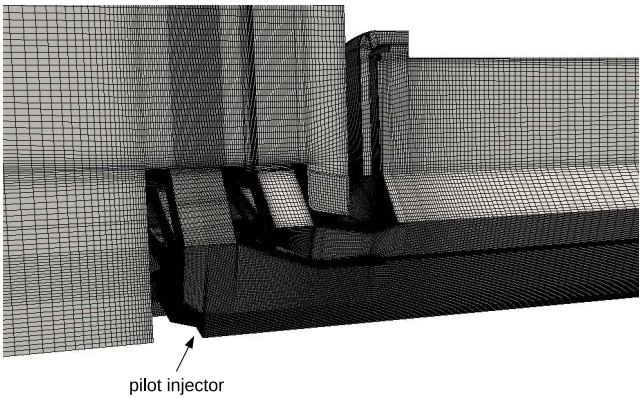

Figure 3.12: Computational mesh.

assigned. The k-ω SST turbulence model was used for this investigation. A prescribed population of droplets was injected from $t = 0$ s to $t = 0.003$ s analysing the temporal evolution of spray angle and penetration.

Three different secondary breakup models were compared with each other. Fig. 3.13 shows a qualitative representation of the spray shape at the end of the simulated time whereas in Fig. 3.14 the temporal evolution of spray penetration and spray angle (as defined in Section 2.4.3) is reported together with the flow field in the injection region. The obtained results confirm that the TAB model tends to predict small breakup times with droplets that disintegrate in a very short distance after injection. As a consequence droplets evaporate close to the injector and the spray penetration is smaller compared to the values predicted with the other models. The ETAB model predicts a slightly bigger spray penetration whereas very high values of axial penetration were found with the MCAB model.

The very high values of axial penetration predicted with the MCAB model can be explained considering the normal penetration and the flow field in the injection region reported in Fig. 3.14(c) and Fig. 3.14(d) respectively. In the simulation performed with the MCAB model the spray is also characterized by a higher normal penetration. A large number of droplets penetrate into the primary flow and are carried

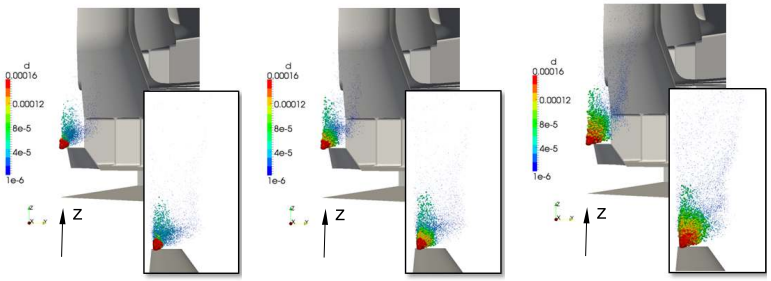

(a) TAB. (b) ETAB. (c) MCAB.

Figure 3.13: Droplet population predicted by different secondary breakup models.

away by the high velocity flow causing the very high value of axial penetration. Finally, as far as spray angle is concerned, the investigated models give very similar results.

Unfortunately, experimental measurements on this kind of injector are not available (as described in Section 1.2.4, the pilot injector is located inside the primary duct of the PERM injection system where measurements are very difficult to be performed), thus it is not possible to determine what is the model which best represents the actual behaviour of the injector. However, this analysis has allowed us to highlight the great influence exerted by the secondary breakup model on the droplet dynamics. Furthermore, more in general, it should be noted that the characteristics of droplets downstream of the injection location are determined by both injection characteristics and secondary breakup. Therefore, when also a primary breakup model is used, in the absence of detailed measurements on droplet population after primary breakup, the characteristics of droplets downstream of the injection location have to be regarded as the result of the combination of primary and secondary breakup models. This important aspect will be considered again in Chapter 5 where a primary breakup model for liquid films will be described in detail.

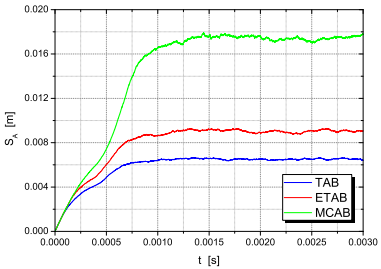

(a) Axial penetration.

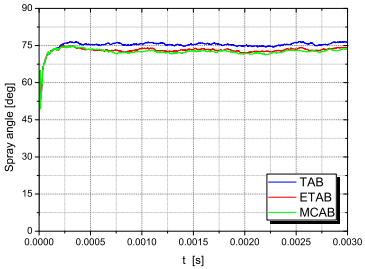

(b) Spray angle.

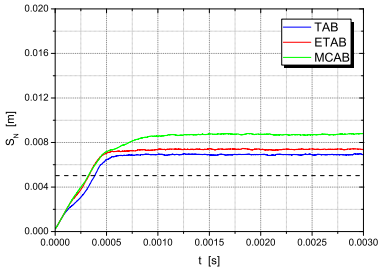

(c) Normal penetration.

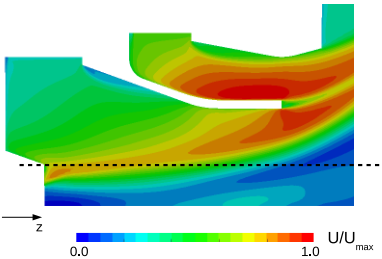

(d) Magnitude of the mean velocity field.

Figure 3.14: Comparison between different secondary breakup models.

3.5 Spray combustion

In order to simulate a burning spray, a closure has to be provided for the mean reaction rate $\overline{\dot{\omega}}_k$. Spray turbulent combustion is a very complex field since many physical phenomena could interact with each other determining the local and global flame structures. An essential characteristic of spray combustion is that the fuel is injected into the combustion chamber in liquid form and evaporation and diffusion of fuel vapour into the surrounding gas-phase precede chemical reactions between fuel and oxidizer. As a result, spray combustion shows features of both non-premixed and premixed combustion [10]. Basically, two different limiting cases can be considered [32]:

- heterogeneous combustion;

- homogeneous combustion.

In *heterogeneous combustion* the droplet evaporates and acts as a source of fuel vapour which burns with the surrounding oxidant as a diffusion flame around the droplet. The local flame structure will influence the evaporation process [16] and the burning characteristics. This limiting case is also called *single droplet combustion*. The local flame behaviour can be obtained by developing models describing the evolution of the flame front around the burning droplet. When droplets are grouped in clusters different heterogeneous combustion regimes may occur. A very common classification is the one proposed by Chiu et al. [106] who developed group combustion models. A spherically symmetric droplet cloud is considered. This cloud could be completely or partially surrounded by a diffusion flame depending on the group combustion number G which is a function of the number of droplets in the cluster N_d and mean droplet separation distance L_d:

$$G = 3(1 + 0.276Re^{1/2}Sc^{1/3})LeN_d^{2/3}\overline{r}/L_d \tag{3.59}$$

where Re, Le and Sc are the Reynolds, Lewis and Schmidt numbers respectively and $\overline{r}$ is the instantaneous average droplet radius. The group combustion number represents the ratio of the rate of the droplet vaporization to the transport of gaseous species by diffusion. As also described in [107], the value of G has a great effect upon the flame location and distributions of temperature, fuel vapour and oxygen. Small values of G ($G < 10^{-2}$) correspond to the single droplet combustion. For greater values of G, internal group combustion, external group combustion and external sheath combustion regimes can be found. More details about the different regimes can be found in references [106, 10, 107]. Other possible classifications of heterogeneous burning modes are also possible as reported in the review by Penny et al. [10]. The presence of a flame front around the droplet is also influenced by the relative motion between the droplet and the gas-phase. At high relative velocities, an envelope flame (a flame front that completely encloses the droplet) cannot exist and side flames or wake flames appear [108, 48]. Considerations about envelope flame stability can be found in reference [16]. As observed

by Koch [48], it should be noted that these combustion regimes are usually identified in very simplified cases usually far from technical applications. Interaction between turbulence field and group combustion could strongly alter the combustion process and different flame structures may appear.

The other limiting case is the *homogeneous combustion* where the fuel is completely vaporized and mixed with air prior to combustion and the local flame structure is similar to the one of gaseous fuel-air mixtures. This is the typical case of droplets evaporating in a hot (burning) environment. The fuel vapour mixing with the environment is fast and no local flame structure influences the droplet evaporation process. Combustion models used for homogeneous combustion are very similar to the one used for gaseous fuels (a good review of gaseous fuel combustion models can be found in [82]). Some modifications to the basic equations are sometimes introduced in order to account for droplet evaporation. For example Chrigui et al. [109] presented a model for partially premixed, pre-vaporized, three-dimensional kerosene spray flames based on the solution of two scalars, mixture fraction and reaction progress variable, where source terms due to droplet evaporation appear in transport equations of the mixture fraction and its variance. The last two quantities are used as input conditions to determine the local flame behaviour following the flamelet approach (the turbulent flame front can be locally described as a collection a laminar flame structures). In the limit of very fast evaporation, the spray flamelet model reduces to the usual gaseous flamelet model [82]. However, more general spray counterflow flamelets, where the presence of droplets is considered in the flamelet solution, have been studied in many works [110] although they are not extensively used.

Flames of technical interest are usually simulated assuming a homogeneous combustion. However, as shown in a recent investigation performed by Beck et al. [111], homogeneous and heterogeneous modes could be present at the same time. In the work performed by Beck et al., a lean partially prevaporized swirled spray flame, similar to the one encountered in advanced lean burn combustors, is experimentally studied. Because of the high temperature in the combustion chamber, droplets start to evaporate before reaching the flame front. The evaporated fuel is mixed with air and from this mixture a par-

tially premixed flame burning at lean condition is generated. The droplets which are not completely evaporated cross the flame front and are ignited by the hot flame and single droplet combustion modes appear in the region downstream of the flame front. Droplet flames may extinguish because of lack of oxidiser or turbulent flame quenching, however high temperatures are able to re-ignite the droplets. However, despite these recent findings, single droplet combustion is usually neglected in typical industrial computations.

The spray flame generated by the PERM injection system has some features in common with the flame investigated by Beck et al. [111]. However, in the tubular combustor configuration considered in this work, especially at high pressure operating conditions, droplets completely evaporate close to the injection system and they are not expected to cross the flame front. Thus, in the simulations performed in this work, single droplet combustion will be neglected. As regards the homogeneous combustion, the mean reaction rate will be computed by means of the Eddy Dissipation Concept (EDC) model which has demonstrated a good accuracy level in many investigations on turbulent spray flames [112, 113, 114].

3.5.1 EDC combustion model

The Eddy Dissipation Concept (EDC) combustion model, proposed by Magnussen [115], is a direct extension to non-premixed flames of the Eddy Breakup (EBU) closure [116], initially devoted to turbulent premixed combustion. Under the assumption of infinitely fast chemistry, the model assumes that the reaction is controlled by the turbulent mixing and occurs in small turbulent structures called *fine structures* where the reactants can be considered mixed at molecular level.

Let's consider a generic global chemical mechanism composed of M reactions and N species ($\mathscr{M}_k$ is a symbol for species k and ν'_{kj}, ν''_{kj} are the molar stoichiometric coefficients of species k in reaction j):

$$\sum_{k=1}^{N} \nu'_{kj} \mathscr{M}_k \leftrightarrow \sum_{k=1}^{N} \nu''_{kj} \mathscr{M}_k \quad \text{for} \quad j = 1, ..., M$$

The species mean reaction rate $\overline{\dot{\omega}}_k$ is expressed as:

$$\overline{\dot{\omega}}_k = W_k \sum_{j=1}^{M} (\nu''_{kj} - \nu'_{kj}) R_j \tag{3.60}$$

where R_j is the molar reaction rate of the j-th reaction.

Non-dimensional analysis of the turbulence energy cascade process [115] allows the definition of important quantities that can be directly exploited in the computation of the mean reaction rate. Two main quantities are required: a measure of the amount of gas mixture involved in the combustion and a measure of the residence time of the mixture in the fine structure. The mass contained in the reaction zone can be computed starting from the volume fraction of the fine structure, expressed as:

$$\gamma^* = \left(\frac{3 C_{D2}}{4 C_{D1}^2} \right)^{3/4} \left(\frac{\nu \varepsilon}{k^2} \right)^{3/4} \tag{3.61}$$

where $C_{D1} = 0.135$ and $C_{D2} = 0.5$. As regards the residence time of reacting mixture inside the fine structure, the following expression can be used:

$$\tau^* = \left(\frac{C_{D2}}{3} \right)^{1/2} \left(\frac{\nu}{\varepsilon} \right)^{1/2} \tag{3.62}$$

Combining these two quantities, the ratio between the mass flow rate exchanged by the fine structure and the local mass of the flow can be found:

$$\dot{m}^* = \frac{\gamma^*}{\tau^*} \tag{3.63}$$

The reaction rate R_j of the j-th reaction is computed as:

$$R_j = \overline{\rho} \dot{m}^* Y_{j,min} = \overline{\rho} \frac{\gamma^*}{\tau^*} Y_{j,min} \tag{3.64}$$

where $Y_{j,min}$ represents the limiting mass fraction between reactants and products and it is evaluated as:

$$Y_{j,min} = \min\left[\frac{\widetilde{Y}_k^{(R)}}{\nu'_{kj}W_k^{(R)}}, \beta\frac{\sum_P \widetilde{Y}_k^{(P)}}{\sum_P \nu''_{kj}W_k^{(P)}}\right] \tag{3.65}$$

where (R) and (P) refer to reactants and products respectively and β is a model constant. The limitation due to the products is usually not included in multi-step mechanisms. Eq. 3.64 is sometimes expressed in a simplified form [82, 83]:

$$R_j = A\overline{\rho}\frac{\varepsilon}{k}Y_{j,min} \tag{3.66}$$

where A is a model constant (usually taken equal to 4.0). Effects of finite rate chemistry can be introduced in the formulation by computing R_{kj} as the minimum between the EDC reaction rate expressed by Eq. 3.64 (or Eq. 3.66) and an Arrhenius type chemical reaction source:

$$R_j = \min\left[R_j^{(EDC)}, R_j^{(ARR)}\right] \tag{3.67}$$

3.6 Validation of the steady-state spray solver

In this Section the validation of the implemented steady-state spray solver is presented. Validation has been performed using literature test cases and comparisons with results obtained with the commercial code Ansys CFX-13.0. The first test case considers the motion of solid particles in a swirled flow. Since solid particles are considered, interaction between gas-phase and droplets is reduced to drag forces and turbulent dispersion only (the turbulence induced by particle motion, often referred to as turbulence modulation, is not considered here). In the second case evaporation in turbulent flows is considered, thus the coupling between continuous and disperse phases is extended to mass and energy exchanges. The third case that has been selected is a

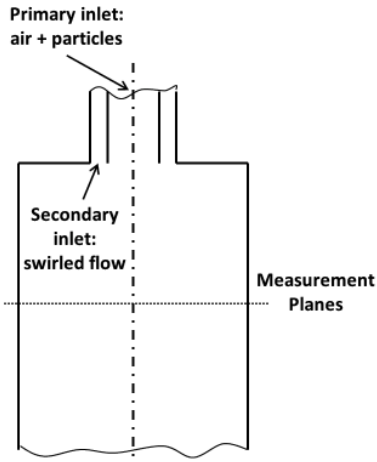

Figure 3.15: Test case scheme (*Test-1*).

configuration investigated at Sydney University. Experimental measurements for both non-reacting and reacting sprays are available. Two different fuels were tested: acetone and ethanol. In the following the results obtained in a non-reactive condition will be presented with the main aim of further assessing the implementation of mass and energy coupling between gas-phase and disperse phase. Further validation of the implemented solver in reproducing turbulent reacting two-phase flows will be performed in a real burner by comparing results obtained with the present solver with the ones obtained with Ansys CFX (see Section 6.3.2).

3.6.1 TEST-1

The first test case consists in an isothermal swirling particulate two-phase flow, experimentally investigated by Sommerfeld and Qiu [117]. Fig. 3.15 schematically represents the experimental configuration, basically a vertical test section with two different flow circuits for the primary and secondary annular flows. Glass particles, with a given size distribution, move down from a reservoir and enter the measurement section together with the primary flow whereas a swirled flow

Table 3.2: Air flow and particle conditions (*Test-1*).

Air flow	
Mass flow rate of primary jet	9.9 g/s
Mass flow rate of secondary jet	38.3 g/s
Inlet Reynolds number (D=64 mm)	52400
Swirl number	0.47
Particles	
Particle mean number diameter	45.5 μm
Particle material density	2500 kg/m^3
Particle mass flow rate	0.34 g/s

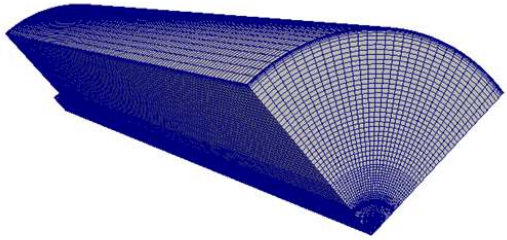

Figure 3.16: Computational mesh (*Test-1*).

issues from the secondary inlet. PDA measurements were performed at different planes normal to the main chamber axis. In Table 3.2 the main flow conditions are given; for geometrical features and all the other details see reference [117].

As shown in Fig. 3.16, the experimental rig was modelled as a 90 degrees sector with cyclic boundary conditions on lateral faces. The computational domain was discretized by means of a multi-block hexahedral structured mesh of about 470000 elements. Fixed value velocity boundary condition was imposed in both primary and secondary inlets whereas a statistically representative population of 12500 parcels was injected at the main chamber entrance representing the experimental size distribution with a Rosin-Rammler function. Turbulence effects on the mean field were accounted for using

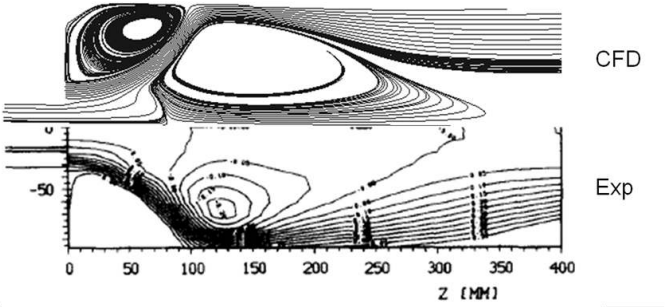

Figure 3.17: Comparison between numerical and experimental [117] stream lines (*Test-1*).

the k-ω SST turbulence model [118] whereas particle turbulence dispersion was included using the stochastic dispersion model presented in Section 3.4.3. As regards droplet-wall interaction, solid surfaces were modelled as rebounding walls.

Fig. 3.17 shows a comparison between experimental and numerical 2D streamlines in an axial-radial plane. The extension of the recirculation zones is well predicted both in the centre and on the left corner.

In Fig. 3.18 radial profiles of gas-phase axial and tangential mean velocities are reported at two different planes. A good agreement between experimental and numerical results is reached far away from the inlet while near the inlet some discrepancies arise. The difficulty of the present model to reproduce gas-phase velocity can be ascribed to the general inability of turbulence models to properly predict swirled flows. It should be noted that similar differences were also found by Chrigui in his thesis work [49] using the k-ε turbulence model. Fig. 3.19 shows how particle velocity profiles well reproduce experimental data at those locations where the gas-phase flow was well predicted. It is important to note that experimental measurements are referred to particular droplet size classes (30, 45, 60 μm) whereas numerical results presented in the figure consider all the particles together through a mass averaged value.

As a further assessment and validation of the implemented steady-state approach, in Fig. 3.20 numerical results obtained with the imple-

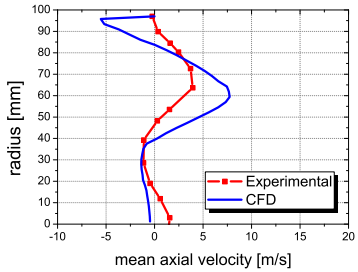

(a) Axial velocity at plane z=85 mm.

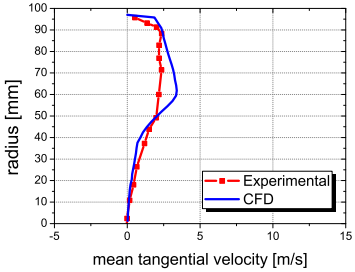

(b) Tang. velocity at plane z=85 mm.

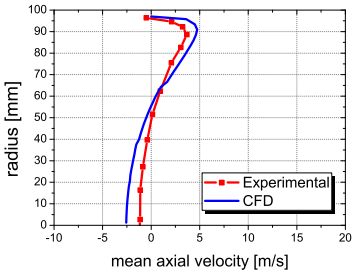

(c) Axial velocity at plane z=195 mm.

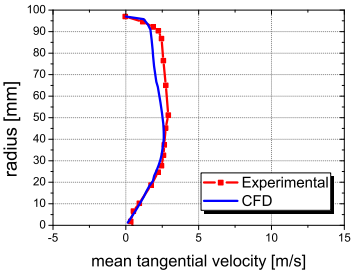

(d) Tang. velocity at plane z=195 mm.

Figure 3.18: Gas-phase mean velocity profiles (*Test-1*).

mented solver are compared with results obtained with the unsteady solver already present in the base version of OpenFOAM. The two different solvers gave the same mean velocity profiles for both gas and disperse phases proving that, in case the interest is only on time averaged quantities, the use of a steady solver might substitute traditional unsteady solvers that are more computationally expensive.

Finally, in Fig. 3.21 two size-velocity correlation plots are reported at different points in the domain. Comparisons with experimental data [117, 119] showed that numerical results are less dispersed than experimental ones following the same trend observed in other works [119].

Summarizing, comparisons with simulations performed with the unsteady solver show the correct implementation of momentum inter-

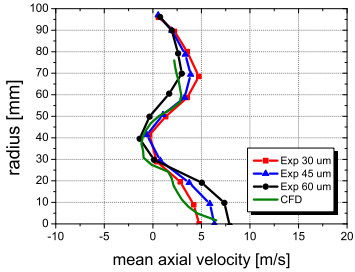

(a) Axial velocity at plane z=85 mm.

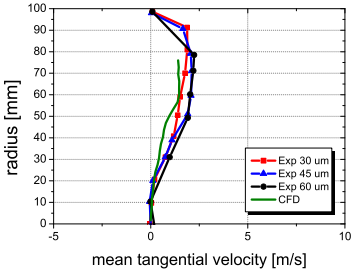

(b) Tang. velocity at plane z=85 mm.

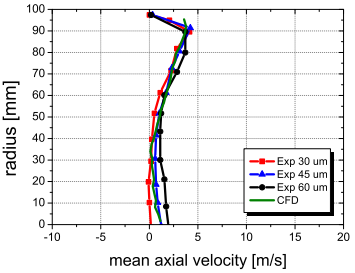

(c) Axial velocity at plane z=195 mm.

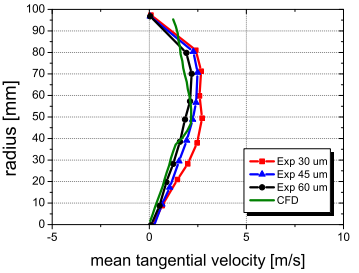

(d) Tang. velocity at plane z=195 mm.

Figure 3.19: Particle mean velocity profiles (*Test-1*).

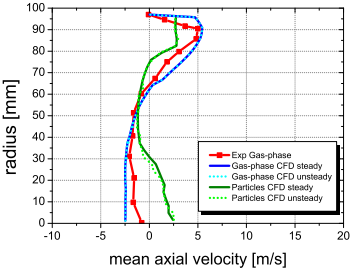

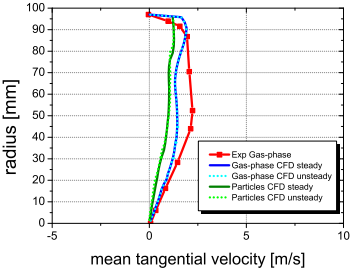

Figure 3.20: Comparison between steady state and unsteady solvers at plane z=112 mm (*Test-1*).

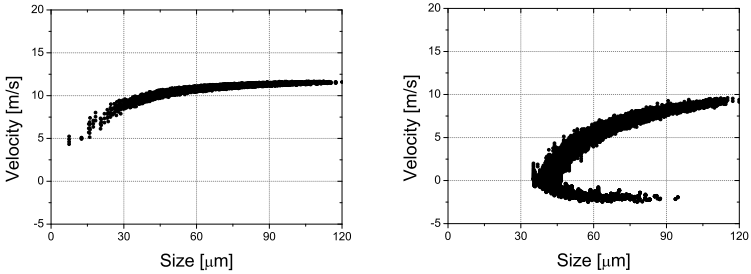

(a) Point (0.0 m, 0.0 m, 0.052 m) (b) Point (0.0 m, 0.0 m, 0.112 m)

Figure 3.21: Particles size-velocity correlations (*Test-1*).

actions between gas-phase and particles. Comparisons with experiments allow us to highlight some general considerations that have to be taken into account when Eulerian-Lagrangian simulations are performed. Particle dynamics is strongly influenced by the gas-phase field (this is especially true for droplets characterized by a very small dynamic relaxation time), therefore an accurate prediction of spray distribution requires proper models able to correctly reproduce the most important flow structures. The problem of swirled flows is of particular interest since swirl stabilization is often used in modern lean burn aero-engines.

3.6.2 TEST-2

The second test case that was used to evaluate the capabilities of the implemented solver considers evaporation of isopropyl alcohol in a turbulent environment. Fig. 3.22 shows a schematic representation of the test rig experimentally investigated by Sommerfeld and Qiu [120]. It consists of a main cylindrical chamber where heated air is supplied through an annulus. Droplets are injected at the centre of the annulus by means of a hollow cone injector. Geometrical details are given in reference [120] together with all flow conditions. Two different simulations were performed, without and with the presence of the spray. Table 3.3 summarizes the main flow parameters of such simulations.

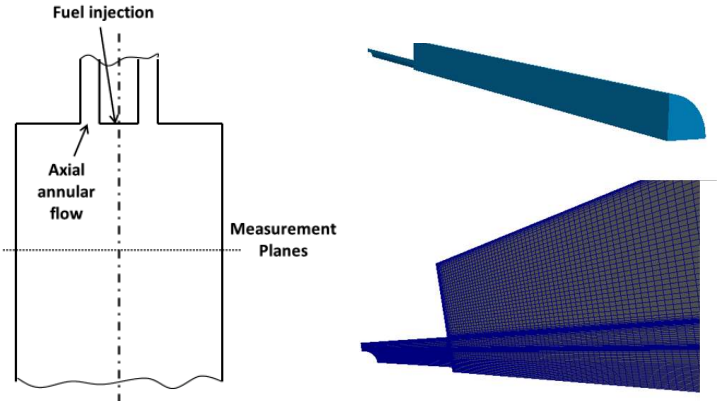

Figure 3.22: Test case scheme, computational domain and mesh (*Test-2*).

Table 3.3: Air flow and particle conditions (*Test-2*).

	Single-phase flow	**Case 1**
Diameter nozzle holder [mm]	40	40
Air volume flow rate [m^3/s]	0.032	0.034
Air mass flow rate [g/s]	29.0	32.6
Maximum air velocity [m/s]	18.0	18.0
Maximum air temperature [°C]	100	80
Liquid mass flow rate [g/s]	-	0.44
Liquid temperature at nozzle exit [°C]	-	32

The computational domain reproduces a 90 degrees sector of the test rig. A multi-block hexahedral structured mesh of about one million elements was used (see Fig. 3.22). The inlet annular duct has been included in the computational domain in order to have a developed flow at the main chamber entrance. A fixed value velocity was imposed at air inlet, ambient pressure was set at the outlet and

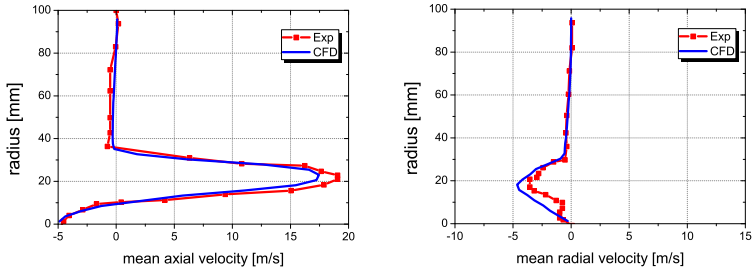

Figure 3.23: Mean velocity radial profiles at plane z=25 mm for single-phase flow (*Test-2*).

no-slip condition together with experimental temperature profile was imposed at walls. A representative population of 16000 parcels was used. Following [49], particle injection was modelled by means of eight concentric injectors. Droplet mean diameter and injection velocity were assigned to each injector. A reflecting wall condition was imposed at solid surfaces, the uniform temperature model derived from the work of Borman and Johnson [92] (see Eq. 3.40) was used for droplet evaporation whereas secondary breakup model was not included.

As shown in the previous test case, a reliable prediction of spray evolution requires a proper characterization of gas-phase dynamics. Fig. 3.23 shows a comparison between numerical results and experimental data of the case without spray in a plane normal to the main chamber axis. A good agreement was reached and similar results were also obtained in the other measurement planes.

In Fig. 3.24 and Fig. 3.25 results of the simulation with spray at two different planes are considered. Results obtained with the implemented steady-state solver have been compared with both experimental data and results obtained with Ansys CFX using the same computational setup. A reasonable agreement between numerical simulation and experiments both in terms of axial velocity and particle mean diameter was obtained. Present results are also in good agreement with CFX simulations showing that the implemented code has an equivalent behaviour to one of the most common commercial

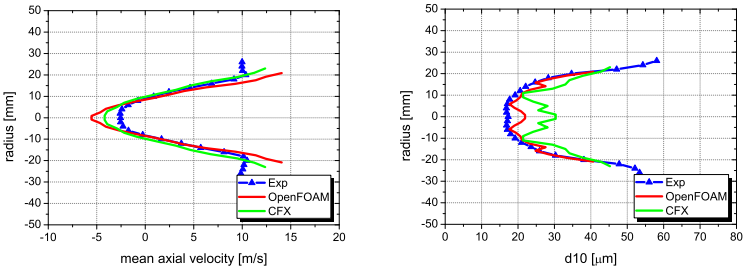

Figure 3.24: Particle mean axial velocity and diameter profiles at plane z=25 mm (*Test-2*).

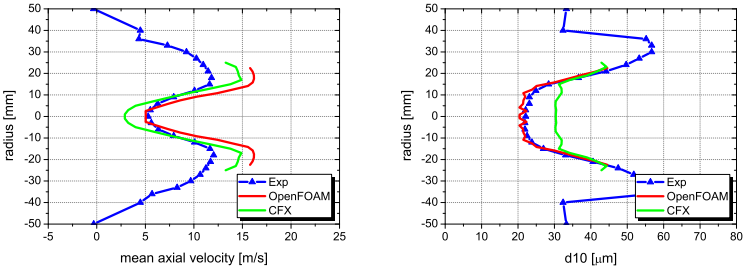

Figure 3.25: Particle mean axial velocity and diameter profiles at plane z=50 mm (*Test-2*).

codes. The two codes are almost equivalent also in terms of CPU time required by the simulation, with the implemented solver which shows slightly better convergence rates.

If Fig. 3.25 is considered again, it is possible to note that in this simulation particle turbulent dispersion is not well predicted with experimental results that show a higher dispersion of the liquid particles. As shown in the figure, no parcel is predicted by numerical simulations at high radius denoting the presence of a more coherent spray compared to experiments where a non-negligible droplet mass flux was measured also at $r > 25$ mm [120]. A better agreement with experiments could be obtained with an improvement of the turbulent dispersion model or by using numerical approaches able to give a detailed solution of the turbulent field. Although the development

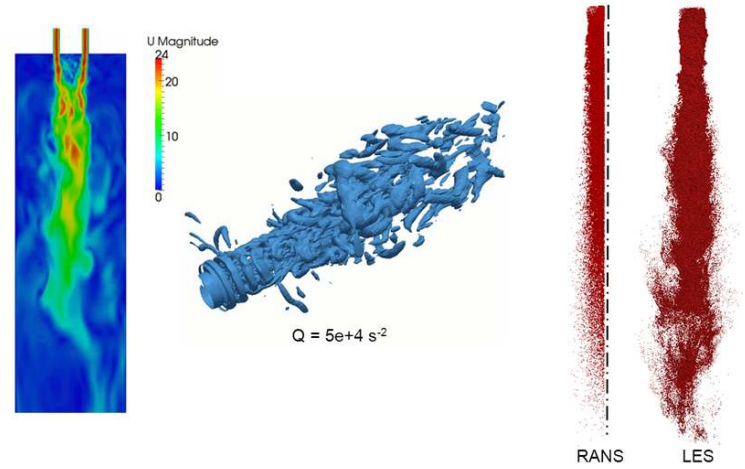

Figure 3.26: Gas-phase solution obtained using the LES approach and comparison between RANS and LES particle tracking (*Test-2*).

or improvement of turbulence dispersion models is beyond the objectives of this research, it could be interesting to analysis how a more detailed resolution of the turbulent field could allow us to improve the description of droplet dispersion. Thus, exploiting the Eulerian-Lagrangian unsteady solver, a LES simulation of the same case has been performed. The entire duct was modelled with a hexahedral mesh of about 2 million elements. Smagorinsky model was used to reproduce sub-grid scale turbulence effects and no fluctuations were superposed to the mean inlet velocity relying on the flow through the annular inlet duct for the development of turbulent structures. Furthermore, in this case, no turbulent dispersion model was included in the simulation assuming that the particle motion is mainly determined by the resolved scales. Since the main aim of this investigation is to understand the effects of a more detailed description of the flow field in the prediction of particle dispersion, in the following only qualitative results will be presented. Fig. 3.26 shows the velocity field of the LES simulation and the turbulent eddies identified by means of the Q-criterion [121] (a widely used methodology based on the second invariant of the velocity gradient tensor). It is possible to note

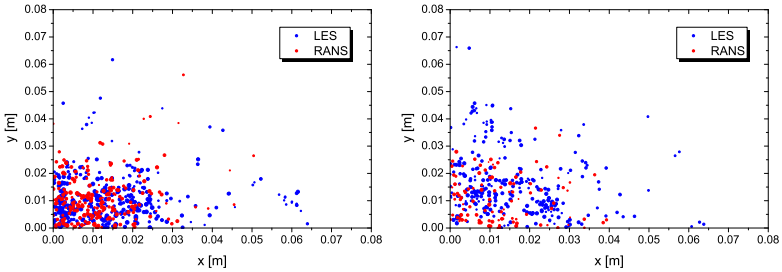

(a) Plane z = 300 mm (b) Plane z = 350 mm

Figure 3.27: Droplet dispersion predicted in RANS and LES simulations (*Test-2*).

that the unsteady velocity field is characterized by a lot of structures that tend to carry particles far away from the duct axis. Fig. 3.26 also shows a comparison between LES and RANS particle tracking where the improvement in particle dispersion prediction obtained using detailed turbulent flow simulations is clearly demonstrated. The same conclusion can be drawn by considering the graphs reported in Fig. 3.27, which represent droplet position at two different plane normal to the spray axis.

Summing up, an application of the solver to an evaporating spray has been presented. Once again the strong coupling between gas-phase and droplet motion is highlighted. A detailed description of the turbulent field allows us to improve the prediction of particle dispersion which is difficult to be caught with standard RANS models, especially when the flow field is characterized by complex turbulent structures. This aspect has to be taken into account when reactive simulations are performed since the evaporated fuel mass fraction field predicted with standard RANS calculations could be far from the real distribution.

3.6.3 TEST-3

In this test case the evaporation of an acetone spray is considered. Fig. 3.28 shows a representation of the experimental configuration used to generate the spray. The system is mounted vertically in a

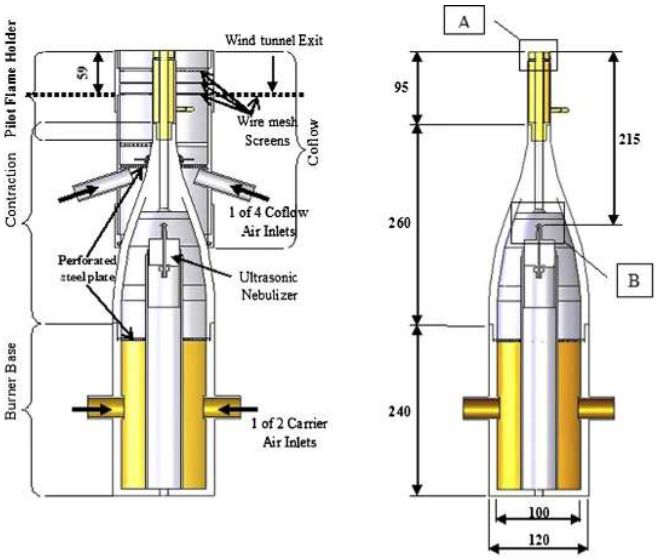

Figure 3.28: Experimental apparatus of *Test-3* (taken from [122]).

wind tunnel that supplies a co-flowing air stream of 4.5 m/s. Spray is generated using an ultrasonic nebulizer: fuel droplets generated on the nebulizer surface are convected downstream at the burner exit plane by a carrier stream of air. The particular geometric configuration allows the formation of a uniform spray profile at the exit plane. A detailed description of the experimental setup and apparatus used for the generation of the experimental data can be found in references [123, 124]. The computational domain considers the region downstream of the exit plane with a computational setup similar to the one used by De et al. [113]. The computational mesh (a structured hexahedral mesh) represents a sector of 90 degrees of the entire domain. Inlet boundary conditions to both gas and disperse phases have been imposed using experimental measurements performed near the exit plane. Particle turbulent dispersion has been accounted for by means of a stochastic model (see Section 3.4.3), spray evaporation has been modelled using the model derived from Borman and John-

Table 3.4: Main characteristics of selected non-reacting acetone spray (SP2) for *Test-3*.

Quantity	**Value**
Bulk jet velocity [m/s]	36
Air mass flow rate [g/min]	225
Liquid fuel injection rate [g/min]	75
Temperature at jet exit plane [$^{\circ}C$]	-5.0
Measured liquid flow at exit [g/min]	33.9
Vapour fuel flow rate at jet exit [g/min]	41.0
Jet Reynolds number	31800

son [92] whereas secondary atomization has been included using the TAB model [102]. Table 3.4 summarizes the most important inlet conditions of the examined case (in the experimental database it is referred to as SP2).

An important quantity to evaluate the capabilities of the code to handle spray evaporation is the liquid fuel mass flux (or equivalently the liquid volume flux) which represents the mass flow rate per unit area of droplet crossing a given section. Fig. 3.29 shows the droplet volume flux at four different planes normal to the burner axis. A good agreement with experiments was obtained at the all locations resulting in a reliable prediction of the evaporation process. Furthermore, it should be noted that in this case the turbulent dispersion predicted by the RANS simulation is able to adequately represent the experimental behaviour.

Furthermore, in Fig. 3.30 a comparison between numerical and experimental SMD is presented. Sauter mean diameter is generally considered the most representative diameter for evaporation and heat transfer processes and, also in this case, a good agreement with experiments was obtained, especially in the region near the burner axis. Far from the axis (higher values of r/D_{jet}), the SMD is slightly underpredicted, however in this region the droplet volume flux is very small and thus these droplets give a negligible contribution to the whole spray.

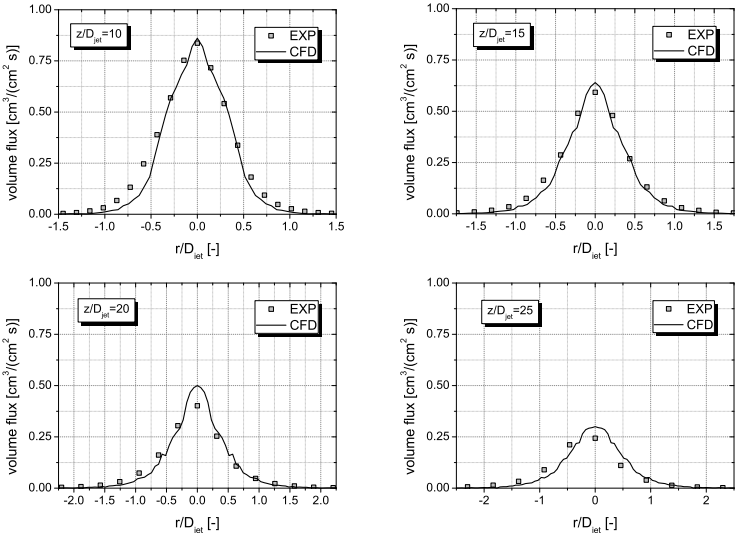

Figure 3.29: Volume flux at different planes normal to the burner axis (*Test-3*).

3.7 Concluding remarks

In order to perform industrial computations of aero-engine combustors, a steady-state solver for reacting sprays based on the Eulerian-Lagrangian approach has been developed in the framework of OpenFOAM. All the aspects related to interactions between gas-phase and droplets have been carefully analysed and up-to-date models for evaporation and secondary breakup have been introduced in the code. It should be noted that proper injection models suitable for gas-turbine applications have also been implemented (these models allow us to efficiently couple injectors with periodic models, see for example the simulations of the test cases used for validation, with completely independent injectors). All the models have also been integrated with the unsteady solver already present in the base version of the code which is useful to simulate the transient behaviour of many phenomena.

Assessment of evaporation and secondary breakup models has

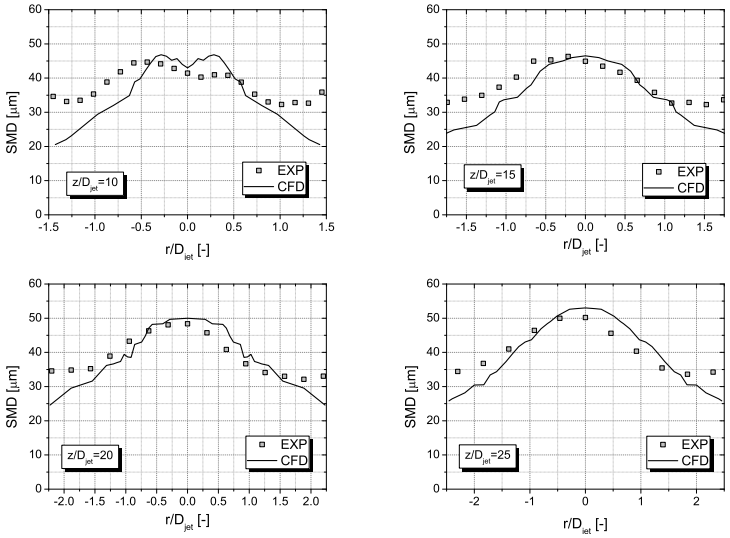

Figure 3.30: SMD at different planes normal to the burner axis (*Test-3*).

been performed together with the validation of the implemented steady-state solver. Test cases representing particle motion in swirled flows and droplet evaporation in a turbulent field have been considered showing a general good agreement of numerical results with both experimental data and results obtained with the commercial code Ansys CFX. Comparisons with experiments also show that in some cases (especially when the flow field is characterized by complex turbulent structures) RANS simulations could lead to an underestimation of turbulent dispersion which could affect the droplet distribution inside the domain resulting in a more coherent spray. Since the main aim of this research is not the development of combustion models, validation in reacting cases has not been considered in this chapter. However, in order to assess the implementation of the EDC combustion model, comparisons between the results obtained with the developed solver and the ones obtained with Ansys CFX will be presented in Chapter 6 where the developed tools are applied to the simulation of a tubular combustor.

The approach presented in this chapter allows the solution of spray dynamics in the dilute region but does not include any model for the description of the liquid film evolution which could have important effects on liquid fuel preparation when a prefilming airblast injection system is considered. Therefore the solver has been further improved through the introduction of a film solver and proper models for liquid film breakup. The integration of the spray solver with the film solver will be described in Chapter 4 whereas in Chapter 5 a model for liquid film primary breakup able to account for the phenomena characterizing liquid film and spray dynamics in the dense region will be presented.

Chapter 4

Multi-coupled solver

In Chapter 3 the basic concepts of spray modelling have been introduced together with the description of a steady-state approach for spray simulation, very useful in industrial computations in order to reduce the computational cost. However in prefilming airblast injectors, commonly used in lean burn aero-engine combustors, a liquid film interacting with both gas-phase and droplets is also present. Thus, in order to perform more realistic simulations of the liquid fuel preparation, it is important to develop a computational method able to consider all the different phases involved in the fuel evolution. In this work, a multi-coupled approach based on the coupling between an Eulerian-Lagrangian spray solver and a thin film solver is proposed. In the following, first of all, possible approaches for liquid film simulation suitable for industrial computations will be presented, then the developed solver will be described with great attention to the interactions among the different phases. Finally, validation of the film solver using test cases representing shear-driven films in configurations close to real prefilming airblast atomizers will be reported.

4.1 Possible approaches for liquid film solution

A liquid film evolving over solid walls and driven by a co-flowing air stream is a particular case of multi-phase flows where both liquid and gas-phase have to be treated as a continuum. A detailed description

of the liquid film evolution requires the solution of the interface between gas-phase and liquid film. However, computational methods able to directly resolve the interface (for example VOF and level-set methods [125]) are usually characterized by a very high computational cost [25, 36], therefore in industrial computations simplified approaches are usually preferred. Basically, two different methods can be found in literature for the simplified solution of a liquid film:

- Bai and Gosman approach [26]: it is based on an Eulerian description of the liquid film under the thin film approximation.
- O'Rourke and Amsden approach [126]: it consists in a Lagrangian tracking of particles representing the wall film.

In the following both approaches will be presented with great attention to the first one which has been used in the current implementation of the multi-coupled solver.

4.1.1 Bai and Gosman approach

The mathematical model for liquid films developed by Bai and Gosman [26] allows the prediction of the dynamical characteristics of wall films also taking into account the contribution of impinging droplets. A similar approach has also been used by Ebner et al. [38] to describe the evolution of a liquid film in configurations representing the most important interactions that could be found in typical airblast injectors. As described in reference [26], the approach is based on the following main assumptions:

- the film is thin enough so that boundary layer approximation can be applied. Under this assumption, the spatial gradients of the dependent variables tangential to the surface are negligible compared to those in the normal direction.
- Under the boundary layer approximation, the local pressure within the film can be taken constant across the film depth. The local pressure is given by the sum of gas-phase pressure, hydrostatic pressure, droplet impact pressure and surface tension contribution.

- Film motion is caused by shear at the interface, body forces, tangential momentum sources provided by imping droplets[1] and spatial variations in the tangential direction of the local pressure.

Boundary layer conservation equations are written for the liquid film and integrated with respect to the cross-film coordinate obtaining evolution equations in terms of depth-averaged quantities with the following general form:

$$\frac{\partial}{\partial t}(\rho_f \phi \delta) + \nabla_S \cdot (\rho_f \delta \phi \mathbf{V}_f) = S_\phi \tag{4.1}$$

where ∇_S is the surface nabla operator, δ is the local film thickness, $\mathbf{V}_f$ is the depth-averaged film velocity, ϕ represents one of the velocity components, or a quantity related to energy or the number 1 in the case of mass conservation equation. Finally S_ϕ is a generic source term accounting for pressure gradients, evaporation, heat transfer, external forces and contributions due to the impinging droplets. Thus, for example, integration of the continuity equation along the cross-film coordinate leads to the following expression:

$$\frac{\partial}{\partial t}(\rho_f \delta) + \nabla_S \cdot (\rho_f \delta \mathbf{V}_f) = \dot{m}_f \tag{4.2}$$

where $\dot{m}_f$ is the mass source per unit film area due to droplet adsorption, film separation, film stripping and phase change.

$$\dot{m}_f = \dot{m}_{imp} + \dot{m}_{strip} + \dot{m}_{ev} \tag{4.3}$$

Specific models are introduced in the formulation to compute this term (note that the terms representing evaporation $\dot{m}_{ev}$ and droplet stripping or separation $\dot{m}_{strip}$ have negative values since mass is removed from the liquid film). Droplet adsorption is accounted for by impingement models (see Section 4.4), an example of separation model is given by the primary breakup model introduced in this work

[1]It is assumed that the tangential momentum lost by the incident droplets provide a source of tangential momentum for the liquid film.

and described in Chapter 5 whereas film evaporation is computed through the following equation [26]:

$$\dot{m}_{ev} = \frac{Sh\rho_g \mathscr{D}}{L_f} \frac{Y_{F,\infty} - Y_{F,S}}{1 - Y_{F,S}} \tag{4.4}$$

where L_f is a longitudinal length scale.

As far as the momentum conservation is concerned, the following equation can be written:

$$\frac{\partial}{\partial t}(\rho_f \delta \mathbf{V}_f) + \nabla_S \cdot (\rho_f \delta \mathbf{V}_f \mathbf{V}_f) = -\delta \nabla_S p_f + \rho_f \delta \mathbf{g}_t + \boldsymbol{\tau}_{fs} - \boldsymbol{\tau}_w + \mathbf{S} \tag{4.5}$$

where $\mathbf{S}$ is an additional source term which accounts for evaporation, droplet impingement or film separation and p_f is the sum of gas pressure, capillary pressure, hydrostatic pressure ($\rho_f \delta g_n$) and pressure contribution due to impinging droplets:

$$p_f = p_g - \sigma \nabla_S \cdot (\nabla_S \delta) - \rho_f \delta \mathbf{g} \cdot \mathbf{n} + p_{imp} \tag{4.6}$$

Finally, the energy conservation equation can be written as:

$$\frac{\partial}{\partial t}(\rho_f \delta h_{s,f}) + \nabla_S \cdot (\rho_f \delta h_{s,f} \mathbf{V}_f) = \dot{q}_{ht} + \dot{q}_{\dot{m}_f} \tag{4.7}$$

where the different contributions due to mass exchange, $\dot{q}_{\dot{m}_f}$, and heat transfer with both gas-phase and solid walls, $\dot{q}_{ht}$, have been highlighted. These equations will be considered again in Section 4.2, where more information about the solution procedure and the boundary conditions will be given.

4.1.2 O'Rourke and Amsden approach

In the approach of O'Rourke and Amsden [126], the liquid film is described by means of computational particles which are tracked along the surface. The equations used for particle tracking are based on the thin film approximation with the additional assumptions of laminar behaviour of the liquid film and negligible effect of inertial and

gravitational forces on the film dynamics. Furthermore, it is assumed that gas-phase velocities above the film are much larger than the film velocity so that the film is seen by the gas-phase as a solid wall. Compared to Eulerian approaches, this method allows us to avoid numerical diffusion due to spatial discretization and it is easier to be integrated with a particle spray model (for example if a particle detaches from the surface it is directly assigned to the spray Lagrangian solver). However the tracking along a surface requires particular attention, especially along curved surfaces, and this method is quite difficult to be integrated in a steady-state approach.

4.2 Description of the developed solver

The Eulerian-Lagrangian solver for reacting sprays presented in Chapter 3 has been integrated with a film solver based on the Bai and Gosman approach [26] leading to the development of a multi-coupled solver able to take into account all the interactions between liquid film, droplets and gas-phase [127]. Thus, in the developed approach, both gas-phase and liquid film are described in the Eulerian framework whereas the fuel spray computation is based on the Lagrangian method.

The multi-coupled solver has been developed in both steady-state and unsteady approaches. Interactions between gas flow, spray and liquid film, are taken into account by means of specific source terms in the conservation equations describing their dynamics. In the solution algorithm we can distinguish an outer iteration loop, where the different phases are solved following a segregated approach, and an *inner loop* for each solver. In the current implementation of the *outer loop*, the liquid film is solved first, then the spray evolution is computed and finally the gas-phase with source terms derived from both Lagrangian solver and liquid film solver is resolved. As regards inner loops of gas-phase and droplet solvers, the solution procedure is very similar to the one presented in Section 3.2 excepting the presence of source terms in gas-phase conservation equations due to the presence of liquid film and the need of specific models to handle interactions between liquid film and droplets. In the following, solution strategies for the liquid film and the interactions between the film solver and

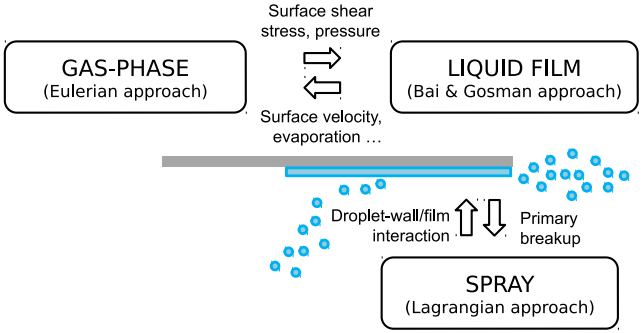

Figure 4.1: Main interactions between the film solver and the other solvers.

the Eulerian-Lagrangian spray solver will be described in more detail.

4.2.1 Liquid film solution

The film solver implementation exploits the thin film model already present in the base version of OpenFOAM. In this work, the original model has been further improved through the development of specific strategies for steady-state solution and through the introduction of a new model for primary breakup of liquid films (see Chapter 5). Furthermore, some additional improvements have been made in the description of the interaction with the gas-phase where the surface shear stresses are directly retrieved from the gas-phase solution and models able to consider the liquid film roughness have been introduced in the code.

The liquid film is solved in a single layer mesh obtained by extruding the boundary mesh of the gas-phase domain where a film is expected to be present. Fig. 4.1 shows a schematic representation of the main interactions between the film solver and the other solvers in a typical airblast injector configuration. The liquid film is solved over the pre-filming surface and as the liquid film reaches the atomizing edge, droplets are injected into the Eulerian-Lagrangian solver using a proper primary breakup model. As in all shear-driven films, the fluid motion is mainly determined by the surface shear stress exerted by the gas phase flow with the additional contribution of pressure gradi-

ents (as stated above, the pressure inside the film is equal to the sum of gas flow pressure, hydrostatic pressure, droplet impact pressure and pressure induced by surface tension), body forces and momentum sources provided by impinging droplets. Thus, the gas-phase flow directly influences the film dynamics through the contribution of pressure gradients and surface shear stresses in the film momentum equation. Furthermore, heat transfer between film and gas flow is also accounted for by means of a specific energy equation. On the other hand, liquid film determines source terms in the gas-phase mass and energy conservation equations through the evaporation and heat transfer processes whereas the effect of the liquid film in the gas-phase momentum equation is imposed through boundary conditions (the gas-phase velocity at the interface must be equal to the film surface velocity). As regards interactions with the spray Lagrangian solver, specific models for stripping, breakup or, more in general, film separation, provide parcels to be injected and thus added to the spray population. Wall/film-droplet interaction is accounted for by means of a particular impingement model derived from the work of Bai et al. [68] (see Section 4.4).

4.2.1.1 Steady-state approach

In order to perform fully steady simulations, a steady-state version of the film solver has been coupled with the steady-state Eulerian-Lagrangian solver described in Section 3.2.

As described in Section 4.1.1, in the Bai and Gosman approach, conservation equations for the liquid film are expressed in terms of depth-averaged quantities. Under the steady-state assumption, equations presented in Section 4.1.1 can be rearranged leading to the following expressions for mass, momentum and energy conservation laws:

$$\nabla_S \cdot (\rho_f \delta \mathbf{V}_f) = \dot{m}_f \tag{4.8}$$

$$\nabla_S \cdot (\rho_f \delta \mathbf{V}_f \mathbf{V}_f) = \mathbf{S}_{p_g} + \mathbf{S}_\tau + \mathbf{S}_g + \mathbf{S} \tag{4.9}$$

$$\nabla_S \cdot (\rho_f \delta h_{s,f} \mathbf{V}_f) = \dot{q}_{ht} + \dot{q}_{\dot{m}_f} \tag{4.10}$$

where in the momentum equation the contributions related to gas-phase pressure gradients $\mathbf{S}_{p_g}$, gravity acceleration $\mathbf{S}_g$ and surface shear stresses $\mathbf{S}_\tau$ have been highlighted and in the energy equation the terms related to the mass added to or removed from the liquid film have been indicated with symbol $\dot{q}_{\dot{m}_f}$. In the solution algorithm (liquid film inner loop), first the momentum equation is solved followed by the energy equation. Finally a thickness-corrector equation derived by combining momentum and mass conservation equations is introduced. In order to enhance convergence rates, the liquid film loop can be repeated many times inside the same outer loop.

4.2.1.2 Unsteady approach

Evolutive terms are introduced in the Eulerian equations describing liquid film evolution leading to the conservation equations presented in Section 4.1.1. In the fully unsteady approach, the unsteady solution of the liquid film is coupled with the unsteady Eulerian-Lagrangian spray solver (see Section 3.3). In this case, each phase is separately advanced in time and once the integration along the assigned time step is completed, source terms are updated and returned to the other phases. As previously stated, in the current implementation liquid film is solved first, then Lagrangian tracking is performed and finally gas-phase evolution is computed with source terms coming from both film a disperse phase solutions. As regards the liquid film solution, the algorithm is similar to the one used for steady state computations excepting the presence of evolutive terms in the conservation equations and the solution of the continuity equation before momentum.

4.2.2 Limitations

Before presenting the assessment and validation of the film solver in configurations close to prefilming airblast injectors, it is important to note that the approach used for liquid film solution presents some limitations mainly due to the solution strategy and the assumptions used in the derivation of conservation equations. The following as-

pects have to be considered with great attention when the solver is applied to real configurations:

- Conservation equations are resolved in terms of depth-averaged quantities thus the profile of a given quantity along the film thickness is not a result of the simulation. If gradients in the direction normal to the film surface are required, some assumptions about the shape of the profile should be made. This is, for example, the case of the velocity gradient at the wall boundary which is used for the computation of wall shear stresses. Cubic profile [26], linear profile [87] and boundary layer approximations are common choices.

- The interface is not resolved. Thus, interfacial phenomena, such as surface instabilities, are not directly accounted for in the liquid film solution and some models are required to introduce their effect in the simulation. This is, for example, the case of additional shear stress due to the presence of surface roughness (see Section 4.3.1) or the primary breakup and stripping phenomena. The simulation of the gas-film interface requires other simulation approaches such as VOF and level-set methods. However, these methods require a very high mesh resolution and are too CPU-time consuming to be applied in realistic configurations and to be used in standard industrial design process.

- The film is considered thin leading to the application of boundary layer approximation. However, the liquid film evolution in real atomizers is very complex and especially near the injection holes the film develops with three-dimensional structures that can be captured only using methods able to resolve the interface between liquid film and gas-phase. However, as stated above, these methods are characterized by a very high computational cost to be used in industrial computations.

- The liquid film mesh is built starting from boundary patches defined in the gas-phase domain. Therefore the liquid film can exist only over boundary walls and it is not possible to predict liquid film entrainment into the gas phase. For example,

in the case of airblast atomizers, the liquid film can be described only over the prefilming surface and the film evolution downstream of the atomizing edge cannot be predicted with this model. Film behaviour in the space between the atomizing edge and the actual breakup location (usually identified with a *breakup length*) should be accounted for through a proper primary breakup model for liquid films.

All these aspects should be kept in mind since they have important effects in the derivation of specific models to describe interactions between gas-phase and liquid film as it will be more clear in the remainder of this dissertation.

4.3 Validation of the film solver

The solver capabilities to reproduce shear-driven films were assessed by considering two different test cases [7] which allow us to simulate the main interactions between liquid film and gas-phase that could be found in typical airblast atomizers. Typical injector configurations are characterized by an acceleration of the surrounding air, thus, in the first test case, a liquid film undergoing a pressure gradient is considered. Additionally, airblast injectors used in aero-engines usually have a conical shape and thus the film load Λ_f (volume flow rate per unit width) varies as a consequence of a different radius. The combined effect of pressure gradient and film load gradient is considered in the second test case. For the geometrical characteristics of these test cases the reader is addressed to reference [7]. Finally, a first application of the multi-coupled solver to the prediction of liquid film evolution over the prefilming surface of a PERM injection system is also presented.

4.3.1 TEST-1

Fig. 4.2 shows the test case geometry and the hexahedral computational mesh used in the numerical simulation (the single layer mesh for the film solver is reported in red). The liquid film (a fluid with physical properties similar to those of kerosene at 80 °C [7]) develops on the bottom surface whereas the air flow is accelerated by

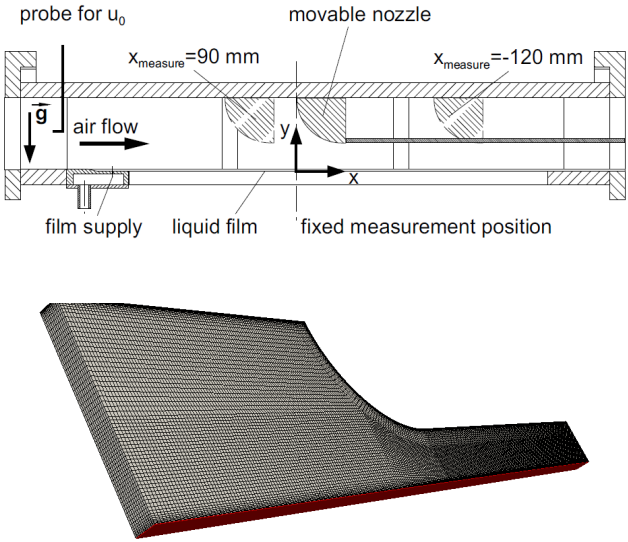

Figure 4.2: Schematic representation of the test case geometry (taken from [7]) and computational mesh (*Test-1*).

means of the nozzle opposite the film propagation surface. Different measurements were performed varying the inlet air velocity and the film loading. Simulations have been performed using a fully steady approach (both gas-phase and liquid film solved with steady-state acceleration techniques). As regards boundary conditions, a uniform velocity was imposed at the inlet boundary, atmospheric static pressure was assigned at the outlet whereas a cyclic condition was assigned to the lateral faces. Solid walls were modelled with a no-slip condition whereas the k-ω SST [118] turbulence model was used to reproduce the effects of turbulence on the mean flow. As far as the interface between liquid film and gas-phase in concerned, more details about the strategy used to correctly represent the shear stress exerted by the gas flow are given in the following.

Because of the interaction with the gas flow and related unstable phenomena (see for example Kelvin-Helmholtz and Rayleigh-Taylor instability mechanisms [128, 129]), waves are generated on the liquid

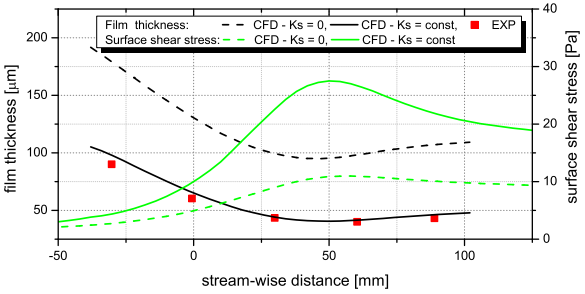

Figure 4.3: Comparison between film thickness and surface shear stress predicted with and without film roughness modelling (*Test-1*).

film surface which, as a consequence, is seen by the gas flow as a rough wall increasing the shear stress at the interface. Thus, in order to properly predict the film velocity and the film thickness, it could be important to introduce the effects of this additional roughness in the computation of surface shear stresses. Since in the proposed approach the interface between liquid film and gas-phase is not resolved, the effects of film roughness have to be introduced in the simulation through a proper model. If a wall-function approach is used, the effect of film waves can be represented by means of an equivalent sand-grain roughness K_S to be used in the computation of the turbulent dynamic viscosity. The importance of considering the film roughness is demonstrated in Fig. 4.3 where two different simulations of the same case ($U_{g,in} = 20$ m/s and $\Lambda_f = 0.2$ cm^2/s), with and without the introduction of the equivalent sand-grain roughness, are compared with each other and with experimental data of reference [38]. A proper prediction of the film thickness requires the introduction of a model able to take into account the enhancement of surface shear stresses due to wave formation on the liquid film surface.

In the previous simulation a constant value of K_S obtained with a calibration procedure was used. As also shown in Fig. 4.4 where comparisons with experimental data at different film loads are presented, this strategy leads to an overprediction of film thickness in the nozzle upstream region, especially at high film loads. The main cause of this behaviour can be ascribed to the constant value assigned

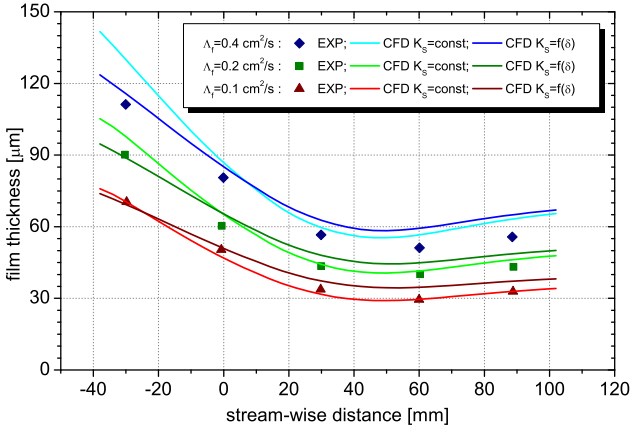

Figure 4.4: Comparison between different modelling strategies for K_S ($U_{g,in} = 20$ m/s).

to K_S: the dimension of the structures generated over the film surface may depend on film thickness and a higher roughness is expected to be present in the regions with a higher film thickness. In order to include this effect in the model, following the work by Ebner et al. [38], an equivalent sand-grain roughness coefficient based on film thickness has been introduced:

$$K_S = 2\delta\Psi \tag{4.11}$$

where Ψ is a function that depends on liquid film properties (see reference [38] for further details). As shown in Fig. 4.4, this modeling approach allows us to improve film thickness predictions at high film loads. Film thickness in the nozzle region is slightly overpredicted, however this approach has the great advantage of not requiring a user-definition of K_S since it is directly derived from the liquid film solution.

Comparisons between steady-state and unsteady approaches were also performed obtaining almost identical results [9].

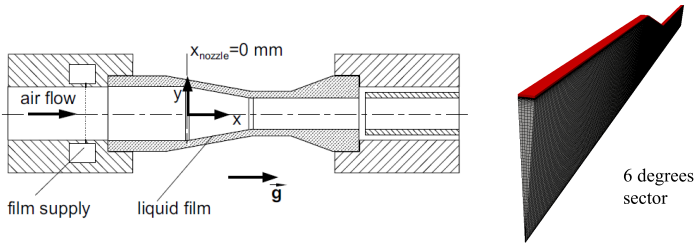

Figure 4.5: Schematic representation of the test case geometry (taken from [7]) and computational mesh (*Test-2*).

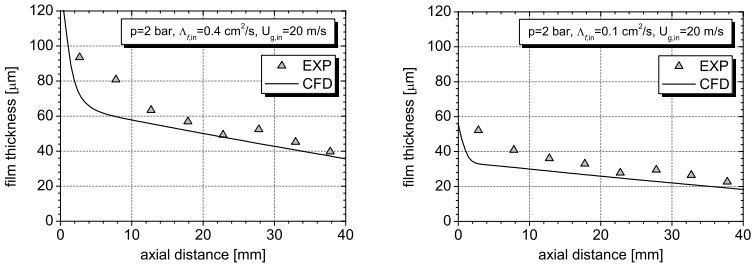

Figure 4.6: Comparison between numerical results and experimental measurements [130] (*Test-2*).

4.3.2 TEST-2

A representation of the second test case is reported in Fig. 4.5 together with the computational domain representing a 6 degree sector of the experimental rig (the film domain is represented by the red region). A liquid film with the same properties of the fluid used in the previous case in supplied around the circumference of the inner duct. Several measurements were performed varying the inlet air velocity and pressure and the film load. A computational setup similar to the one used in the previous case was applied and also in this case the steady-state approach was used for the numerical simulation.

In Fig. 4.6 comparisons between numerical results and experimental measurements (taken from reference [130]) are reported for two selected conditions. A good agreement with experiments was found

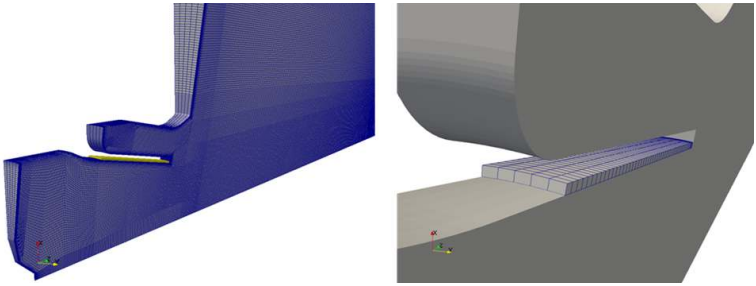

Figure 4.7: Computational mesh.

proving the capability of the solver to correctly represent the interactions between liquid film and gas-phase usually found in typical airblast injector configurations where a pressure gradient and a film load gradient are usually present at the same time.

4.3.3 Application to a PERM injection system

Before examining in depth the aspects related to the modelling of droplet-film interactions and liquid film primary breakup, a first application of the film solver to the study of the film evolution over the prefilming surface of a PERM injection system is presented. In the investigated case, the injector was arranged in a tubular combustor configuration. A high pressure condition was considered so that parcels injected through the pilot injector rapidly evaporate near the injection location and do not impinge the liquid film (see also the application to a tubular combustor presented in Chapter 6). Therefore, the most important modelling aspect to be considered in the computation of the liquid film evolution is the interaction between liquid film and gas-phase. As shown is Fig. 4.7, where the computational mesh near the injection region is reported, the computational domain consists in a sector of 9 degrees of the entire combustor. In Fig. 4.7, the single layer mesh used by the film solver is also reported. Swirler blades were not included in the computational domain and air inlet boundaries were placed at blade exit plane. Swirled flows were reproduced by assigning to air flows a mass flow rate and the

Table 4.1: Liquid film inlet conditions.

Case	V_n/V_{ref} [-]	V_t/V_{ref} [-]	δ_n/δ_{ref} [-]	$\dot{m}/\dot{m}_{nom}$ [-]
1	1.0	1.53	200	0.5
2	1.0	1.53	400	1.0
3	2.0	3.06	200	1.0
4	2.0	4.59	200	1.0

direction of velocity vectors. The aero boundary conditions were obtained by sampling and averaging in the azimuthal direction the results obtained in a separate simulation of the injector, basically a 3D numerical simulation of the injection system. A static pressure was imposed at the exit of the combustor whereas cyclic boundaries were used for the lateral sides. No-slip and adiabatic conditions were assigned to all the solid surfaces. Boundary conditions for the liquid film include a uniform thickness, temperature and velocity at the film inlet boundary and cyclic conditions on lateral edges.

An important issue in the simulation of such system regards the set-up of boundary conditions to be assigned to the liquid film inlet boundaries. Uniform inlet velocity and film thickness are common choices, however, in the real configuration the liquid fuel is supplied through an array of holes and the location at which the film can actually be considered uniform is not known. In this investigation the film inlet boundary was placed at the same location of the injection holes and a sensitivity analysis to the inlet boundary conditions was performed in order to determine the effects of such conditions on the quantities at the outlet boundary which mainly determine the characteristics of detached droplets as it will be described in Chapter 5.

Four different cases, differing by inlet normal and tangential velocity components, initial thickness and mass flow rate (see Table 4.1), were evaluated. Table 4.2 summarizes the liquid film characteristics at the outlet boundary for each case whereas Fig. 4.8 shows film thickness and the axial velocity field over the lip. Film inlet conditions have a small influence on the velocity component normal to the outlet boundary as well as on the film thickness which mainly depends on the film mass flow rate. On the contrary, different inlet tangential

Table 4.2: Liquid film characteristics at the outlet boundary.

Case	V_n/V_{ref} [-]	V_t/V_{ref} [-]	δ/δ_{ref} [-]
1	7.83	1.41	30.3
2	9.48	2.32	50.3
3	9.48	3.18	50.3
4	9.42	4.16	50.4

velocity components determine a different final tangential velocity which could determine different swirl components to the parcels injected through the liquid film primary breakup model. Furthermore, it should be noted how a different film load mainly affects the film thickness whereas the variations of the velocity component normal to the outlet boundary are more restrained.

In the previous simulations liquid film evaporation and heat transfer with both solid walls and gas-phase have been neglected. However, these phenomena could have important effects on both liquid film evolution and fuel preparation. The temperature of the injected liquid is usually much smaller than the gas-phase temperature, therefore an increase in temperature is expected during the film evolution along the prefilming surface. A proper computation of the temperature increase is very important since the liquid film temperature at the atomizing edge directly defines the temperature of droplets injected through the primary atomization model which could have a strong impact on the droplet dynamics after injection (for example, a higher initial temperature reduces the droplet heat-up period making the evaporation process much faster) and thus on fuel distribution inside the combustion chamber. Although the developed model is in principle able to handle heat transfer through the solution of the energy equation, the computation of the actual temperature of the liquid film requires the definition of proper boundary conditions at the interface with both solid walls and gas-phase, which especially on the wall side could be difficult to be evaluated. In the actual implementation, heat transfer from the gas side can be directly retrieved from the gas-phase solution by imposing a gas surface temperature equal to the film temperature. On the wall side, a user-defined heat

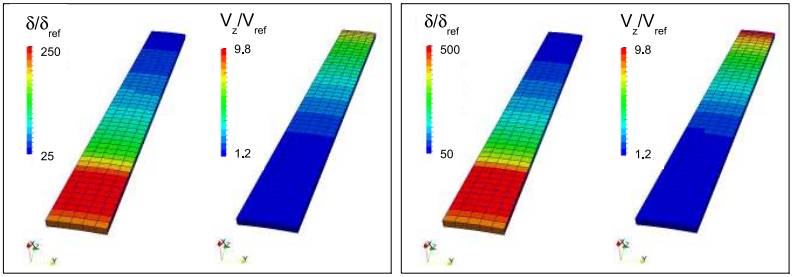

(a) Case 1. (b) Case 2.

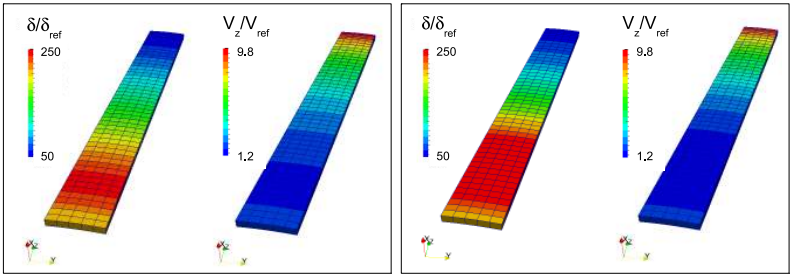

(c) Case 3. (d) Case 4.

Figure 4.8: Analysis of liquid film evolution, comparison between different cases.

transfer coefficient could be used, however the main uncertainty is related to the wall temperature which is not known and could also be affected by the radiative heat transfer. During the evolution along the prefilmer surface, the liquid film is also subjected to evaporation. Part of the fuel is released to the gas-phase before reaching the atomizing edge directly influencing the fuel distribution inside the combustor. Furthermore, the evaporation process also occults some of the energy transferred to the liquid film determining a reduction of the film temperature. In this work the evaporation process has been accounted for using the formulation presented in Section 4.1.1 together with proper source terms in the conservation equations describing film and gas-phase dynamics.

As a first attempt at the evaluation of film temperature, the previous simulations were performed again by imposing evaporation and heat transfer on the gas-phase interface and an adiabatic condition on the wall side. Results at the atomizing edge show an increase in temperature of more than 50 K with a slight reduction of film thickness and an increase of the film velocity component normal to the outlet boundary ($\delta/\delta_{ref} \approx 44.0$ and $V_n/V_{ref} \approx 11$ for Case 2, 3 and 4) whereas the evaporated mass predicted in these simulations appears to be negligible compared to the injected mass. It is important to note that the operating condition considered in these simulations is representative of full load operations. Partial load operating conditions are usually characterized by lower values of gas temperature, thus a smaller increase of film temperature can be expected in such conditions.

4.4 Droplet-film interaction

Droplets evolving inside the combustion chamber could interact with both solid walls and liquid film. Thus, for a more reliable prediction of droplet dynamics, it is important to consider proper impact models. In this work the model developed by Bai and Gosman [68], and further improved by the same authors [131], was used exploiting the implementation present in the base version of OpenFOAM with some modifications in order to achieve a correct integration with the steady-state solver. This model was formulated using a combination of simple theoretical analysis and experimental data from a wide range of sources. Furthermore it considers both dry and wetted wall conditions as well as different interaction regimes with a refined methodology for the computation of droplet characteristics after impingement in comparison to a previous model of the same authors [21].

The model neglects the effects of neighbouring impinging droplets and gas boundary layer on the impinging dynamics and considers only interaction regimes at sub-boiling temperature. As observed in [21], the last assumption is usually verified in internal engine applications. In aero-engines, stationary operation could lead to very high wall temperatures. However, sub-boiling temperatures can be considered

Table 4.3: Transitional Weber numbers at sub-boiling temperatures [68].

Wall status	**Regime transition state**	**Critical Weber number**
Dry	Adhesion (Stick/Spread) → Splash	$We_{I,c} \approx 2630La^{-0.183}$
Wetted	Stick → Rebound	$We_{I,c} \approx 2$
	Rebound → Spread	$We_{I,c} \approx 20$
	Spread → Splash	$We_{I,c} \approx 1320La^{-0.183}$

a good assumption especially at partial load operations and in the following sub-boiling conditions will be assumed addressing to future research the implementation of a more general model together with a more detailed investigation on the temperatures reached by both solid walls and liquid film. A schematic representation of the different regimes considered in the model is given in Fig. 2.6. The transition from one regime to another is based on the impact Weber number. The values of critical impact Weber numbers for transition between different regimes are reported in Table 4.3. For a comprehensive description of the methods used to compute post-impingement characteristics, the reader is addressed to references [68, 21]. Here, it is important to note that in the case of stick and spread regimes, droplet are removed from the Lagrangian population and source terms are given to the film solver. In particular the mass of the impinging droplet is used to compute the mass flow rate per unit area $\dot{m}_{imp}$ whereas the momentum component normal to the liquid film contributes to the impinging pressure p_{imp} and the momentum component tangential to the liquid film (per unit area) acts directly as a source term $\mathbf{S}$ in the film momentum equation. In the rebound regime the parcel is reflected by the wall/film and continues to evolve in the Lagrangian phase. During the impact some energy could be lost (for example in the impact of a droplet on a liquid film some energy is dissipated in the process that lead to the crow formation). In the current implementation, velocity after droplet impact is computed through a restitution coefficient based on relations developed for a solid parti-

cle bouncing on a solid wall [132, 21]. Finally, in the splash regime the incoming droplet disintegrate into smaller droplets. Thus, the parcel is returned to the Lagrangian solver with a modified diameter and velocity (there is also the possibility of splitting the impinging particle into more parcels). An important parameter for the description of the splash regime is the ratio m_s/m_I between the mass of the secondary droplets generated after the impact and the mass of the incident droplet:

$$\frac{m_s}{m_I} = \begin{cases} 0.2 + 0.6a & \text{for dry wall} \\ \\ 0.2 + 0.9a & \text{for wetted wall} \end{cases} \tag{4.12}$$

a is a random number distributed uniformly in the interval $0 < a < 1$. It should be noted that for a dry wall the mass ratio is always less than one, meaning that some mass is also added to the wall boundary leading to the formation of a liquid film (from a modelling point this mass is passed to the film solver with the same methods used in the stick and spread regime). On the contrary, for a wetted wall the ratio m_s/m_I could also be greater than 1 in order to reproduce the entrainment of liquid from the film which has been observed in experiments during droplet splashing. More details for the computation of droplet characteristics after the impact can be found in references [68, 21].

4.5 Concluding remarks

In this chapter, the integration of the Eulerian-Lagrangian spray solver described in Chapter 3 with a film solver based on the Bai and Gosman [26] approach has been presented. Great attention was devoted to the description of interactions between liquid film, droplets and gas-phase. The capabilities of liquid film solver to handle shear driven films in prefilming airblast configurations were assessed and validated by simulating literature test-cases able to reproduce the most important interactions and features of typical prefilming airblast injectors. Furthermore, a first application of the multi-coupled solver to the prediction of film evolution in a PERM injection system was also presented.

The liquid film solver exploited in this work allows us to include in the simulation several important aspects for the description of liquid fuel preparation in advanced airblast injection systems with a relatively small computational cost. The most important improvements in comparisons with typical approaches which neglect the presence of the liquid film can be summarized as follows:

- interaction between droplets and liquid film is included in the simulation and thus it is possible to implicitly consider the mass addition to the film due to droplet adsorption. This aspect is very important for the PERM injection system because in some operating conditions droplets injected through the pressure atomizer reach the prefilming surface enhancing the main injection mass flow rate.

- Interactions between the liquid film and the gas-phase are accounted for. Therefore it is possible to estimate the liquid mass evaporated from the liquid film and heat transfer between the two phases. More detailed investigations should be performed in the future in order to reduce the uncertainties on heat transfer boundary conditions and therefore determine the actual temperature increase due to heat transfer which could have important effects on both atomization and the subsequent droplet evolution (evaporation and secondary breakup).

- The introduction of a liquid film primary breakup model (see Chapter 5) allows us to directly include in the simulation droplets generated by the liquid film atomization.

These aspects will be deeply analysed in Chapter 6 where the application of the present solver to a PERM injection system in a tubular combustor configuration is presented.

Chapter 5

Primary breakup model for liquid films

In this research lean burn combustors equipped with advanced prefilming airblast injectors have been considered. In this type of injectors a liquid film develops along a prefilming surface and, as the liquid film reaches the atomizing edge, interactions with air streams lead to the disintegration of the film and the generation of fine droplets. In Chapter 4 an approach for the coupled solution of liquid film, gas-phase and spray evolution suitable for industrial calculations has been presented. However, no specific models for the primary breakup of the liquid film were introduced. In order to perform fully multi-coupled simulations, a proper model able to predict the droplet population generated by the film breakup (to be injected in the Lagrangian solver) is necessary.

This chapter is devoted to the presentation of the primary breakup model devised in this research. Before describing the developed model, the primary breakup mechanism observed in recent experiments [133, 128] is introduced. Some of the characteristics of the model proposed in this work are based on these experimental observations. Furthermore, some considerations about the stripping phenomenon which could be responsible for atomization before the film reaches the atomizing edge are also given. Finally, an assessment of the developed breakup model against measurements performed on a PERM injection system at atmospheric conditions using water is presented.

Table 5.1: Operating conditions investigated in experiments.

Quantity	**Gepperth et al.** [73]	**Inamura et al.** [128]
U_g [m/s]	20.0 - 70.0	17.0 - 76.5
p_g [bar]	1.01	1.01
T_g [K]	298	298
Λ_f [cm^2/s]	0.125 - 0.75	0.8 - 3.2
h [mm]	1.0, 2.5	$\approx$0.16
μ_L [kg/(m s)]	0.812×10^{-3} - 53.3×10^{-3}	water
σ [kg/s^2]	0.0255 - 0.0466	water

5.1 Breakup mechanism

In prefilming airblast atomizers the fuel is spread out into a liquid film which is driven along a surface by a co-flowing air. When the atomizing edge is reached, a second air flow interacts with the film leaving the edge and fine atomization is produced in a process that is often referred to as primary breakup. In the following, the air stream which drives the liquid film along the prefilming surface will be referred to as *primary flow* whereas the second air stream which interacts with the liquid film at the atomizing edge will be referred to as *secondary flow*. The quality of the atomization mainly depends on air velocity and, in general, on both air and liquid properties, in particular surface tension and liquid dynamic viscosity. Before introducing the numerical approach used to model the primary breakup of liquid films, it is important to give a brief description of the typical breakup mechanism encountered in prefilming airblast systems. The description is based on recent experimental investigations performed by Gepperth et al. [133] and Inamura et al. [128], where basically the same mechanism was observed in a wide range of operating conditions. Experiments were performed on planar configurations, similar to the one reported in Fig. 5.1. Table 5.1 summarizes the conditions investigated in these experiments: all the investigations were carried out at atmospheric conditions with a gas-flow velocity up to about 70 m/s.

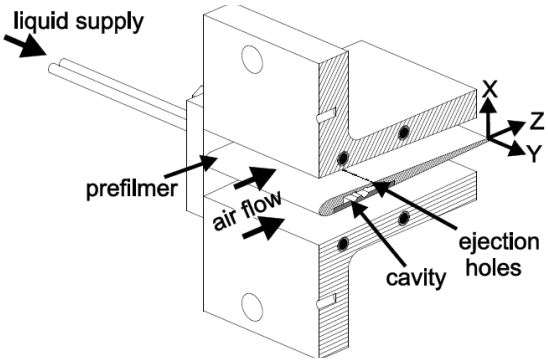

Figure 5.1: Planar configuration of prefilming airblast systems investigated in experiments (taken from [133]).

As reported in [73] and as shown in Fig. 5.2 (taken from [73]), the breakup mechanism observed in prefilming airblast systems can be described through the following steps:

- first, liquid film accumulation at the atomizing edge leads to the formation of a liquid reservoir which is continuously fed by the film flow.
- Then, "bubble" like ligaments are formed out of this reservoir.
- The "bubble" grows in size and eventually is disintegrated. Small droplets are generated by the rupture of this "bubble" with a mechanism similar to the bag breakup of droplets.
- The rim of the "bubble" remains attached to the reservoir and later disintegrates into threads and then into larger droplets.

The process is characterized by a detachment frequency which increases with the air flow velocity. As a consequence of liquid film accumulation, Gepperth et al. [73] observed that the breakup process is completely decoupled from the film flow identifying the atomizing edge thickness as the most important length scale parameter for the determination of the mean drop size. Different considerations were made by Inamura et al. [128] who used a planar atomizer with a

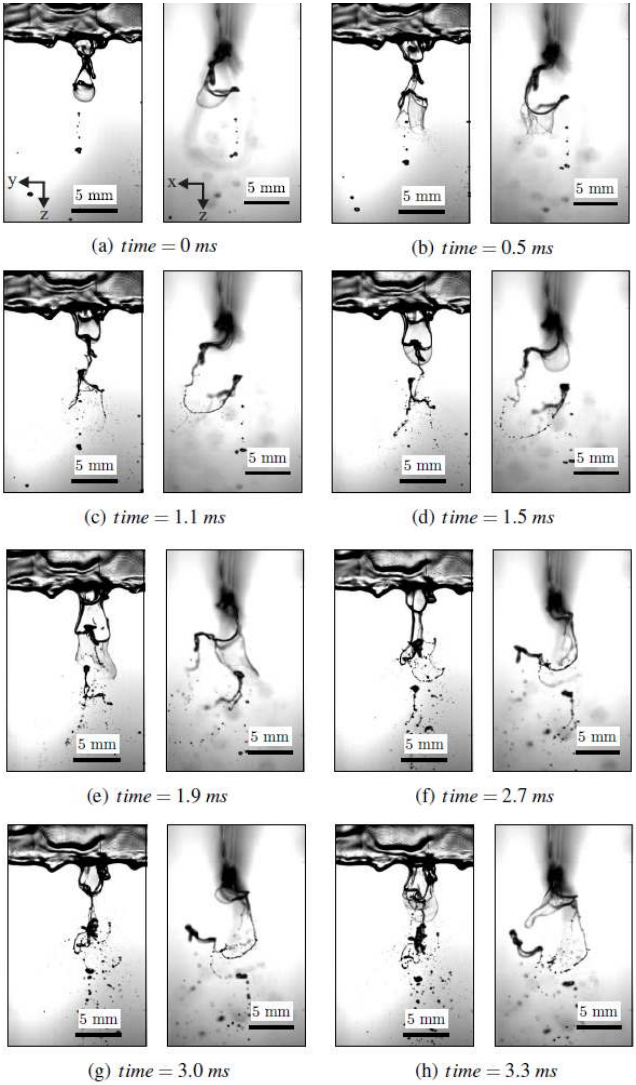

Figure 5.2: High speed sequence of film disintegration (taken from [73], $U_g = 20$ m/s, $\Lambda_f = 25$ mm^2/s, $h = 1.0$ mm).

very thin atomizing edge. In this case they observed a correlation among drop diameter, film thickness and instability phenomena on the prefilming surface. Although Gepperth et al. and Inamura et al. observed a very similar atomization mechanism, the different considerations about the most important parameter affecting primary atomization made by these authors clearly identify the need of more detailed investigations on the physics of primary breakup and the role of film height and atomizing edge thickness on the disintegration process.

It should be noted that in gas turbine applications the air velocity could be greater than the maximum value investigated in these experiments. For example in the PERM injection system investigated in this research, mean "free stream" velocities along the prefilming surface could be greater than 100 m/s, especially at full-load conditions (see the application presented in Chapter 6). As described in Section 2.2.1, higher relative velocities usually lead to smaller droplets moving the atomization process close to the atomizing edge. However, considering the trend observed in experiments [128], a breakup mechanism similar to the one described here could also be expected in these cases even if the role of atomizing edge curvature, air swirled flows and high pressure and temperature has to be deeply investigated and analysed. Furthermore, it should be considered that in real applications the two air streams that interact with the liquid film are usually characterized by different velocities and swirling rotations. This aspect is not considered in the experimental investigations described here, however it could have a strong impact on the atomization process and on the distribution of droplets between the two flows.

5.2 Primary breakup model

As observed in Section 4.2.2, the approach used for liquid film solution is not able to solve the interface between the liquid film and the gas-phase, thus the complex physical phenomena regulating the primary breakup of the liquid film cannot be predicted in the simulation and the droplets generated after breakup have to be introduced

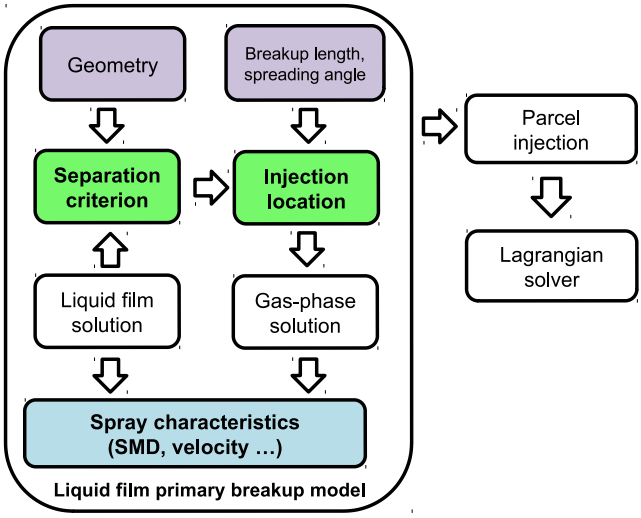

Figure 5.3: Schematic of the primary breakup model.

with a proper model[1]. The main aim of the primary breakup model is to give the characteristics of droplet population to be injected in the simulation and tracked through the Lagrangian solver. Therefore, to some extent, the primary breakup model can be considered as a particular kind of particle injector aimed at reproducing the basic characteristics of liquid film breakup. Since the physics regulating the breakup process is still not completely understood, the developed model is mainly based on a phenomenological approach. Fig. 5.3 shows a schematic representation of the implemented primary breakup model with the most important connections between the different sub-models and the other solvers.

In order to inject parcels into the Lagrangian solver, injection location and droplet characteristics have to be determined. Thus, in the developed model, great attention has been devoted to the two following aspects:

[1]It should be noted that other numerical approaches, such as VOF/level-set, can be used to directly simulate the breakup process [25], however these methods are very time-consuming and thus they are not useful for industrial applications.

- definition of injection location;
- computation of droplet characteristics (in particular diameter and velocity).

In the following, numerical strategies and models used for the definition of the injection location and the computation of the characteristics of spray population introduced in the Lagrangian solver will be described with great detail.

5.2.1 Injection location

As shown in Fig. 5.3, the definition of the injection location requires two main inputs:

- a separation criterion able to detect the location along the surface mesh used for liquid film solution where droplets are prone to detach from the liquid film;
- information about the breakup length and spreading angle in order to recover some of the physical characteristics of the breakup process, as it will be better explained in the following.

As far as the separation criterion is concerned, two different strategies have been considered. First of all, a criterion based on geometric curvature could be used, for example the approach by Owen and Ryley [134], specifically devised for flows around sharp corners where a balance between inertia, gravity and surface tension forces is exploited, or the approach described in [126]. In this case the separation location is not prescribed in advance and can vary during the simulation so it is important to extend the liquid film mesh around the atomizing edge as shown in Fig. 5.4(a). All the liquid mass present in the cell where separation is predicted has to be converted in Lagrangian particles. Film separation determines losses in mass, momentum and energy for the liquid film which are accounted for in the film conservation equations by means of specific source terms. However, since in prefilming airblast systems the location of liquid film separation is usually known, that is the atomizing edge, a more

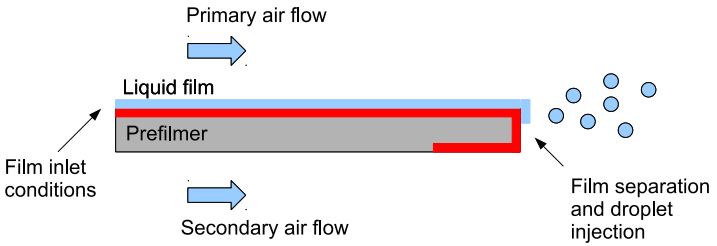

(a) Criterion based on surface curvature.

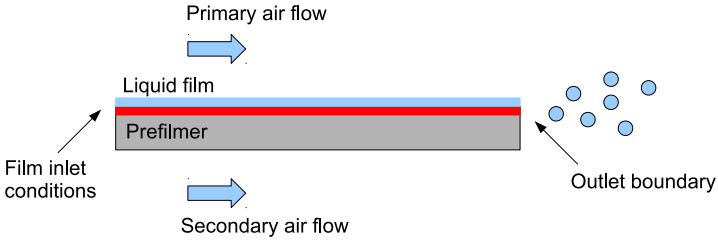

(b) Outlet boundary for the liquid film.

Figure 5.4: Different strategies for determining droplet separation location (film solver mesh is reported in red).

straightforward approach can be used. It basically consists in defining an outlet boundary for the liquid film placed at the atomizing edge (see Fig. 5.4(b)). This approach is easier to be coupled with the steady-state solver since the liquid film mass flow rate crossing the boundary directly defines the mass flow rate of droplets injected in the computational domain. It should be noted that in this case no particular source term has to be included in the film equations since the mass flux which describes droplet separation directly leaves the film computational domain through the outlet boundary.

Since in the developed solver the liquid film mesh is build over solid boundaries, separation locations predicted with the methods previously described are always placed in correspondence of solid surfaces. However, as described in Section 5.1, the atomization process is usually completed downstream of the atomizing edge. Therefore, the

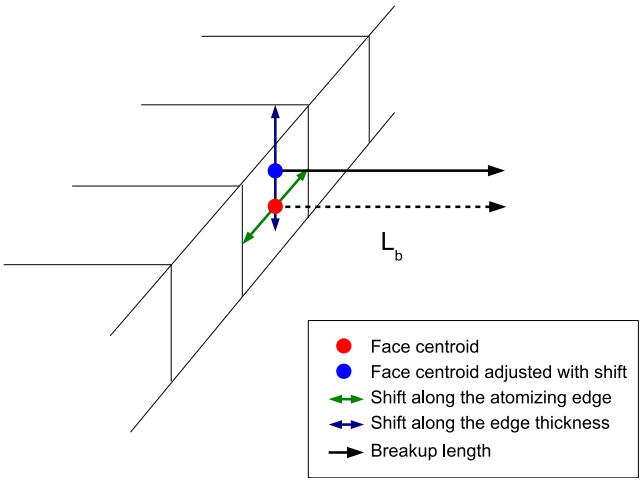

Figure 5.5: Strategy to determine the injection location.

location determined by the separation criterion could not be representative of the actual injection location and more information should be given to make the breakup model more realistic. In the developed model the separation criterion is just used to define the cell of the film mesh where separation occurs and the actual injection location is recovered through the definition of a breakup length. In the following, the case of film separation location defined through an outlet boundary is considered.

Considering a generic face of the outlet boundary, the injection location is computed starting from the face centroid by adding the breakup length along the face normal vector. Random functions are used to move the face centroid in the space between the two adjacent cells so that the parcels are not always injected in the same point. Furthermore, additional parameters are used to define particular injection configurations aimed at reproducing fuel distribution between the primary and secondary air flows, as will be explained in the following. A schematic description of the adopted procedure is reported in Fig. 5.5. The red point represents the face centroid. This point is moved with a random function in the direction tangent to the pre-

filming edge (green line) so that all the positions along the atomizing edge can be considered. Furthermore, a shift given by the combination of a constant value and a random function can also be applied in the direction normal to the atomizing edge (blue line) so that an injection surface can be defined also allowing the implementation of different injection strategies. The parameters regulating the shift, that is the constant value and the amplitude of the random sampling, are given as external inputs by the user. Finally, starting from the point determined after the application of the aforementioned shifts, the breakup length is added in the direction normal to the face.

It should be noted that, in general, droplet could be entrained by both primary and secondary air flows (especially in the case of liquid film accumulation at the atomizing edge). Therefore, great attention should be devoted to the choice of the breakup model parameters described above in order to define an injection location able to properly represent the fuel distribution between the two air flows. Fig. 5.6 shows possible strategies to describe different entrainment configurations. If just one of the two flows (for example the primary flow) is dragging off the droplets, the strategy represented in Fig. 5.6(a), where droplets are directly injected along the corresponding flow streamlines, could be the best choice. On the other hand, when droplets are entrained by both primary and secondary air flows a good strategy could be to inject droplets in front of the atomizing edge (see Fig. 5.6(b)). A proper value of the breakup length should be used in order to avoid to place the injection locations in the low-velocity region that forms immediately downstream of the atomizing edge (wake-like structure). Another possible strategy implemented in the code is represented in Fig. 5.6(c). In this case the injection is artificially split into two streams placed respectively above and below the atomizing edge so that particles are taken away by both primary and secondary air flows. In addition to the parameters described above, in this case the user should also define the mass flow split and the radial distance between the two injection locations. Some indications for the choice of the best modelling strategy will be given in Section 5.4.

Finally, because of liquid film flapping induced by the two air flows (see for example Fig. 2.4 where a planar liquid sheet is considered), droplets generated by the liquid film primary breakup are released

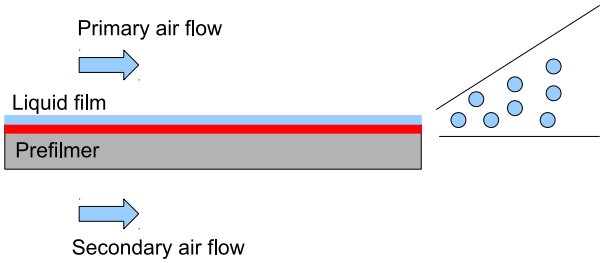

(a) Injection in the primary flow.

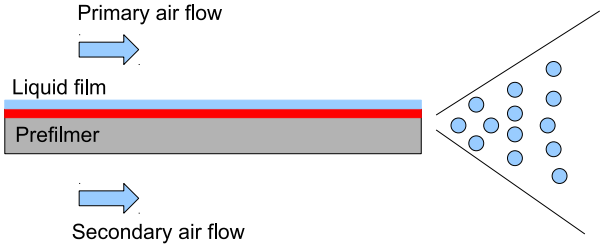

(b) Injection at the center of the atomizing edge.

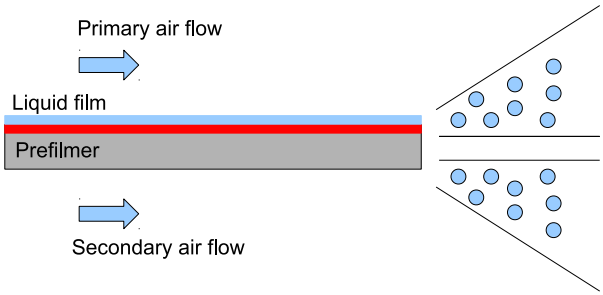

(c) Split injection.

Figure 5.6: Possible injection strategies to reproduce different entrainment configurations.

with a certain spreading angle. In the current implementation it is also possible to define a spreading angle which is used the compute the actual injection direction by rotating the velocity vector around an axis tangent to the atomizing edge. In addition to the injection strategies described above, a proper definition of the spreading angle could allow us to recover a realistic fuel distribution between primary and secondary flows.

It is important to note that in the implemented model breakup length and spreading angle could also be defined through experimental correlations whenever they will be available. As far as the breakup length is concerned, a very interesting investigation is the one proposed by Carvalho and Heitor [135]. The breakup of an annular sheet interacting with two turbulent coaxial jets (respectively, inner and outer jets), with and without swirl, was experimentally investigated. The experiments were carried out at atmospheric pressure using water with different liquid flow rates and velocities for the outer and inner air flows (different swirl levels were also imposed to the outer flow). Furthermore two values of liquid film thickness were considered. According to the experimental observations, the liquid film thickness seems to affect the breakup process only at low air velocities whereas at high velocities the breakup characteristics, in particular the breakup length, appear less dependent on film thickness. The presence of the swirl leads to shorter breakup lengths which become very small at high velocities (prompt atomization regime).

5.2.2 Spray characteristics

Once the injection location is determined, proper characteristics should be assigned to the droplets injected in the spray solver. Injection velocity and thermo-physical properties are taken equal to the corresponding values characterizing the liquid film at the separation location whereas the droplet diameter is computed starting from a SMD value and a proper distribution function (for example Rosin-Rammler distribution). In the implemented model, two different methods can be used for the SMD computation:

- experimental correlations;
- theoretical models.

In the following correlations and theoretical models will be described in more detail. In particular, a review of the most important theoretical models will be presented and possible modifications to existent models in the light of the breakup mechanism described in Section 5.1 will be proposed.

5.2.2.1 Experimental correlations

In general, theoretical models that try to reproduce the physics of liquid film atomization suffer the lack of a comprehensive theory on the mechanisms of primary breakup (however, as shown in the following, simple theoretical models may lead to very interesting results). As a consequence, especially in an industrial context, experimental correlations are often preferred. In past years, several studies aimed at determining the most important parameters affecting primary breakup were performed considering both real atomizers and simplified planar injectors. Starting from experiments, correlations to predict droplet sizes in such atomizers were developed. A review of the main correlations can be found in references [33, 73]. Droplet population SMD mainly depends on air velocity, liquid surface tension and dynamic viscosity and a characteristic length which, depending on the correlation, could be the edge thickness, the film thickness or a representative dimension of the atomizer. Film properties at the atomizing edge are determined by liquid film evolution over the prefilming surface and in the present approach they are directly derived from the liquid film solution.

A very interesting correlation is the one proposed by Gepperth et al. [133]. This correlation was derived using experimental measurements made very close to the atomizing edge and therefore the secondary breakup phenomena have a negligible impact on the measured data. As a consequence of the liquid film accumulation at the atomizing edge observed in the range of test conditions considered in these experiments, it has been found that the SMD is mainly affected by the mean air velocity and the atomizing edge thickness whereas the film thickness and the prefilming length have a minor effect on the droplet mean diameter. According to this correlation, droplet

SMD is given by the following expression:

$$\begin{aligned}\frac{SMD}{\delta_{x,edge}} = \; & 4.96\left(\frac{\rho_g U_g \delta_{x,edge}}{\mu_g}\right)^{-0.17}\left(\frac{\rho_g U_g^2 \delta_{x,edge}}{\sigma}\right)^{-0.36} \\ & \left(\frac{\rho_L}{\rho_g}\right)^{-0.013}\left(\frac{h}{\delta_{x,edge}}\right)^{0.46}\end{aligned} \tag{5.1}$$

where $\delta_{x,edge}$ is the turbulent boundary layer thickness at the atomizing edge evaluated as [133, 136] (L_{surf} is the prefilmer chord length):

$$\delta_{x,edge} = 0.16\frac{L_{surf}}{\left(\frac{\rho_g U_g L_{surf}}{\mu_g}\right)^{1/7}} \tag{5.2}$$

Many other formulations can also be found in literature [33]. Some of them have an explicit dependence on film thickness[2] which in the developed approach is directly derived from the liquid film solution. An example of these correlations is the one proposed by Rizkalla and Lefebvre [137, 138] where the film thickness was introduced to obtain a dimensionally correct expression. In this work, the expression of the Rizkalla and Lefebvre correlation reported in [73] is considered:

$$\begin{aligned}SMD = \; & 3.33\times10^{-3}\frac{(\sigma\rho_L\delta)^{0.5}}{\rho_g U_g}\left(1+\frac{1}{AFR}\right) \\ & +13.0\times10^{-3}\left(\frac{\mu_L^2}{\sigma\rho_L}\right)^{0.425}\delta^{0.575}\left(1+\frac{1}{AFR}\right)^2\end{aligned} \tag{5.3}$$

In other cases a characteristic dimension of the injection system is taken as reference length scale. This is, for example the case of the El-Shanawany and Lefebvre correlation [139] where the prefilmer diameter D_p appears in the formulation:

$$\begin{aligned}SMD = \; & 0.073\left(\frac{\sigma}{\rho_g U_g^2}\right)^{0.6}\left(\frac{\rho_L}{\rho_g}\right)^{0.1}D_p^{0.4}\left(1+\frac{1}{AFR}\right) \\ & +0.015\left(\frac{\mu_L^2 D_p}{\sigma\rho_L}\right)^{0.5}\left(1+\frac{1}{AFR}\right)\end{aligned} \tag{5.4}$$

[2]This clearly indicates that the role of film thickness in airblast atomization is not completely understood and further investigations are required as observed in Section 5.1.

It is important to consider this kind of expressions because typical industrial correlations are often based on similar formulations with constants calibrated according to the given injector geometry. However, as also discussed in [73], it should be noted that these correlations generally predict too small SMD values compared to recent investigations since the measurement data used to derive them were usually collected in a region where secondary atomization effects can obscure the initial droplet sizes in the primary breakup region.

Correlations are often derived using geometrical configurations and test conditions far from typical industrial applications and thus they have to be used with great caution.

5.2.2.2 Theoretical models

The breakup of liquid films has been studied in several theoretical works [57] leading to the development of models that can be directly exploited in numerical solvers. Generally speaking, contrary to correlations, the range of validity of theoretical models is determined by the assumption made in their derivation (in particular the breakup mechanism). Furthermore, in general, they require liquid film thickness and velocity at the atomizing edge to be known which, however, in the approach proposed in this work, are readily available as a result of the liquid film solution. Different models have been implemented in the code. In the following a comprehensive description of them is given.

Dombrowski and Johns model. The first model that has been considered is the one developed by Dombrowski and Johns [59] which is based on a stability analysis of a liquid film injected in a stationary gas with the breakup mechanism schematically represented in Fig. 5.7. Interactions between the liquid film and the gas-phase cause the development of instabilities which grows in amplitude until a critical value is reached. The most unstable wave leads to the formation of ligaments (one ligament per half wavelength) that move normal to the ligament axis and break up into drops as a consequence of capillary forces. The ligament diameter is computed as:

$$d_{lig} = \sqrt{\frac{4\delta_b}{n}} \tag{5.5}$$

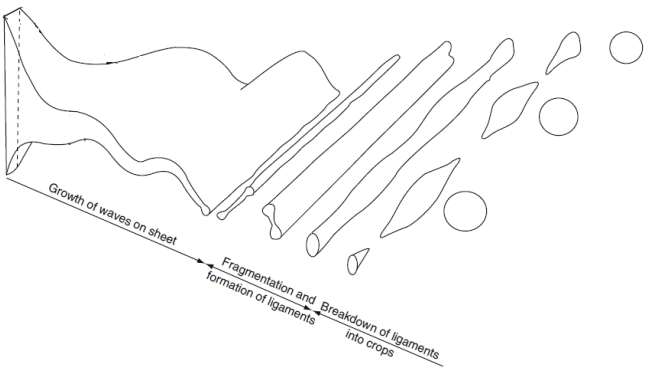

Figure 5.7: Breakup mechanism considered in the Dombrowski and Johns model (taken from [59]).

where δ_b is the film thickness at the breakup location (it can be assumed equal to the film thickness at the atomizing edge or an attenuating sheet can be considered) and n is the wave number of the most unstable oscillation which is a function of the film thickness and is computed from the stability analysis. In the case of a parallel-sided sheet (δ is independent of time) n is given by:

$$n = \frac{F^2 \rho_g U_R^2}{2\sigma} \tag{5.6}$$

with F equal to the ratio of wave growth of viscous liquid to the inviscid value. The maximum value of F which allows us to compute the most unstable wavelength is given by the following equation:

$$1 - F^2 - VF^3 = 0 \tag{5.7}$$

where:

$$V = \frac{\mu_L \rho_g U_R^2}{2} \left(\frac{\delta}{2\rho_L \sigma^3} \right)^{0.5} \tag{5.8}$$

As said above, in this model the ligaments generated after the liquid sheet breakup are supposed to move transversally through the atmosphere. Under these conditions, the gas-phase has no effect on the ligament breakup. Thus the capillary mechanism can be assumed to apply and Eq. 2.14 can be used for the computation of droplet diameter:

$$d = \left(\frac{3\pi}{\sqrt{2}}\right)^{1/3} d_{lig}\left(1+3\frac{\mu_L}{\sqrt{\rho_L \sigma d_{lig}}}\right)^{1/6} = \left(\frac{3\pi}{\sqrt{2}}\right)^{1/3} d_{lig}(1+3Oh)^{1/6} \tag{5.9}$$

This value could be directly assigned to the parcel to be injected as a consequence of the film breakup. However, in the current implementation, the diameter computed in this way is assumed to be the most probable diameter of a Rosin-Rammler distribution. Once the dispersion parameter q is given, all the parameters of the distribution are uniquely determined (see Section 2.4.2) and the droplet diameter is sampled from the distribution with a random function.

It is important to point out that in this model the SMD computation requires an estimation of the film thickness at the atomizing edge which in the developed approach can be directly evaluated through the liquid film solution. Under the assumption that the most important mechanisms of primary breakup in prefilming airblast injectors are similar to the ones described by this model, this formulation can also be used for the advanced injectors considered in this research. This assumption is to some extent supported by the work of Gepperth et al. [140] who compared the SMD predicted by this model with their experimental data finding a general good agreement with measurements performed in the downstream region (where secondary breakup effects make the diameter smaller). However, an underestimation of SMD measured close to the atomizing edge was found. Looking at the breakup mechanism described in Section 5.1, the breakup process considered in the Dombrowski and Johns model could be representative of the disintegration of the reservoir and the rim ligaments formed at the atomizing edge [140]. The fragmentation of the bag-like structures is not considered, however the use of film thickness, which in the experiments performed by Gepperth et al. was much

lower than the edge thickness, as a length scale parameter could lead to small SMD values.

This theoretical model was also successfully applied to an airblast atomizer by Rizk and Mongia [141]. The injection system investigated in this work was characterized by a very short prefilming surface leading to a negligible effect of air flow on the film evolution which was mainly controlled by swirl chamber and atomizing lip geometry. In this case, the breakup mechanism described by Dombrowski and Johns appears representative of the actual physical process since no reservoir effect is expected at the atomizing edge.

Modified Senecal et al. model. Starting from the atomization mechanism described by Dombrowski and Johns [59], Senecal et al. [60] developed an improved model identifying a critical Weber number (based on film thickness and gas density[3] $We_f = \rho_g U^2 \delta/(2\sigma)$) which separates two different atomization regimes.

For $We_f < 27/16$ the so called *long wave regime* occurs. Following the Dombrowski and Johns breakup mechanism, the ligament diameter is computed as:

$$d_{lig} = \sqrt{\frac{4\delta}{K_s}} \tag{5.10}$$

where K_s is the wave number of the most unstable wavelength computed as the value of k that maximises the following dispersion relation for the growth rate:

$$\omega = -2\frac{\mu_L}{\rho_L}k^2 + \sqrt{4\frac{\mu_L^2}{\rho_L^2}k^4 + \frac{\rho_g}{\rho_L}U^2\frac{2k}{\delta} - \frac{2\sigma k^2}{\rho_g \delta}} \tag{5.11}$$

In the long wave regime the viscosity has a minor effect on the growth rate and a good approximation of K_s can be obtained from the in-

[3] In the original work of Senecal et al. [60] a liquid film moving in a quiescent medium was considered, thus the velocity to be used in the Weber computation is the liquid film velocity. In this work the formulation has been applied to an airblast injector and the velocity U has been assumed to be the relative velocity between the liquid film and the gas-phase.

viscid solution of the dispersion relation:

$$K_s = \frac{\rho_g U^2}{2\sigma} \tag{5.12}$$

Finally, once the ligament diameter is computed, the droplet diameter is obtained using Eq. 5.9.

On the contrary, when $We_f > 27/16$ the so called *short wave regime* approximation can be used. In this case the ligament diameter is given by (it is assumed that sheet instability leads to the formation of one ligament per wavelength):

$$d_{lig} = \sqrt{\frac{8\delta}{K_s}} \tag{5.13}$$

where the most unstable wave number K_s is the value of k that maximises the following dispersion relation:

$$\omega = -2\frac{\mu_L}{\rho_L}k^2 + \sqrt{4\frac{\mu_L^2}{\rho_L^2}k^4 + \frac{\rho_g}{\rho_L}U^2k^2 - \frac{\sigma k^3}{\rho_g}} \tag{5.14}$$

Also in this case the droplet diameter is computed from the ligament diameter using Eq. 5.9. Droplet diameter determined in this way is then used as the most probable diameter of a Rosin-Rammler distribution.

Comparing the dispersion relations of long wave and short wave regimes (Eq. 5.11 and Eq. 5.14 respectively), it is possible to note that in the short wave regime the instability growth rate is not affected by the film thickness. This theoretical finding has some aspects in common with the experimental observations made by Gepperth et al. [73] who, as described above, found that the SMD is not dependent on the film thickness, proposing the edge thickness as the most influencing length scale parameter. In light of these considerations, a modified version of the Senecal et al. model is proposed, introducing the atomizing edge thickness in place of film thickness as the reference length for the computation of the ligament diameter in the short

wave regime (Eq. 5.13):

$$d_{lig} = \sqrt{\frac{8\alpha h}{K_s}} \tag{5.15}$$

where α is a model parameter that in the present work was taken equal to 0.5. The formulation in the long wave regime has not been modified since with a very thin film thickness or a very low air velocity [133] the breakup mechanism could deviate from the mode based on liquid film accumulation and the original formulation of the Senecal et al. model is preferred. Diameters computed with Eq. 5.10 and Eq. 5.15 could be very different from each other since the atomizing edge thickness is often an order of magnitude bigger than the film thickness. In order to avoid abrupt changes of ligament diameter in the vicinity of the critical value of We_f, a blending function was introduced so that the length scale parameter gradually changes from the film thickness to the atomizing edge thickness. This function can be incorporated into the parameter α so that:

$$\alpha = \frac{1}{2h}\left[\delta + (h-\delta)\tanh\left(\frac{We_f}{We_{f,T}}\right)\right] \tag{5.16}$$

The transition to the edge accumulation regime is regulated through the parameter $We_{f,T}$ which in the present implementation has been taken equal to 27/4.

Gepperth et al. model. With the main aim of introducing a model suitable to be used in numerical codes, starting from the breakup mechanism observed in experiments, Gepperth et al. [140] developed a model based on the breakup frequency that does not require the film thickness as an input parameter. It is assumed that liquid film accumulation at the atomizing edge leads to the periodic formation of cylindrical ligaments. Mass conservation and breakup frequency are used to calculate the ligament diameter. Then the ligaments, because of capillary instability, breakup to form large drops which immediately undergo secondary atomization through a bag breakup mechanism. The diameter of droplets before bag breakup

is computed as:

$$d \approx 3.130\sqrt{\frac{\Lambda_f x_{in}}{U_g}}\left(\frac{\rho_L}{\rho_g}\right)^{1/2} Re_{in}^{-1/4} \tag{5.17}$$

where x_{in} is the inlet length of the experimental rig and Re_{in} is the air inlet Reynolds number. Gepperth et al. [140] also suggested an expression for the computation of SMD after bag breakup. However, as also pointed out by the authors, if the model is used in an Eulerian-Lagrangian numerical code, the diameter of the parcel can be computed directly using Eq. 5.17 exploiting the secondary breakup models of the Lagrangian formulation to determine the final droplet diameter after bag breakup.

The model was assessed and calibrated using available experimental data [140], thus can be safely applied only in conditions close to the experimental range.

Chaussonnet et al. model. This model, devised by Chaussonnet et al. [8] during the FIRST project, is based on the transversal instability prediction and it is calibrated to fit experimental measurements by Gepperth et al. [133]. Following the mechanism described in [129], droplet breakup is related to the growth and instability of transversal liquid structures whose dimension is supposed to be proportional to the edge thickness:

$$SMD = 2\pi C\sqrt{\frac{6\sigma\alpha h}{C_D\rho_g(U_g - U_C)^2}} \tag{5.18}$$

C_D is the drag coefficient of the liquid structure, usually close to one [129], C is a constant equal to 0.1166 and α is a constant representing the characteristic length of accelerated liquid compared to the prefilmer thickness. α ranges between 0 and 1 and in the present model has been taken equal to 0.67. Finally, U_C is the interface velocity which has been computed using the following expression [129]:

$$U_C = \frac{\rho_g^{1/2}U_g + \rho_L^{1/2}U_L}{\rho_g^{1/2} + \rho_L^{1/2}} \tag{5.19}$$

Chaussonnet et al. also proposed a correlation for the computation of the dispersion parameter q of a Rosin-Rammler distribution which is able to fit the experimental data of Gepperth et al. [133], with the parameter X of the Rosin-Rammlet distribution computed starting from the SMD value of Eq. 5.18 by means of Eq. 2.24.

$$q = \frac{\kappa}{\sqrt{We}} + (ah + b) \tag{5.20}$$

where $We = \rho_g u_{70}^2 y_{70}/\sigma$ (u_{70} is equal to the 70% of the free stream velocity and y_{70} represents the height in the boundary layer where the local velocity is equal to u_{70}), $\kappa = 1.76$, $a = 112\ \mathrm{m}^{-1}$ and $b = -0.043$. It should be noted that the value of q suggested by this correlation can also be exploited in the other models for the droplet diameter computation in order to give a reliable value to the dispersion parameter of the Rosin-Rammler distribution.

In the breakup mechanism described in Section 5.1, the breakup phenomenon considered in this model could be representative of the breakup of the reservoir rim. The bag breakup of the bubble-like structures is not directly included, however the formulation considers all the main parameters affecting the primary atomization, that is air velocity, atomizing edge thickness and surface tension, and a comprehensive evaluation of the mean diameter can be achieved through a proper calibration of the model constants.

Inamura et al. model. The last model considered here is the one devised by Inamura et al. [128]. Differently from Gepperth et al., in their experiments Inamura et al. found a dependence of the atomization process on the film thickness and the instability phenomena at the interface between liquid film and gas-phase along the prefilming surface. Thus, they described the liquid film primary atomization as a combination of breakup of ligaments derived from both longitudinal and transversal waves generated on the film surface. Surface instabilities lead to the formation of U-shaped ligaments which breakup as a consequence of capillary forces. Finally, the largest droplets may be disintegrated again into fine droplets as a consequence of secondary atomization phenomena. This model represents the fragmentation of the rim of the bag-like structures whereas the droplets generated by

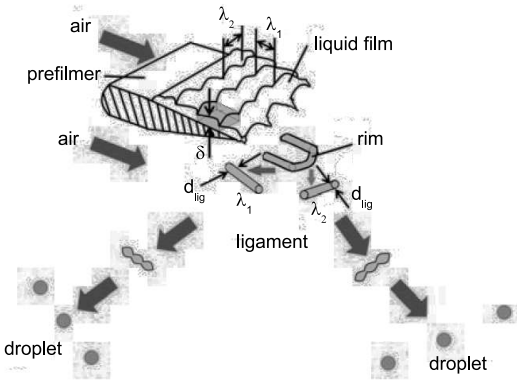

Figure 5.8: Breakup mechanism considered in the Inamura et al. model (taken from [128]).

burst of the bag are neglected since, according to Inamura et al., they give a small contribution to the mean droplet size.

The breakup mechanism considered in this model is schematically represented in Fig. 5.8. Waves in the liquid flow direction are assumed to be generated according to the Kelvin-Helmholtz instability. Thus, the wavelength in the liquid flow direction is expressed as:

$$\lambda_1 = CL_\omega \sqrt{\frac{\rho_L}{\rho_g}} \tag{5.21}$$

where C is a correction factor taken equal to 1.6 and L_ω is the thickness of the boundary layer computed through the following expression:

$$L_\omega = 3.56 \frac{H_g}{\sqrt{Re_{H_g}}} \tag{5.22}$$

H_g is the width of the channel and Re_{H_g} is the gas-phase Reynolds number based on the channel width ($Re_{H_g} = \rho_g U_g H_g / \mu_g$). As regards the waves in the transverse direction, the Rayleigh-Taylor instability phenomenon is supposed to occur and the wavelength in the

transverse direction is computed as:

$$\lambda_2 = 2\pi\sqrt{\frac{6BC}{C_D}}L_\omega\left(\frac{\rho_L}{\rho_g}\right)^{1/4}\sqrt{\frac{\sigma}{\rho_g(U_g-U_L)^2L_\omega}} \tag{5.23}$$

where B indicates a correction factor equal to 0.25 and C_D is a drag coefficient equal to 2.01. Finally U_L is the liquid film velocity which in the present implementation is directly derived from the liquid film solution. The ligament diameter is then computed as:

$$d_{lig} = 2\sqrt{\frac{\lambda_1\lambda_2\delta}{\pi\left(2\lambda_1+\frac{\pi}{2}\lambda_2\right)}} \tag{5.24}$$

Finally, the diameter of droplets generated by the ligament breakup are calculated using Eq. 5.9 (also in this case it is assumed that the ligament breakup follows the capillary mechanism according to the Weber's theory). Droplets generated by ligament breakup are usually very coarse and may undergo further breakup. The final disintegration of these large droplets has to be accounted for through a proper secondary breakup model.

Inamura et al. assessed their model by comparing numerical predictions with measurements performed downstream of the atomizing edge. The TAB model was used to include the effects of secondary atomization in the numerical predictions. A general good agreement with experiments was found with a slight underprediction of experimental SMD values at high air flow velocities. Once again, it is important to note that in this model the ligament formation is assumed to be connected to the development of film instabilities along the prefilmer surface. However, in the experiments by Gepperth et al. [73] where a much thicker atomizing edge was used, it was observed that the atomization process and breakup frequency were completely uncorrelated with the development of film surface instabilities. This highlights the possible influence of the atomizing edge thickness on the decoupling of breakup process from liquid film evolution along the prefilming surface and the necessity of further investigations on the role of atomizing edge thickness in the breakup process.

In the current implementation, the diameter of injected droplets is computed by assuming the diameter of droplets generated after ligament breakup as the most probable diameter of a Rosin-Rammler distribution. The secondary breakup of large droplets is accounted for immediately after injection through the use of a secondary breakup model in the Eulerian-Lagrangian formulation. Furthermore, the choice of a proper secondary breakup model could also allow us to recover the presence of small droplets generated by the bursting of bag-like structures.

5.3 Stripping phenomenon

In the previous discussion it has been implicitly supposed that all the liquid present in the film (this liquid could have been directly injected as a thin film or could derive from mass addition due to droplet impingement) reaches the atomizing edge excepting the amount of fuel that evaporates from the film surface and droplets detached as a consequence of droplet impingement. However, when a liquid film is subjected to high velocity flows, some droplets could detach from the liquid surface [142, 129] because of the instability structures (for example the so called Kelvin-Helmholtz instabilities) generated at the interface between gas-phase and liquid film, in a process usually referred to as *stripping*. In very severe conditions and longer atomizer lengths, stripping could lead to full atomization before any of the liquid reaches the atomizing edge. Thus, before moving on to the investigation of real injector configurations, it is important to evaluate if the stripping phenomenon is important in the PERM atomizer investigated in this research.

During the FIRST project, a PERM injection system was experimentally investigated by Wollgarten et al. [143] at the Karlsruhe Institute of Technology (KIT). Experiments were performed at ambient pressure using water. Injector pressure losses and global air/liquid mass flow rate ratio considered in experiments were representative of engine operations. Although an investigation of the stripping phenomenon would require visualizations inside the nozzle which are not practicable in real injectors, in these experiments there was not evidence at the downstream locations of phenomena ascribable to mass

stripping, and, at conditions with 3.5% pressure drop (similar to the conditions considered in this research), it can be assumed that the complete film reaches the atomizing edge [144]. Only at a very high pressure drop of 6.9% (far from engine applications), huge droplets were observed near the injector axis. However the amount of droplets was very little (5-20 droplets) so that they did not affect the mass distribution. The authors of these experiments assumed that these droplets were stripped off the prefilmer or directly injected from the pressure atomizer without ever touching the lip [143, 144]. But this was just an assumption since, as stated before, observation inside the injector were not available. Therefore, these experiments reveal that at pressure losses and air-liquid ratios representative of engine operating conditions, in the configuration experimentally investigated the stripping phenomenon can be neglected.

However, before giving general conclusions about the behaviour of the PERM injection system at engine operating conditions, it should be noted that pressure drop and air-liquid ratio are not the sole relevant parameters affecting the stripping phenomenon but also the gas-phase density, the film thickness and the surface tension could play an important role in determining the detachment of droplets from the liquid film surface. From this point of view, an interesting investigation is the one performed by Bhayaraju and Hassa [142] where the stripping phenomenon over the prefilming surface of an airblast injector was experimentally studied. The authors found that stripping starts to appear at $We_f = \rho_g \delta U_R^2/\sigma \approx 100$ whereas for $We_f < 100$ detachment of mass from the liquid surface was not observed. In the engine conditions considered in this work (see Chapter 6), values of We_f greater than 100 can be found only at high pressure, in conditions representative of full load operation.

In literature some correlations and theoretical models for the stripping evaluation can also be found. An interesting work is the one proposed by Lopez de Bertodano et al. [145] where the water steady-state entrainment in high air velocity and at high pressure conditions was experimentally studied. A review of different literature correlations [146, 147] was performed and a new correlation based on the analysis of the growth of Kelvin-Helmholtz instabilities was proposed. Applying these correlations to the experiments of Wollgarten et al. [143], a stripped mass flow rate less than 1% of the

injected mass flow rate is predicted confirming the previous conclusions deduced from experimental observations. Furthermore, if the correlations are applied to the engine conditions considered in this work (see Chapter 6) a value of stripped mass flow rate less than 3% of the total film mass flow rate is found at partial load conditions whereas at conditions representative of full load operation a stripped mass of about 6% of the total liquid mass flow rate is predicted. It should be noted that these correlations usually refer to a steady-state entrainment condition whereas in the injection system under consideration the film flow cannot be considered fully developed along the whole prefilmer surface. Therefore, the stripped mass could be different from the value predicted by these correlations.

Considering experimental observations on the PERM injection system and the consideration made on the basis of experiments and correlations available in literature, in the present investigation the stripping phenomenon will be neglected. However, it should be noted that at high pressure conditions representative of engine full-load operation some phenomena ascribable to stripping could appear and in the future specific research should be devoted to the development of stripping models able to describe this phenomenon in liquid films driven by swirled flows.

5.4 Assessment and validation

Experimental measurements performed by Wollgarten et al. [143] on a PERM injection system have been used for the assessment and validation of the developed primary breakup model. Experiments were performed at atmospheric conditions using water with an unconfined configuration in order to avoid spray distortion due to the presence of chamber walls and to make easier optical measurements. Fig. 5.9 shows a schematic representation of the experimental configuration whereas Table 5.2 summarizes the most important fluid dynamic characteristics of the case considered for validation. All the liquid is injected through the pilot pressure atomizer and liquid film over the atomizing edge is generated as a consequence of droplet impact. Experiments showed that in this configuration basically all the injected liquid reaches the atomizing edge and evolves as a liquid film.

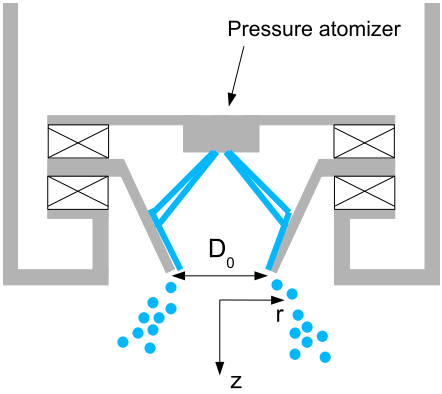

Figure 5.9: Schematic of the experimental configuration.

Table 5.2: Validation test case.

Quantity	**Value**
T_g [K]	298
p_g [Pa]	101325
$\Delta p/p$ [%]	3.5
Δp_{inj} [bar]	2.7
AFR [-]	27
SMD_{pilot} [μm]	67.6

Droplet size and mass flux were measured on a plane normal to the injector axis located $2.075D_0$ downstream of the injector exit plane where D_0 is the atomizing edge diameter.

In the following, numerical results will be compared with experiments in terms of global SMD and cumulative mass radial profile at the downstream plane where measurements were performed. The cumulative mass gives information about the radial distribution of the spray and, to some extent, the subdivision of droplets between the primary and secondary flows as will be described in the following.

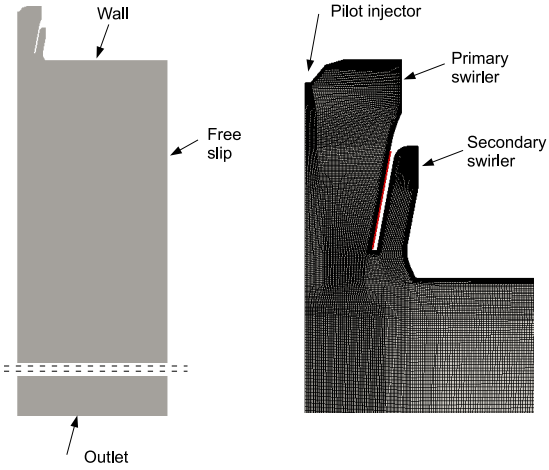

Figure 5.10: Computational domain and numerical mesh near the injection region.

5.4.1 Computational setup

The computational domain, shown in Fig. 5.10, represents a 1.5 degree sector of the experimental configuration. The swirling channels of the PERM injector were not modelled and swirled flows were imposed at the inlet boundaries (located at the exit of the swirling channels) by assigning a mass flow rate and the direction of velocity vectors. Air flow split between primary and secondary flows and velocity directions were obtained in a preliminary three-dimensional simulation of the entire injector. Axisymmetric behaviour was imposed through cyclic conditions on lateral sides. Static pressure was assigned at the outlet boundary whereas a free-slip condition was used for the external confinement boundary. Solid walls were modelled using adiabatic and no-slip conditions. Since measurements were performed in an unconfined configuration, the dimension of the computational domain was chosen large enough to avoid flow and spray distortion due to the presence of confinements walls.

The liquid film single-layer mesh was built over the prefilming

surface. Since in the experimental configuration all the film was injected through the pilot atomizer, no film was imposed at the film inlet boundary. Separation criterion based on the definition of an outlet boundary (see Fig. 5.4(b)) was chosen; therefore the outlet boundary of the liquid film mesh was directly placed at the atomizing edge.

Pilot atomizer was modelled by injecting a given population of parcels. Diameter distribution was reproduced using a Rosin-Rammler function with a representative diameter computed starting from the SMD value reported in Table 5.2 and a dispersion parameter q equal to 2.0. Injection angle was deduced from atomizer characteristics described in its technical data-sheet whereas the injection velocity was computed following the approach described in [60] where the injection velocity is related to the injection pressure Δp_{inj} by:

$$U_{inj} = k_v \sqrt{\frac{2\Delta p_{inj}}{\rho_L}} \tag{5.25}$$

with the velocity coefficient k_v given by:

$$k_v = \max\left[0.7, \frac{4\dot{m}_{inj}}{\pi d_{0,inj}^2 \rho_L \cos\theta}\sqrt{\frac{\rho_L}{2\Delta p_{inj}}}\right] \tag{5.26}$$

where $\dot{m}_{inj}$ is the injected liquid mass flow rate, θ is the spray angle and $d_{0,inj}$ is the injector exit diameter.

5.4.2 Results

Before presenting comparisons with experiments, it is important to show the basic features of the flow field generated by PERM injection system. As shown in Fig. 5.11 where the velocity field predicted in numerical simulations is reported, the double swirler configuration generates a vortex breakdown structure with an inner recirculation zone, typical of swirl-stabilized flames [31]. Furthermore, it is important to note that in numerical simulations more than 99% of the liquid mass injected by the pilot atomizer reaches the prefilming surface and evolves as a liquid film, in good agreement with experimental

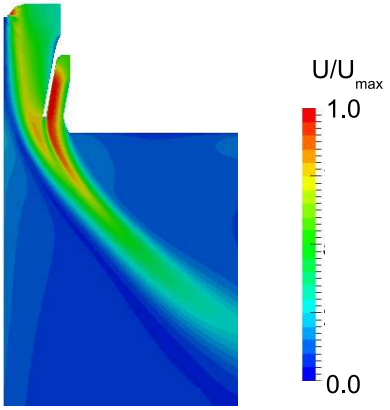

Figure 5.11: Velocity field magnitude near the injection system.

observations. The remaining part (very few droplets) do not reach the lip surface and it is carried away by the primary flow.

In Table 5.3 a comparison between different models and correlations for the computation of droplet diameter after primary breakup is presented. The SMD of injected particles is reported together with the SMD at the plane where experimental measurements were performed. The mean value of SMD evaluated in experiments is about 52 μm [143]. Before discussing the results obtained in the numerical investigation, it is important to note that the SMD at the experimental sampling plane is determined by both primary and secondary atomization which, as discussed in Section 5.2.2.2, in some models is also representative of the disintegration of bag-like structures or large fragments of ligaments generated by the primary breakup process. Looking at the numerical results, first of all, it should be noted that injection diameters predicted with the correlations of Rizkalla and Lefebvre [137] and El-Shanawany and Lefebvre [139] are very small in comparison with the value obtained with the correlation recently developed by Gepperth et al. [133]. This result is in agreement with the analysis performed by Gepperth et al. [73] who compared their experimental results with predictions performed with several correlations found in literature. As discussed in [73], old literature

Table 5.3: Comparison between models and correlations for the computation of droplet diameter after primary breakup.

Model/Correlation	SMD [μm] at injection	SMD [μm] at $z/D_0 = 2.075$
Rizkalla and Lefebvre correlation [137]	23	22
El-Shanawany and Lefebvre corr. [139]	34	32
Gepperth et al. correlation [133]	199	100
Dombrowski and Johns model [59]	88	83
Senecal et al. model [60]	100	91
Modified Senecal et al. model	182	82
Inamura et al. model [128]	222	130

correlations are usually based on measurements performed far away from the injection system where the effect of secondary breakup may obscure the diameter of droplets generated after the primary atomization. On the contrary, the measurements performed by Gepperth et al. were made very close to the atomizing edge making negligible the effect of secondary breakup on measured diameters. Therefore, typical correlations usually underestimate the value predicted by the correlation developed by Gepperth and co-workers. Furthermore, in this particular application, the SMD of injected particles obtained with the correlations of Rizkalla and Lefebvre and El-Shanawany and Lefebvre is even smaller than the value measured downstream of the injection system.

As far as numerical models are concerned, the original model by Senecal et al. and the model by Dombrowski and Johns predict very small injection diameters in comparison to the other theoretical models and the SMD value at the sampling plane is almost identical to the injection diameter meaning that only few droplets are subjected to secondary atomization (liquid evaporation is negligible). The same observation can been drawn for the results obtained with El-Shanawany and Lefebvre correlation and Rizkalla and Lefebvre correlation where the SMD at the sampling plane remains almost unchanged from injection. On the other hand, the injection SMD

predicted by the Inamura et al. model and the modified Senecal et al. model is quite larger than the value found at the sampling plane. The larger injection diameter leads to higher Weber numbers which make the effects of secondary atomization more pronounced. It should be noted that secondary atomization is completed immediately downstream of the injection location whereas no secondary breakup occurs near the downstream sampling plane, in good agreement with experiments where no secondary breakup effects were observed for $z/D_0 > 1.59$ [143]. As fas as the modified Senecal et al. model is concerned, it is important to note that in this particular test case, the value of We_f is very close to the critical value that separates short and long wave regimes and the blending function described in Section 5.2.2.2 is activated. Finally, comparing experimental correlations and theoretical models, it should be noted that the SMD of injected parcels obtained with the Inamura et al. model and the modified Senecal et al. model is in fairly good agreement with the diameter computed using the Gepperth et al. correlation.

Excepting the cases where El-Shanawany and Lefebvre correlation and Rizkalla and Lefebvre correlation are used where the droplet diameter is small since injection, comparisons with the experimental SMD show that the primary breakup model introduced in this work generally leads to an overestimation of droplet mean diameter. In addition to the characteristics of the models used to reproduce primary and secondary breakup, a possible cause of these discrepancies could be related to the computational setup used to solve the gas-phase. Vortex breakdown structures generated by swirled flows are usually characterized by high velocity fluctuations which cannot be caught with standard RANS approaches leading to an underestimation of the effect of flow fluctuations on the secondary atomization of droplets and consequently to bigger droplet diameters.

The other quantity considered for the assessment of the primary breakup model is the cumulative mass. Cumulative mass was experimentally determined through the patternator technique [143]. Corrections to the measured mass were applied in order to consider the different area determined by the increase in radius from the injector axis to the outer measurement locations. Assuming N different sampling locations in the radial direction, the cumulative mass can be

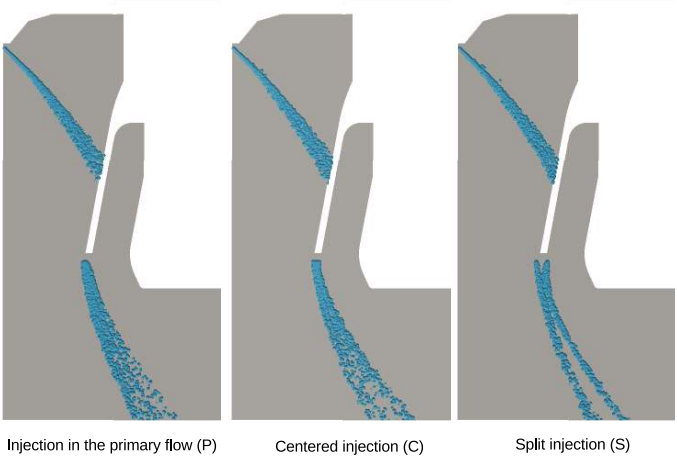

Figure 5.12: Application of different injection strategies to the PERM injection system.

defined as [143]:

$$M_j = \sum_{i=1}^{j} \frac{m_i}{\sum_{i=1}^{N} m_i} \tag{5.27}$$

where j is a given radial position. In numerical simulations this quantity has been determined in a similar way, identifying N sampling intervals along the radial direction.

Experimental profiles of cumulative mass were used to perform an assessment of different injection strategies. The configurations presented in Section 5.2.1 and shown in Fig. 5.6 were considered. The application of such strategies to the PERM geometry is reported in Fig. 5.12 together with the symbols that will be used in the following to indicate the different injection configurations.

- In the first strategy (P), droplets are directly injected in the primary flow, in front of the liquid film layer (this is the classical approach used in industrial computations). Numerical results reported in Table 5.3 were obtained using this strategy.

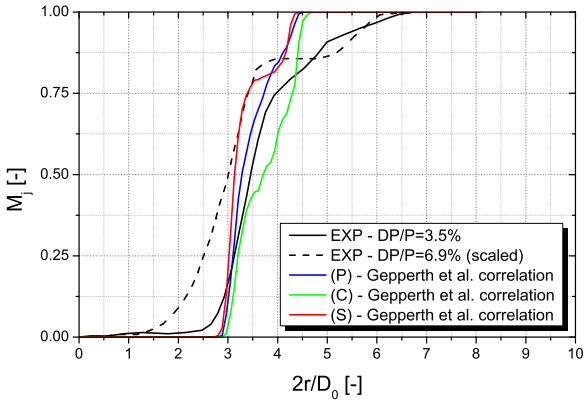

Figure 5.13: Comparison between different injection strategies in terms of cumulative mass.

- In second approach (C), parcels are injected in front of the atomizing edge. A proper value of the radial spreading is used in order to inject parcels in a surface corresponding to the entire atomizing edge thickness.

- In the last case (S), a split injection is used. Parcels are directly introduced in both primary and secondary flows with a given mass flow rate split.

Fig. 5.13 shows a comparison between experimental and numerical radial distributions of cumulative mass. These simulations were performed using the Gepperth et al. correlation for the computation of droplet diameter generated by the film breakup and a spreading angle of 60 degrees. Compared to experiments, numerical simulations show a lower spreading of the droplets with the spray that is confined in a more narrow region (the cumulative mass is equal to 1 at a smaller radius and becomes different from 0 farther away from the injector axis). As also observed in Section 3.6.2, the underestimation of the spreading of the spray is in general a drawback of RANS simulations where the unsteady structures responsible for droplet dispersion are not simulated and droplet interaction with turbulent structures is just

modelled through a dispersion model. A better agreement with experimental measurements could be obtained through the development of improved dispersion models. However, it should be noted that the prediction of droplet spreading is strongly related to the capabilities of the computational method to reproduce the main characteristics of the gas-phase velocity field and turbulence levels. In general, the vortex breakdown process generated by swirled flows is a fluid instability which, in principle, has no steady-state solution [13]. The magnitude of the vortices generated in the vortex breakdown process are in some cases extremely large and the solution found with steady-state analysis, where the flow is forced to be stationary, could be not so representative of the actual flow field and turbulence levels reducing the effects of flow fluctuations on particle dispersion [12]. In order to properly capture these phenomena, a three-dimensional unsteady simulation (LES) of the injector is necessary, however the very high computational cost makes this approach not suitable to be used in a design tool. Furthermore, in the particular case of airblast atomizers, it should also be noted that interactions between liquid film and air flows downstream of the atomizing edge lead to high oscillations in the radial direction (flapping) of the liquid structures generated before droplet detachment [52]. Thus, droplets are released with a high spreading angle increasing particle dispersion.

Looking at the different injection strategies, the results obtained with the first approach (P) seem to be closer to experimental measurements, however the underestimation of droplet spreading suggests that droplets are also carried away by the secondary flow and therefore droplets should be injected in both air flows. A very interesting result is the one obtained with the split (S) strategy. In this case two distinct droplet streams, one in the secondary flow and the other in the primary flow, appear. These streams are separated by an annular region where droplets are not present (this is in the range of radius where the cumulative mass is constant). This configuration is not so representative of experimental results at $\Delta p/p = 3.5\%$. However a similar spray pattern was found in experiments at very high pressure drop[4] (see dashed line in Fig. 5.13) meaning that when air velocity is

[4]Note that experiments at high pressure drop were performed on a scaled injector.

Table 5.4: Comparison between SMD predicted by different injection strategies.

Injection strategy	SMD [μm] at injection	SMD [μm] at $z/D_0 = 2.075$
Injection in the primary flow (P)	199	100
Centered injection (C)	200	128
Split injection (S)	199	85

very high this injection strategy could be the best choice to properly represent the spray distribution.

Finally, it is important to note that the different injection strategies also influence the value of the SMD at the downstream location. Table 5.4 shows a comparison between SMD mean values predicted using the three strategies considered before. The SMD at the injection location is very similar in the three cases (only small changes in liquid film and gas-phase properties). However, at the downstream location the different injection strategies lead to different values of droplet mean diameter. The injection in front of the atomizing edge (C) gives the highest SMD since droplets are mainly injected in the region immediately downstream of the atomizing edge where the steady-state solution is characterized by very low values of velocity (wake-like structure) reducing the effects of secondary atomization. Exactly the contrary can be observed in the split strategy (S) where the direct injection in the secondary flow, characterized by higher values of velocity (see Fig. 5.11), makes the effects of secondary atomization more pronounced resulting in a smaller mean diameter at the sampling location compared to the other two strategies.

5.5 Concluding remarks

A primary breakup model for liquid films has been introduced in the multi-coupled solver developed in this work allowing to include in the simulation the phenomena related to primary atomization of the film which are fundamental for the description of injection systems based

on prefilming airblast configurations. The proposed model exploits gas-phase and liquid film solutions for the computation of droplet characteristics after breakup with additional user-defined parameters to recover a more physically consistent representation of the injection location.

The primary breakup model was assessed against experimental measurements performed on a PERM injector at atmospheric conditions using water. Several correlation and theoretical models for the computation of the diameter of droplet generated after primary breakup were evaluated with a fairly good agreement in terms of droplet SMD in the downstream location. Furthermore, different injection strategies were assessed. It is important to note that droplet diameter downstream of the atomizing edge is determined by both primary and secondary breakup. Secondary atomization becomes more efficient in the case of poor primary breakup allowing the reduction of droplet diameter downstream of the atomizing edge. A direct evaluation of the primary breakup model requires measurements performed close to the atomizing edge. If detailed measurements in the primary breakup region are not available, only conclusions about the combined effect of primary and secondary breakup models can be drawn. Comparison with experimental measurements has also highlighted the inability of the computational setup used in the simulation to correctly reproduce the droplet spreading. The flow field generated by the PERM injector is very complex and the simple approach used for the gas-phase simulation is not able to properly predict the effects of velocity fluctuations on the droplet dynamics. However, this is not a limit of the proposed primary breakup model which is aimed at defining droplet characteristics of the parcel to be injected in the Eulerian-Lagrangian spray solver and it can also be exploited in advanced unsteady analysis which, as also shown in Section 3.6, are able to better describe particle dispersion and spray dynamics downstream of the injection location. Phenomena related to droplet spreading as well as droplet distribution between the primary and secondary flows should be investigated in future research since they could have a strong impact on fuel distribution inside the combustion chamber and consequently on the combustion process.

Finally, some recommendations for the choice of a proper model or correlation for the computation of droplet mean diameter after pri-

mary breakup should be given. Correlations directly give the value of the SMD of injected parcels, starting from thermo-fluid dynamic properties of the gas-phase and liquid film at the atomization point, and their use is generally suggested. However, it is important to note that correlations can be safely used only in the range of operating conditions used for their calibration. Furthermore, as discussed in [73] and as observed in the simulation of the test case used for the assessment of the developed model, typical correlations available in literature usually predict very small diameters which could not be representative of primary breakup. The main cause could be related to the fact that most of the correlations are based on measurements performed downstream of the atomizing edge where the effect of secondary breakup drastically reduces the diameter of droplets leading to the prediction of very small diameters. On the other hand, theoretical models aim at reproducing the physics of atomization through a mathematical description of the mechanism that generates instability and the final disintegration of the film. In the absence of a general theory on liquid film atomization, models are usually developed on the basis of a specific atomization mechanism. Thus, the development and also the selection of a proper theoretical model, first require the identification of the atomization mechanism representative of the operating condition to be investigated. In this work, a breakup mechanism similar to the one observed in recent experiments on planar prefilming configurations was assumed and modifications to existent theoretical models were proposed on the basis of the selected mechanism. However, further investigations should be performed in the future to give more insight into the breakup mechanism of real injector configurations.

Chapter 6

Application to a PERM injector in a tubular combustor configuration

In order to determine the impact of the liquid film solution in the prediction of spray dynamics and to show the improvements that can be obtained in the description of liquid fuel preparation in comparison with standard approaches which neglect the presence of the liquid film, the multi-coupled solver developed in this research has been applied to the study of a tubular combustor equipped with a PERM injection system.

In the following, results of such investigation will be presented. First of all, the combustor was simulated neglecting the presence of the liquid film using the computational setup generally used in industrial computations before this research. As a further assessment and validation of the implemented solver, computational results obtained in these simulations were compared with simulations performed with the commercial code Ansys CFX-v13.0. Then, the liquid film has been inserted in the computational domain and numerical results obtained including film modelling have been compared with the previous ones. Different operating conditions were considered. Furthermore an analysis of the liquid film evolution over the pre-filming surface is also presented.

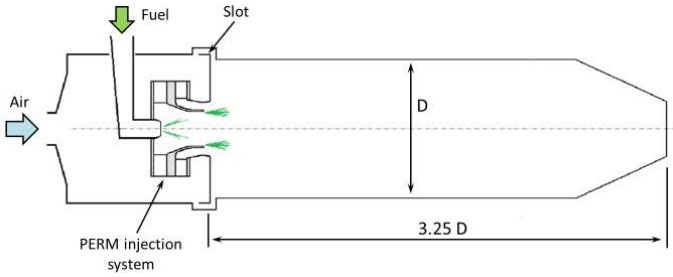

Figure 6.1: Schematic representation of the combustor geometry.

Table 6.1: Investigated cases.

	Case 1	**Case 2**	**Case 3**
$T_{g,in}$ [K]	613	656	811
p [bar]	5.3	13.5	22.4
P/T [%]	20	15	15
FAR [%]	4.06	3.86	3.52
$\Lambda_{f,in}$ [cm^2/s]	1.1	3.0	4.4
$\Delta p/p$ [%]	4.25	3.73	4.0

6.1 The investigated combustor

Fig. 6.1 shows a schematic representation of the combustor which consists in a cylindrical flame tube with a length to diameter ratio L/D equal to 3.25. Air enters the combustion chamber through the swirled channels of the injector and a slot located in the corner between the dome and the liner which discharges the air flow used for the impingement cooling of the dome.

Three different operating conditions, respectively representative of idle (Case 1), partial load (Case 2) and full load (Case 3) conditions, have been investigated. The main characteristics of the different cases are summarized in Table 6.1 (P/T is the pilot to total fuel mass flow rate ratio).

6.2 Computational setup

In order to reduce the complexity of the simulation, swirler blades were not included in the computational domain and, exploiting the symmetry of the geometry, the combustor was modelled using a sector of 1.5 degrees. Swirler inlet boundaries were placed at blade exit and inlet conditions were simply imposed by assigning azimuthal-averaged values obtained in a preliminary 3D simulation of the whole injection system. This computational setup is characterized by a very low computational cost and therefore it is suitable to perform a comparative analysis for the assessment of the role of liquid film in the description of liquid fuel preparation.

It should be noted that this computational setup does not allow us to include in the simulation spatial disuniformities due to the presence of swirler blades which could have an important effects on the flow field inside the injector. Furthermore, the RANS approach applied here and used as reference for the development of tools suitable for industrial applications, in general is not able to give a detailed solution of the complex phenomena regulating the combustion of swirl-stabilized spray flames for which a fully 3D LES simulation with advanced combustion models should be used. However, it is important to point out that the main objective of this investigation is not to perform a detailed analysis of the combustion process, but just to evaluate, at least from a qualitatively point of view, the improvements in the description of liquid fuel preparation that can be obtained introducing the film modelling in an industrial approach based on RANS simulations addressing to future research the detailed analysis of the effects of a more comprehensive description of liquid fuel preparation on the combustion process and engine emissions.

Fig. 6.2 shows the computational mesh (a hexahedral mesh of about 60000 cells with a single element in the azimuthal direction) in the region near the injection system. The single layer mesh used by the film solver is also reported. The liquid film is solved over the prefilming surface: the film inlet boundary is placed near the fuel injection holes whereas the outlet boundary is located at the atomizing edge (the criterion for liquid film separation based on the definition of an outlet boundary for the liquid film is used).

All the numerical simulations presented in the following were per-

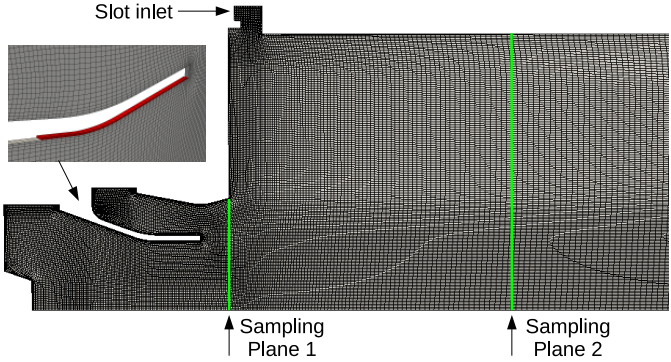

Figure 6.2: Computational mesh.

formed using a fully steady-state approach. Air swirled flows were reproduced by assigning a mass flow rate and the direction of velocity vectors (flow direction was found in the preliminary 3D simulation of the injection system) whereas at the slot inlet an axial air mass flow rate was imposed. A static pressure was assigned at the exit of the combustor whereas cyclic conditions were used for the lateral sides. Solid surfaces were modeled as adiabatic walls with a no-slip condition. As far as boundary conditions for the liquid film are concerned, uniform thickness, temperature and velocity at the film inlet boundary were imposed together with cyclic conditions on lateral faces.

A mono-component fuel with the chemical and physical properties of JET-A1 was used. The pressure atomizer was modeled by injecting a statistically representative population of parcels using a hollow cone model with a defined cone angle and a proper Rosin-Rammler distribution whereas the main injection due to liquid film primary breakup was modelled using the approach presented in Chapter 5. Droplet injection location due to the film primary breakup was computed using the computational strategy described in Section 5.2.1. As said above, film separation from solid walls was described through the definition of a film outlet boundary and a breakup length and a spreading angle were introduced in order to have a more physically realistic behaviour of the injection [140, 135]. As far as the evaporation model is concerned, the formulation derived from the work by Borman and

Johnson[92] was considered. Turbulent dispersion was accounted for using a stochastic approach (see Section 3.4.3) whereas droplet secondary breakup was modeled using the TAB model [102]. Results presented in the following were obtained using k-ω SST turbulence model [118] with wall-function approach (at the interface between liquid film and gas-phase the equivalent sand-grain roughness was considered) whereas the gas-phase combustion was modelled using a double step EDC model [19]. Finite rate kinetics effects were taken into account by keeping the local minimum between turbulent mixing rate and an Arrhenius type chemical reaction source computed by means of a two-step global scheme consisting in the fuel oxidation into CO and H_2O, and CO oxidation into CO_2 (the fuel is modelled as $C_{12}H_{23}$):

$$C_{12}H_{23} + 11.75O_2 \rightarrow 12CO + 11.5H_2O$$

$$CO + 0.5O_2 \rightarrow CO_2$$

Arrhenius coefficients introduced in this scheme can be found in reference [148].

6.3 Results

Results will be presented with the main aim of showing the improvements obtained introducing the liquid film modeling in an Eulerian-Lagrangian solver compared to the standard procedure of directly prescribing injection characteristics for parcels used to represent liquid film primary breakup. Thus, before analysing the results obtained with the multi-coupled approach developed in this work, simulations performed without a film model will be introduced as a reference case. Results are reported in terms of non-dimensional temperature T/T_{ref}, axial velocity U_z/U_{ref}, species mass fractions and mixture fraction radial profiles at two different planes. As shown in Fig. 6.2, the first one (Plane 1) is located near the injector exit whereas the second one (Plane 2) is located about 0.6D downstream of the combustor dome.

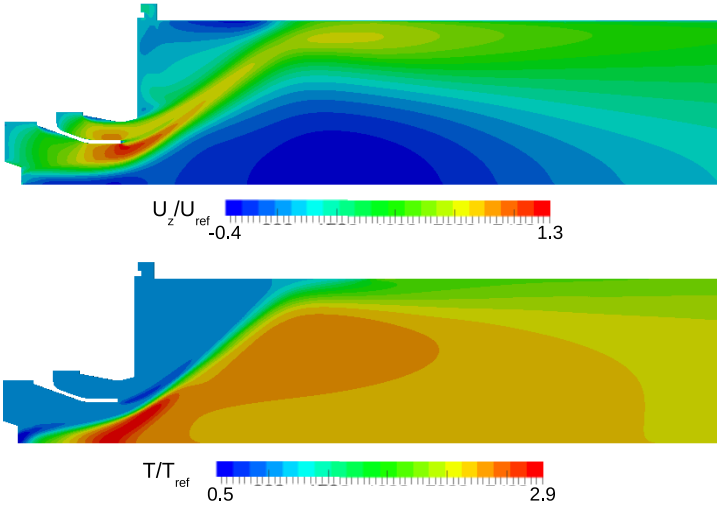

Figure 6.3: Axial velocity and temperature fields (Case 3).

6.3.1 Flow field

All the investigated cases are characterized by the same basic flow structures, typical of swirl-stabilized flames. Fig. 6.3 shows the axial velocity and temperature fields in the vicinity of the injection system of one of the examined cases. The presence of swirl in the flow allows the development of a strong vortex core along the axis with the typical vortex breakdown structure. The formation of a corner vortex in the region between the dome and the flame tube liner can also be noted. These structures, in particular the vortex breakdown, are very important for the combustion process allowing the formation of a stable flame which is further stabilized by means of the diffusion flame near the combustor axis generated by the pilot injector. It should be noted at this point that, although the most important flow features can also be observed in steady-state computations, because of the intrinsic unsteadiness of the vortex breakdown process (it is basically a flow instability), a steady-state solution where the process is forced to be stationary could lead to an underestimation of the effects of unsteady flow structures on the phenomena characterizing droplet and

combustion dynamics [12]. The vortex breakdown process is characterized by very strong velocity fluctuations which cannot be captured with RANS approaches. Therefore, as also observed in Section 5.4, the solution obtained with RANS simulations could lead to an underestimation of droplet spreading which could have important effects on the fuel distribution inside the combustion chamber affecting the combustion process. However, it is important to note again that the main objective of this dissertation was not the study of the combustion process and spray dynamics in swirl-stabilized flames but the development of numerical tools able to improve the description of liquid fuel preparation in standard RANS (U-RANS) computations through the introduction of liquid film modelling. Furthermore, in the present approach where the instabilities characterizing liquid film evolution are modelled, a more detailed solution of the gas-phase is expected to have similar effects on both simulations performed without and with film modelling, therefore the most important improvements introduced through the film modelling can also be described with the computational setup considered in this chapter.

The accuracy in the description of the physical processes characterizing droplet and combustion dynamics can be properly recovered with advanced time-resolved numerical approaches such as the LES which has demonstrated to be able to catch the most important unsteady phenomena in swirl stabilized spray flames [14, 15]. These methods should be undoubtedly considered in future research to better understand the effects of phenomena related to liquid film evolution on the combustion process, however they still require a very high computational cost to be used as a design tool in real injector configurations.

6.3.2 Solution without film modelling

As a common practice, in typical industrial calculations the presence of the liquid film is usually neglected and the injection due to the film primary atomization is modeled using an equivalent injector located at the atomizing edge. Therefore the possible impact of droplets injected by the pilot atomizer on the liquid film is not considered and the lip between the two swirled flows is simply modeled as rebounding solid surface. The simulations presented in this section

Table 6.2: Droplet characteristics.

	Case 1	**Case 2**	**Case 3**
Pilot: SMD [μm]	48	24	17
Film: SMD [μm]	52	28	20

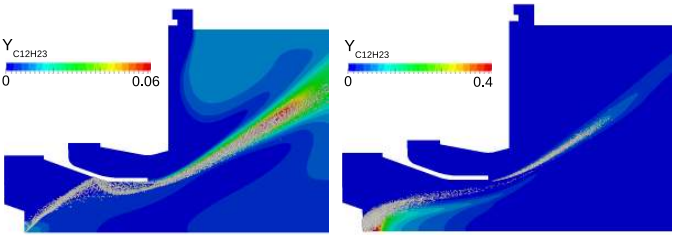

(a) Case 1 (b) Case 2

Figure 6.4: Droplet dynamics and fuel mass fraction - solution without film modelling.

were performed using this strategy. Droplet SMD was computed using an experimental correlation and the particle injection velocity was assumed to have an axial direction with a magnitude U_{inj}/U_{ref}=0.17 for all cases. As a further validation of the implemented Eulerian-Lagrangian spray solver, results obtained with the present solver will be compared with simulations performed with the commercial code Ansys CFX using an equivalent setup.

6.3.2.1 Case 1

As shown in Table 6.1, this case is characterized by a low pressure and a relatively high fuel-air ratio with the 20% of fuel that is injected using the pilot injector. Because of the high value of SMD (in Table 6.2 the SMD values of the different cases are compared with each other) and low values of air inlet temperature, the parcels fully evaporate far away from the injection location and, as shown in Fig. 6.4(a), particles injected through the pilot injector could reach the prefilming surface. These droplets, depending on the impact energy, may be adsorbed by the liquid film enhancing the fuel mass

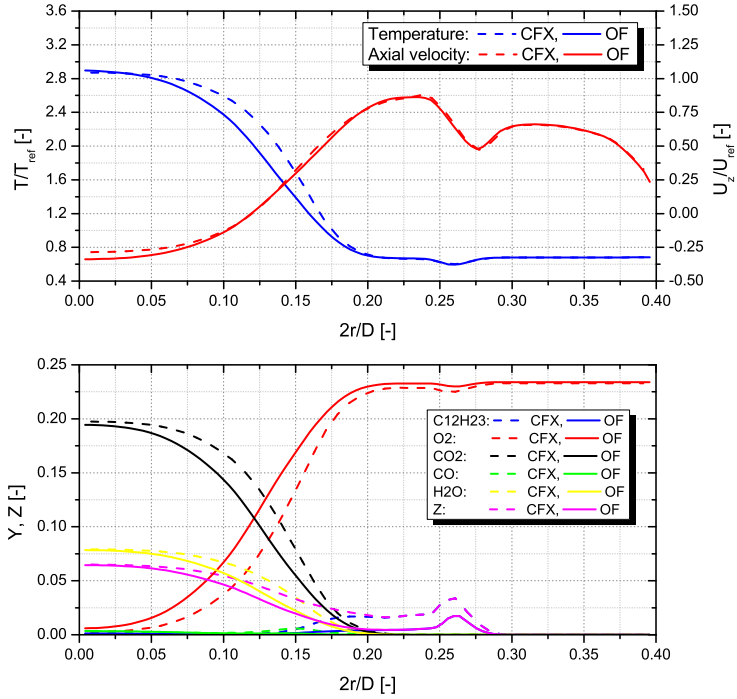

Figure 6.5: Radial profiles at Plane 1 (Case 1) - solution without film modelling.

flow rate injected by the airblast system. In this simulation these aspects cannot be caught and the parcels are simply rebounded by the walls. In Fig. 6.5 the present (OF) temperature, axial velocity and species mass fraction profiles at Plane 1 are compared with results obtained using the commercial code (CFX). The solver implemented in this work seems to predict slightly smaller evaporation rates as suggested by the lower values of fuel mass fraction and mixture fraction. Although the models used in the two codes are equivalent, different implementation strategies could lead to the aforementioned differences. Several factors could contribute in determining different evaporation rates: heat transfer modelling between particles and

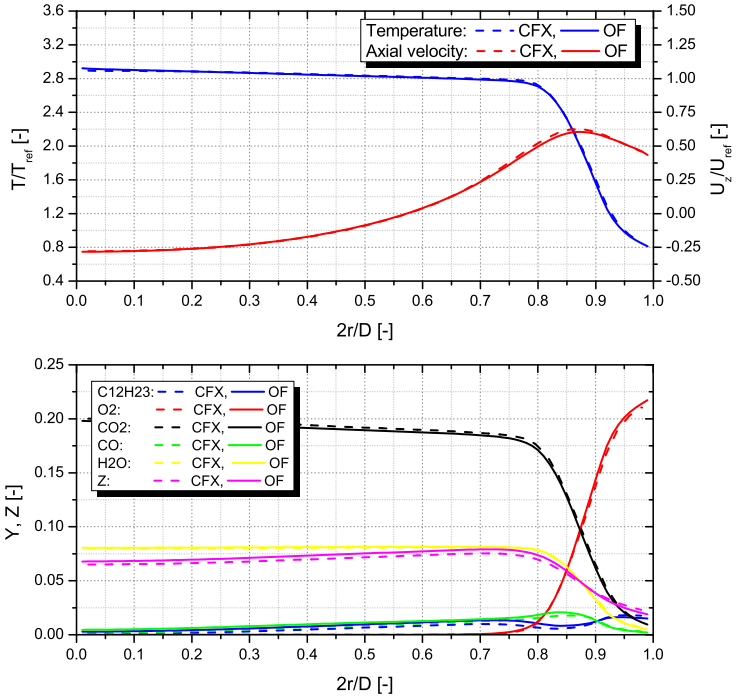

Figure 6.6: Radial profiles at Plane 2 (Case 1) - solution without film modelling.

gas-phase, the secondary breakup model which influences the droplet diameter, the drag model which alters the particle velocity influencing both the heat transfer and the secondary breakup, the physical properties of the fuel. Furthermore, the criteria used for parcel extinction can also play an important role in the prediction of liquid evaporation. Numerical results at Plane 2, reported in Fig. 6.6, show a general good agreement between the two codes. The small differences in species mass fractions can be ascribed to the different parcel evaporation histories with the commercial code that predicts slightly higher fuel concentrations near the flame tube walls since much more fuel in transported by the swirled air flow structures.

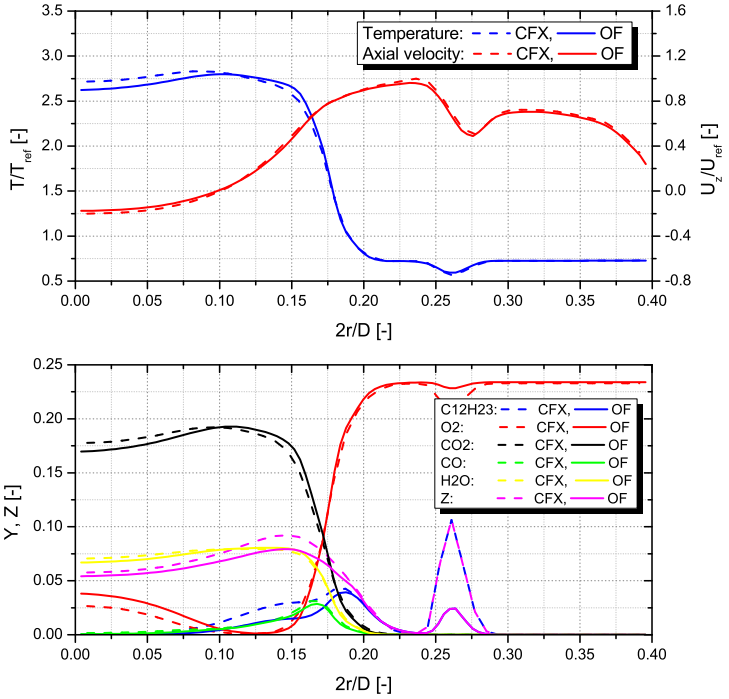

Figure 6.7: Radial profiles at Plane 1 (Case 2) - solution without film modelling.

6.3.2.2 Case 2 and 3

Results obtained for Case 2 are reported in Figs. 6.7 and 6.8. Because of the higher inlet temperature and the smaller droplet SMD (see Table 6.2), the fuel fully evaporates much closer to the injection system and no parcels reach the prefilming surface (see Fig. 6.4(b)). As a result, the mixture fraction predicted at Plane 1 is higher than one predicted in the previous case. Similar considerations can be drawn for Case 3. The very small SMD values of injected parcels, together with the higher inlet temperature, leads to a rapid evaporation, very

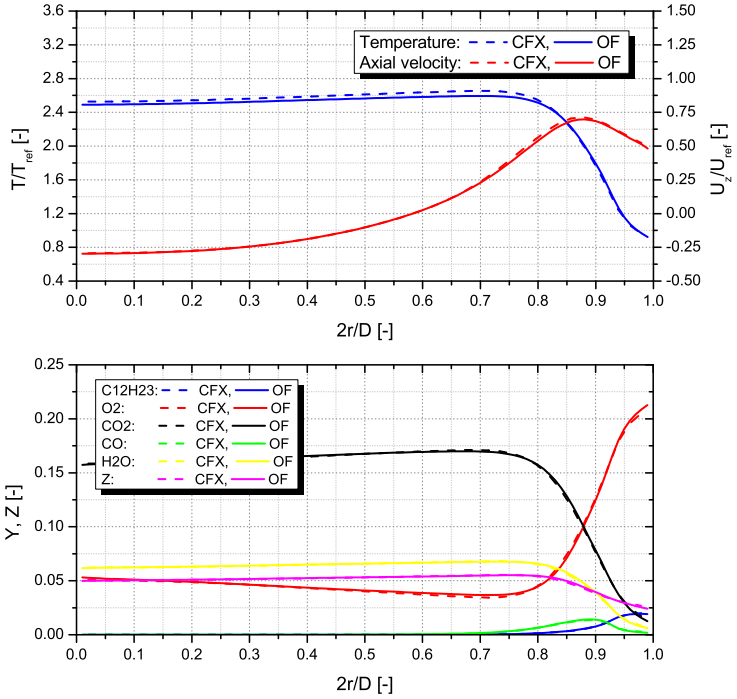

Figure 6.8: Radial profiles at Plane 2 (Case 2) - solution without film modelling.

close to the injection location, and also in this case there is no interaction between droplets and prefilming surface. Figs. 6.9 and 6.10 show the radial profiles at the two different sampling planes for Case 3. It is possible to note the high values of fuel mass fraction and mixture fraction at Plane 1 as a consequence of the very high droplet evaporation rate. A general good agreement between the results of the present solver and the ones obtained with the commercial code can be observed, especially at Plane 2. Also in this cases, the present solver predicts smaller droplet evaporation rates resulting in lower maximum values of fuel mass fraction near the injection system.

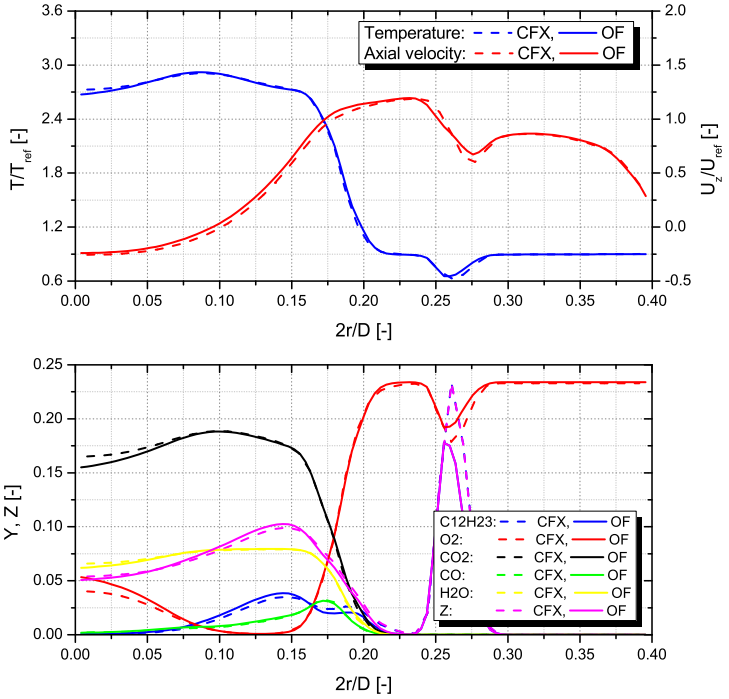

Figure 6.9: Radial profiles at Plane 1 (Case 3) - solution without film modelling.

6.3.3 Solution using the multi-coupled solver

In the multi-coupled approach proposed in this work, the liquid film over the prefilming surface is directly solved. Thus, it is possible to consider the interaction between droplets and liquid film which, as shown in the previous section, could be important especially in Case 1. Furthermore, the liquid film model allows us to impose a more reliable injection velocity for the droplets generated by the film primary breakup which could have important effects in the early stages of droplet evolution directly influencing drag forces and secondary breakup. In the following an analysis of the liquid film evolution is

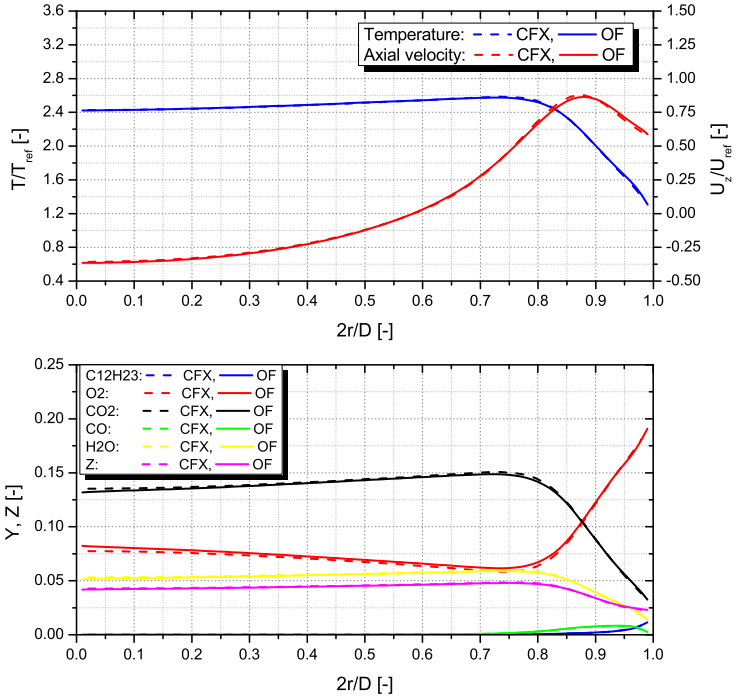

Figure 6.10: Radial profiles at Plane 2 (Case 3) - solution without film modelling.

firstly presented, then the results obtained with the multi-coupled approach are discussed.

6.3.3.1 Analysis of the liquid film evolution

The liquid fuel is supplied to the inner surface of the lip that separates the two swirlers through an array of holes with a high swirl component in order to cover the all surface and, thanks to the action of the air flow, it develops as a thin film until the atomizing edge is reached. Shear stresses acting on the liquid film surface due to the primary swirled flow give a tangential acceleration to the liquid

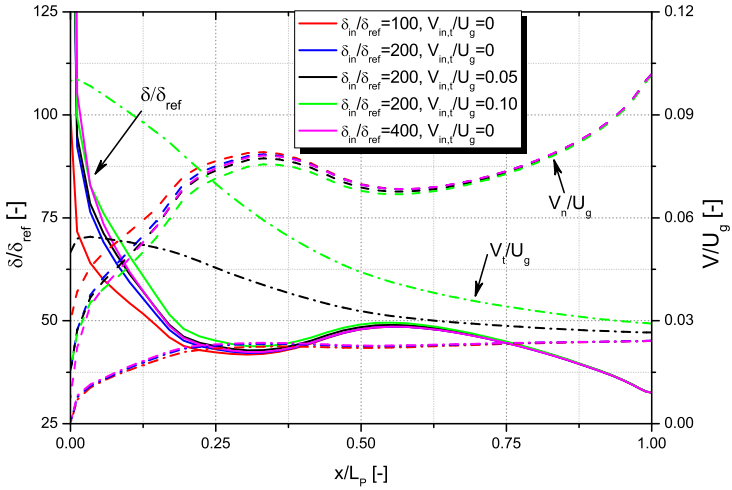

Figure 6.11: Film thickness and velocity along the prefilming surface (Case 2).

film determining a centrifugal force which pushes the liquid against the wall contributing to make the film more stable. In the numerical simulation the film has been injected uniformly along the circumference at the same location of the injection holes. However film inlet conditions are not known as well as the location at which the film can actually be considered uniform. Thus, before performing a fully-coupled numerical simulation of the combustor, a sensitivity analysis to the most important film inlet conditions was performed, with the same approach used in the preliminary analysis of film evolution presented in Section 4.3.3. Results concerning Case 2 are summarized in Fig. 6.11. The film thickness and the normal velocity component at the outlet boundary do not depend on boundary conditions assigned at the inlet (an asymptotic condition is reached). On the contrary, different tangential components imposed at the film inlet boundary lead to slightly different values of tangential velocity at the atomizing edge meaning that the prefilming surface is too short to allow a full

Table 6.3: Liquid film velocity at the film outlet boundary.

	Case 1	**Case 2**	**Case 3**
U_{inj}/U_g [-]	0.05	0.10	0.14
U_{inj}/U_{ref} [-]	0.04	0.10	0.17

development of the film swirl component. Therefore, great attention has to be devoted to the choice of the film tangential component at the inlet boundary. Similar considerations can be drawn for the other cases.

Table 6.3 summarizes the final film velocity of the three cases obtained considering a tangential inlet velocity equal to zero and without considering the possible contribution of droplets impinging the film and the stripping phenomenon (neglected in this work as discussed in Section 5.3). As shown in the experiments by Gepperth et al. [133] the initial velocity of droplets generated by film primary breakup falls between U_{inj}/U_g=0.02 and U_{inj}/U_g=0.2, thus the liquid film velocity at the outlet boundary could be reasonably taken as the droplet injection velocity. Furthermore, it is possible to note that the injection velocity imposed in the previous simulations is reached only in Case 3.

The liquid film solution is also exploited by the theoretical models used to compute the SMD of the droplets generated by the liquid film primary breakup. Table 6.4 summarizes the SMD predicted by different models and correlations considered in this work. First of all it should be noted that the SMD predicted by the Gepperth et al. correlation is quite larger than the value computed using the industrial correlation. This result does not surprize since, as shown in reference [73] and as explained in Section 5.2.2.1, the correlation by Gepperth et al. was developed using measurements performed very close to the atomizing edge avoiding the effects of secondary breakup which otherwise are included in the correlation. However, it should be noted that the range of calibration of the correlation is quite far from the operating conditions of the investigated cases (in terms of pressure, temperature, film load and geometrical configuration). Thus, before giving general conclusions much more investigations are needed even

Table 6.4: SMD [μm] predicted by different theoretical models and correlations.

	Case 1	**Case 2**	**Case 3**
Industrial correlation	52	28	20
Gepperth et al. [73] correlation	76	42	34
Dombrowski and Johns [59] model	34	24	19
Modified Senecal et al. model	120	75	59
Chaussonnet et al. [8] model	46	29	24
Inamura et al. [128] model	134	83	66

if the trend described here could be representative. The mean diameter predicted by the Dombrowski and Johns model is very similar to the one computed using the industrial correlation (especially in Case 2 and Case 3) as well as the one obtained using the model by Chaussonnet et al. [8]. The SMD predicted by the modified version of the Senecal et al. model [60] is in very good agreement with the values predicted using the model by Inamura et al. [128]. These values are quite larger if compared to the other formulations, with the same trend observed in the test case used for the assessment and validation of the primary breakup model (see Section 5.4). However, in an Eulerian-Lagrangian code injected droplets are usually immediately subjected to secondary atomization allowing proper SMD values to be recovered at the downstream location. If not differently specified, results presented in the following have been obtained using the modified version of the Senecal et al. model (with secondary atomization described by means of the TAB model [102]).

6.3.3.2 Case 1

As described above, in this case the droplets injected by the pilot injector impact the liquid film. The multi-coupled approach proposed in this work allows us to better describe the dynamics of droplets impinging the liquid film. Fig. 6.12 shows the path followed by the parcels together with the fuel mass fraction field. Droplets characterized by higher impact energy are subjected to splashing and thus

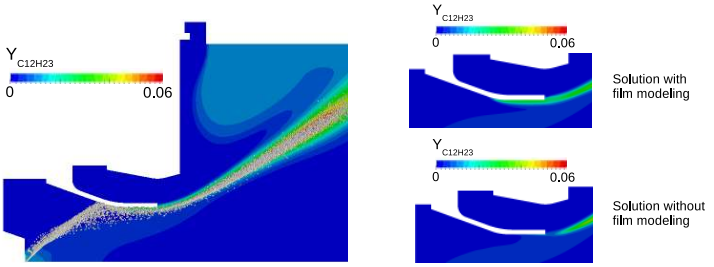

(a) Droplet dynamics (b) Fuel mass fraction near the film

Figure 6.12: Multi-coupled solution (Case 1).

disintegrate into droplets of smaller diameter as they impact the liquid film. These droplets rapidly evaporate causing an increase of fuel mass fraction near the liquid film interface which is convected downstream (the fuel directly evaporated from the prefilming surface is negligible). On the contrary, the droplets characterized by small impact energy are adsorbed by the liquid film (spread regime [68]) contributing to enhance the fuel mass flow rate injected through the liquid film primary breakup model (in this particular case about 70% of pilot fuel is added to the liquid film). The spray dynamics is very different from the one obtained without considering the liquid film model (see Fig. 6.4(a)) and this has a great impact on both species mass fraction and temperature profiles. Fig. 6.13 shows the radial profiles near the atomizer exit. The multi-coupled solution is characterized by higher values of fuel mass fraction near the atomizing edge compared to the simulation performed without film modeling. This higher fuel concentration is mainly due to the evaporation of small droplets near the film surface generated by the splashing of pilot fuel with the additional contribution due the evaporation of parcels injected from the liquid film which are characterized by an enhanced mass flow rate. However the effect of the increased mass flow rate is mitigated by the higher SMD which slows down the evaporation process resulting in a relatively smaller enhancement of the fuel mass fraction. Furthermore, the effect of the secondary breakup model should also be considered. The higher SMD together with

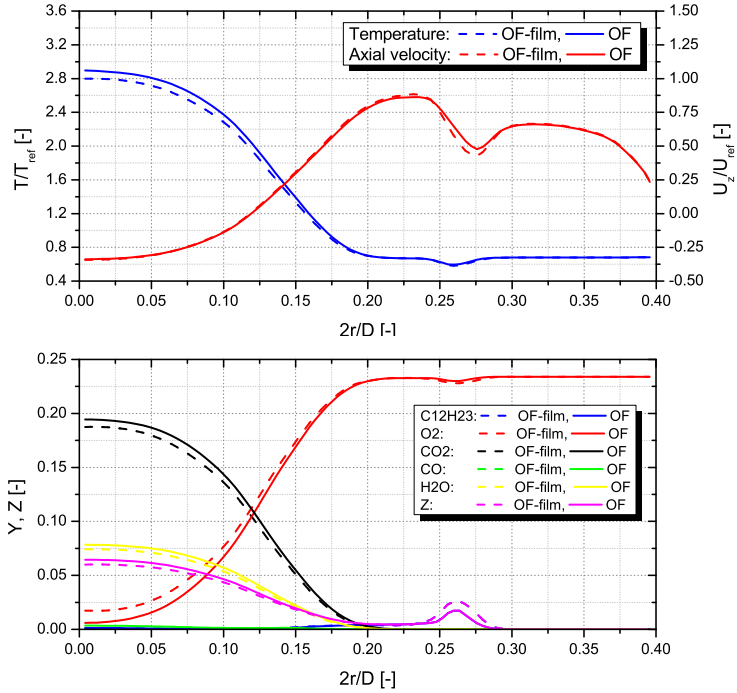

Figure 6.13: Radial profiles at Plane 1 (Case 1).

the lower injection velocity (and thus a greater relative velocity between particles and gas-phase) lead to higher droplet Weber numbers and therefore to relatively smaller droplet diameters after breakup reducing in the downstream region the impact of the higher SMD of injected parcels. As far as the temperature field is concerned, the values near the pilot injector are smaller than the ones predicted without the film model whereas in the downstream region (see Fig. 6.14) temperatures and species mass fraction profiles predicted in the two simulations are very similar to each other.

Fig. 6.15, which shows a comparison between evaporation sources obtained with the multi-coupled solver using different models for the SMD computation, allows us to explain the influence of the liquid

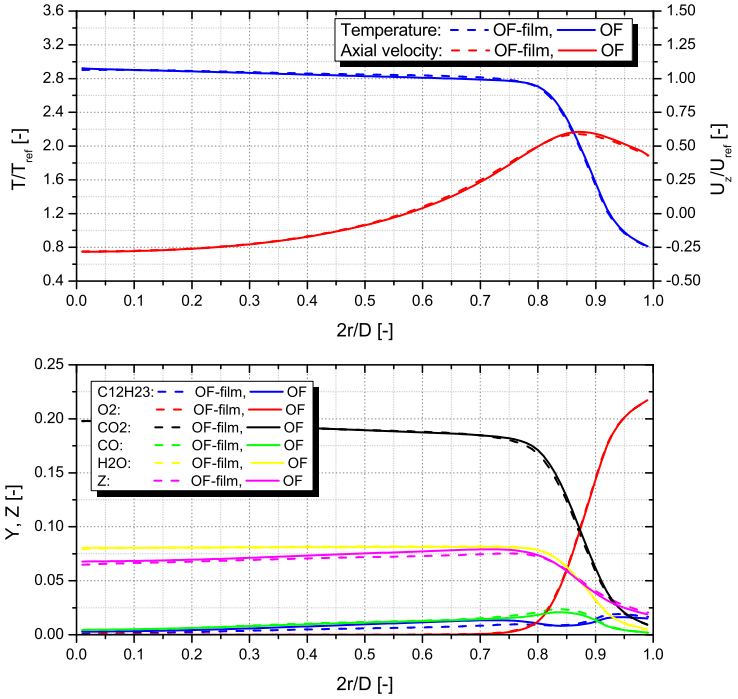

Figure 6.14: Radial profiles at Plane 2 (Case 1).

film primary breakup model. Because of the higher value of the mean diameter of the injected parcels (see Table 6.4), the simulation performed using the modified Senecal et al. model predicts lower evaporation sources compared to the results obtained with the model by Dombrowski and Johns. Furthermore, in the same figure, it is also possible to note the high value of evaporation rates near the liquid film where droplet splashing causes the formation of small droplets that rapidly evaporate.

Another aspect that should be considered with great attention is the injection location of droplet generated by the liquid film primary breakup. As a common practice these droplets were injected near the surface where the film develops and basically all the droplets are car-

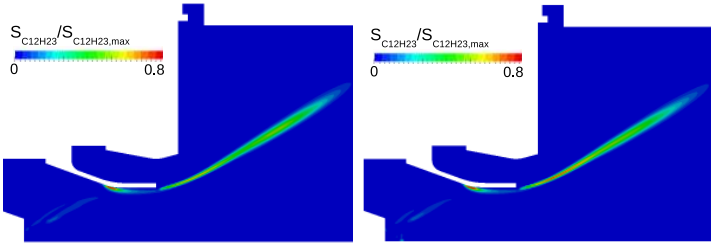

(a) Modified Senecal et al. model. (b) Dombrowski and Johns model.

Figure 6.15: Evaporation sources (Case 1).

ried away by the primary swirler flow. This is the strategy used in the simulations presented above. However, as a consequence of the liquid film accumulation at the atomizing edge and more in general of the action exerted by the secondary air flow, droplets could also be torn off by the secondary swirler flow. As also described in Section 5.2.1, a possible strategy to take this effect into account could be to inject the parcels in front of the atomizing edge using a proper spreading angle. However, in RANS simulations with the Lagrangian phase considered dispersed, the flow field in front of the atomizing edge is characterized by very low velocities (a wake like structure is formed) which do not lead to representative aerodynamic interactions between injected parcels and gas-phase, highly affecting droplet evolution and secondary breakup after injection. Another possibility could be to split the injection into two different locations corresponding to the upper and lower surfaces of the injector lip. Fig. 6.16 shows the fuel mass fraction field obtained using such injection strategies (note that in order to better visualize the fuel mass fraction a very small number of parcels was used in the visualization, however the droplet dynamics near the prefilming surface is very similar to the one reported in Fig. 6.12). Because of the very low values of gas-phase velocity, droplets injected in front of the atomizing edge are weakly subjected to the secondary breakup and thus the evaporation rate near the lip is much smaller. In the other case, parcels are equally split between the two injection locations: a large amount of fuel is trapped in the corner vortex leading to the formation of a more homogeneous air-

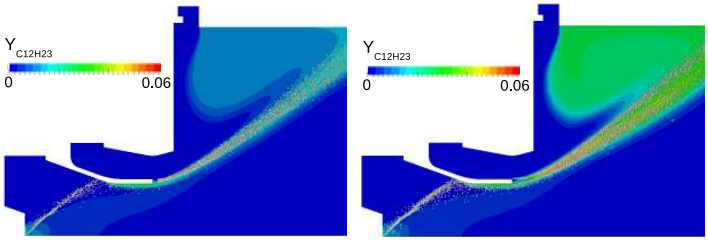

(a) Injection in front of the atomizing edge.

(b) Split injection.

Figure 6.16: Comparison between different injection strategies.

fuel mixture and lower temperatures in the flame region. Further experimental investigations or detailed numerical simulations are required to understand what could be the most representative injection pattern and split of parcels between the primary and secondary flows. A configuration close to the real injectors should be used in order to include the effects of atomizing edge curvature.

6.3.3.3 Case 2 and 3

In both these cases, droplets injected by the pilot atomizer do not reach the liquid film, thus the main contribution of the liquid film modeling is related to film evaporation and film primary breakup model which allows us to impose more consistent injection velocity and mean diameter to the parcels injected at the atomizing edge. Fig. 6.17 shows mass fraction, temperature and axial velocity radial profiles at the injector exit for Case 3. The droplets generated by the liquid film primary breakup are characterized by higher SMD values compared to the simulation without film solver leading to a lower evaporation rate near the injector exit and thus to smaller fuel mass fractions. As a consequence the air-fuel mixing is completed farther away from the atomizing edge. Furthermore, the slightly different values of fuel mass fraction near the combustor axis are mainly due to changes in the velocity field caused by the different boundary condition for the gas-phase on the prefilming surface (no slip condition in the simulation without film, liquid film velocity in the multi-coupled

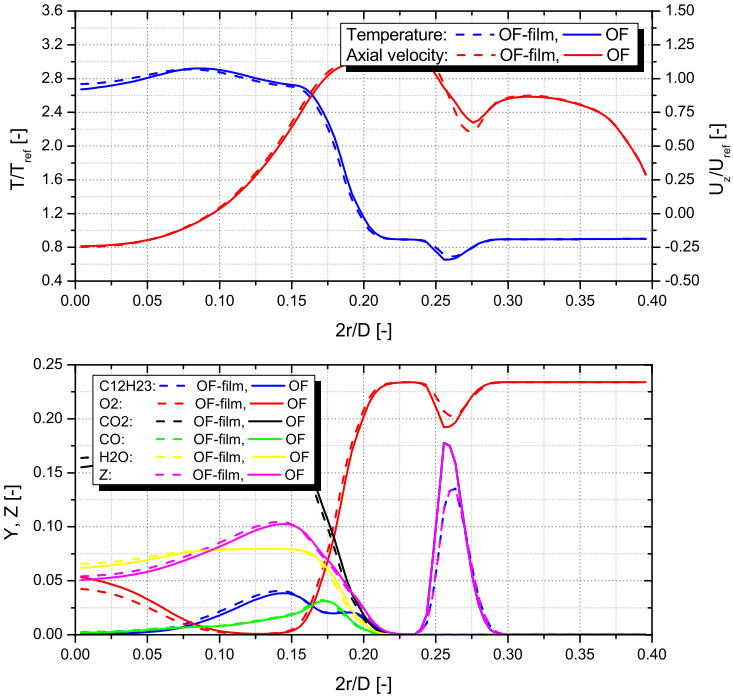

Figure 6.17: Radial profiles at Plane 1 (Case 3).

solution).

6.4 Concluding remarks

The multi-coupled approach developed in this research has been applied to the simulation of a tubular combustor equipped with a PERM injection system with the main aim of showing the improvements that can be obtained in the description of liquid fuel preparation through the introduction of liquid film modelling. The main advantages of the proposed approach, compared to standard industrial approaches where the presence of the liquid film is neglected and droplets generated by the liquid film primary breakup are introduced with an

equivalent injector placed at the atomizing edge, can be summarized as follows:

- interaction between droplets and liquid film can be included in the simulation and thus important physical phenomena such as droplet adsorption or splashing can be considered in the simulation.

- Fuel mass flow rate of droplets generated by liquid film primary breakup directly derives from the liquid film solution. Thus it is possible to consider the mass flow rate enhancement due to droplet adsorption.

- Interactions between liquid film and gas-phase are taken into account. Therefore, it is possible to compute fuel evaporation and heat transfer along the prefilming surface resulting in more accurate boundary conditions for the droplets injected through the liquid film primary breakup model.

- The primary breakup model offers a strategy to determine spray characteristics without requiring a user-definition of the most important parameters. However, the reliability of the assigned parameters depends on the accuracy of correlations and theoretical models used in the primary breakup model for the computation of droplet diameter.

The aspects related to combustion and chemistry modeling still remain important issues for a correct prediction of species and temperature fields. However, the phenomena related to liquid fuel preparation and evolution cannot be neglected as they influence the entire combustion process. As shown in this work, a more comprehensive description of fuel preparation, including liquid film primary breakup and interaction between liquid film and droplets, leads to different droplet dynamics resulting in non-negligible variations of the temperature field which is fundamental for NO_x emission predictions. Some improvements to the model are still necessary. In particular, an important issue that has to be considered in the future is the injection location of parcels generated by the liquid film since it could strongly affect the fuel distribution inside the combustor leading to

significantly different temperature fields. Furthermore all the developed models should be exploited in unsteady simulations with advanced combustion models able to better describe the droplet and combustion dynamics in swirl-stabilized spray flames.

Chapter 7

Conclusions

The liquid fuel preparation has a strong impact on the combustion process and engine emissions since it directly influences the air-fuel mixing and the fuel distribution inside the combustion chamber. Therefore, in order to properly predict the behaviour of aero-engine combustors, great attention has to be devoted to the description of the most important aspects related to fuel evolution and interactions with the gas-phase. This research activity was carried out with the main aim of developing numerical tools for the analysis of advanced prefilming airblast injectors to be used in standard industrial computations based on RANS (U-RANS) approaches. Prefilming airblast injector configurations are characterized by the presence of a liquid film which is spread out along a prefilming surface and evolves under the action of the gas-phase until the atomizing edge is reached and primary atomization occurs. A reliable prediction of liquid fuel preparation and fuel distribution inside the combustor requires a proper description of the complex physical phenomena related to the interactions among liquid film, droplets and gas-phase. However, typical industrial computations usually neglect the presence of the liquid film resulting in a poor description of liquid fuel preparation. Thus, in this research, great attention was devoted to the aspects related to the film evolution and primary breakup developing proper tools able to include liquid film modelling in industrial computations. It is important to underline that in this research both theoretical and numerical aspects related to the physical phenomena involved in liquid fuel preparation were deeply investigated with an equal contribution

to the development of the proposed approach.

In this chapter the main achievements of this research will be summarized and final conclusions to the work carried out will be given underlining the significant results but also the limits of the developed approach in order to suggest possible directions for future research and applications.

7.1 Main achievements

In this work, a multi-coupled numerical solver able to handle liquid film evolution and primary breakup as well as droplet-film interactions for RANS (U-RANS) calculations was developed in the framework of OpenFOAM starting from models implemented in the Version 2.0. In order to make the developed approach suitable to be used in an industrial design context, numerical approaches able to guarantee a good compromise between computational cost and accuracy in the physical representation of the involved phenomena were selected. Spray evolution was modelled using an Eulerian-Lagrangian approach where the gas-phase is solved in an Eulerian framework while droplets are tracked in the domain using a Lagrangian description. Since in many industrial applications the interest is on time-averaged quantities, a steady-state Eulerian-Lagrangian solver for reacting dilute sprays was implemented and validated using literature test-cases with detailed experimental measurements. Models for the description of interactions between spray and gas-phase were updated implementing recent models and formulations. Spray evaporation and secondary breakup were considered with great attention and different models were assessed and compared with each other. Then, the spray solver was integrated with a film solver based on the thin film approximation with proper models for the description of droplet-film interactions and primary breakup. The capabilities of the film solver to describe film evolution in typical prefilming airblast configurations were assessed and validated using literature test cases representing the most important interactions between gas-phase and liquid film characterizing typical industrial injectors. As far as primary atomization of liquid film is concerned, a completely new model was introduced in the code. The model is basically a phenomeno-

logical approach which exploits correlations and theoretical models for the computation of droplet characteristics after primary breakup starting from liquid film and gas-phase solutions. Several theoretical models were revised considering recent experimental findings on prefilming airblast injectors. Furthermore, different strategies for particle injection were proposed and evaluated. The primary breakup model was assessed using experiments performed with a PERM injection system at ambient conditions using water. It should be noted that all the developed tools for the description of liquid fuel preparation and spray dynamics were also integrated with the unsteady spray solver already implemented in the base version of the code. Finally, the developed approach was applied to the simulation of a PERM injection system in a tubular combustor configuration with the main aim of analysing ad showing the improvements that can be obtained in the description of liquid fuel preparation in comparison with standard approaches which neglect the presence of the liquid film.

In order to better explain the contributions of the present research, it could be useful to give a picture before and after this work of the approaches used in industrial computations for the analysis of lean burn aero-engine combustors equipped with advanced prefilming airblast injectors.

Before this research...

Typical industrial computations of prefilming airblast injection systems performed using standard RANS (U-RANS) approaches usually neglect the presence of the liquid film and its possible formation due to the interaction between droplets and solid walls. Primary atomization of liquid film is not included in the numerical solver and droplets generated by the liquid film primary breakup are simply introduced in the computational domain by means of an equivalent injector placed at the atomizing edge of the airblast system. The characteristics of droplets generated by the liquid film atomization are imposed by the user and do not depend on the liquid film evolution over the prefilming surface disregarding, for example, changes in temperature due to heat transfer with the gas-phase and solid walls as well as liquid film pre-vaporization which could alter the fuel mass fraction distribution

near the injection system. Furthermore, interactions between liquid film and droplets are not considered and therefore it is not possible to compute the increase of film mass flow rate due to droplet adsorption or the detachment of droplets due to splashing phenomena.

After this research...

A multi-coupled approach which includes liquid film evolution and primary breakup suitable for industrial computations has been developed allowing us to include in the numerical simulation the most important interactions among liquid film, droplets and gas-phase. Therefore, important phenomena for liquid fuel preparation, such as film evaporation, heat transfer between liquid film and gas-phase and liquid film mass flow rate enhancement due to droplet adsorption, can be considered in the simulation of the injection system. Furthermore, the primary breakup model for liquid films introduced in the formulation allows us to assign more reliable characteristics to the droplet population generated by the film breakup exploiting the liquid film solution and correlations or theoretical models for the computation of the main parameters of the injected droplets.

7.2 Conclusions and recommendations for future research

Advanced airblast injectors are characterized by many complex physical processes and for a reliable prediction of fuel preparation the aspects related to liquid film evolution, primary breakup and interactions of the liquid film with both gas-phase and droplets cannot be neglected. Validation with experimental test cases and application to the simulation of a real combustor have shown that the multi-coupled approach developed in this work allows a better representation of the physical phenomena regulating the behaviour of advanced injection systems based on prefilming airblast configurations with a relatively low computational cost which makes the proposed tools suitable for industrial design applications. The proposed approach has several advantages compared to classical industrial approaches which neglect the presence of liquid film, especially in the case droplets impinge the

liquid film. Phenomena related to the interaction between droplets and liquid film as well as interactions between liquid film and gas-phase can be included in the simulation resulting in an more physically consistent prediction of fuel distribution in the injector region.

The model for the primary breakup of the liquid film introduced in the numerical solver allows a more reliable prediction of the characteristics of droplets generated by liquid film atomization. The assessment of the developed model, performed through the simulation of a PERM injector, showed the consistency of the approach even if the success of a simulation is related to a proper choice of the model or correlation used to compute the diameter of particles generated by the film breakup. More basic research from both experimental and theoretical points of view should be done in the future for a more comprehensive understanding of the phenomena involved in primary atomization, especially in configurations close to real atomizers where the curvature of the atomizing edge as well as the presence of swirled flows could play an important role in determining the droplet size. Anyway, the proposed approach allows new models and correlations to be easily introduced in the code and thus it is ready to exploit all the results that will be achieved in the future.

Validation and application of the developed model also allowed us to highlight some limits of typical RANS simulations used in industrial computations which could affect fuel distribution inside the combustion chamber. Industrial computations of aero-engine combustors are often performed using steady-state acceleration techniques because of their low computational cost which allows designers to have useful indications in a very short time. Although steady-state approaches are usually able to predict the correct trend of the combustor behaviour, for example at different operating conditions, many physical processes that regulate the spray dynamics, such as the droplet spreading due to velocity fluctuations, are characterized by a strong coupling with the turbulent field and only unsteady simulations can give a physically consistent representation of the fuel distribution inside the combustion chamber and thus a more reliable prediction of the combustion process and pollutant emissions. With the increase in performance of computer resources, in the next future unsteady simulations are expected to be extensively used also in the industrial design process. Therefore, in the future research, attention has to be

moved on to advanced time-resolved approaches able to better describe liquid and gas-phase dynamics. However, it should be noted that advanced numerical tools such as LES, which in principle could give a more accurate solution of gas-phase and flame dynamics, are still far from application in an industrial design context and more academic research is necessary in order to develop models capable of properly representing physical phenomena in configurations of industrial interest.

As far as the numerical simulation of liquid films is concerned, in the future more attention has to be devoted to numerical methods able to resolve the interface between liquid film and gas-phase. VOF and level-set methods, already used in academic configurations, should also be exploited in industrial cases. The main limitations are due to the high mesh resolution (and consequently the high computational cost) required to limit numerical diffusion and to catch the small flow structures along the interface. Such methods, in principle, are able to resolve the unstable structures developing along the liquid surface leading to a better prediction of momentum exchanges between film and gas-phase. Furthermore, these methods also allow the resolution of the unstable phenomena regulating the primary atomization and thus they can be used as predictive tools for the study of liquid film breakup. Spatial resolution of numerical simulations could overcome the resolution of experimental techniques and simulations could give an important contribution in the understanding of the physics regulating droplet formation. To some extent, simulations could substitute experiments in the prediction of droplet characteristics after breakup and, from this point of view, results obtained in these simulations could also be exploited in the numerical approach developed in this work giving the characteristics of parcels to be injected through the model for liquid film primary breakup.

...queste poche pagine
non bastano a descrivere
gli sforzi fatti in questi anni,

spero però che da queste righe
sia trasparso tutto l'entusiasmo
che mi ha accompagnato
e che vorrei sempre con me.

Grazie.

Bibliography

[1] Blazowski, W. S., 1978. "Future jet fuel combustion problems and requirements". *Prog. Energy Combust. Sci.,* ***4***, pp. 177–199.

[2] Andreini, A., Facchini, B., Giusti, A., Vitale, I., and Turrini, F., 2013. "Thermoacoustic analysis of a full annular lean burn aeroengine combustor". *Proceedings of the ASME Turbo Expo 2013*(GT2013-94877).

[3] Andreini, A., Facchini, B., Giusti, A., Vitale, I., and Turrini, F., 2013. "Thermoacoustic analysis of a full annular aero-engine lean combustor with multi-perforated liners". *Proceedings of the AIAA-CEAS conference.*

[4] Andreini, A., Facchini, B., Giusti, A., and Turrini, F., 2014. "Assessment of flame transfer function formulations for the thermoacoustic analysis of lean burn aero-engine combustors". *Energy Procedia,* ***45***, pp. 1422 – 1431.

[5] Andreini, A., Facchini, B., Giusti, A., Turrini, F., and Vitale, I., 2012. "Thermo-acoustic analysis of an advanced lean injection system in a tubular combustor configuration". *Proceedings of the 2012 COMSOL European Conference, Milan 10-12 October 2012.*

[6] Advisory Council for Aeronautics Research in Europe, 2010. *Aeronautics and Air Transport: Beyond Vision 2020 (towards 2050): Background Document.* Studies and reports / European Commission, European Research Area, Transport. Europ. Comm. Directorate-General for Research Aeronautics and Air Transport.

[7] Schober, P., Ebner, J., Shäfer, O., and Wittig, S., 2003. "Experimental Study on the Effect of a Strong Negative Pressure Gradient on a Shear-driven Liquid Fuel Film". *Proceeding of the ICLASS03*.

[8] Chaussonnet, G., Riber, E., Vermorel, O., Cuenot, B., Gepperth, S., and Koch, R., 2013. "Large Eddy Simulation of a prefilming airblast atomizer". *Proceedings of the ILASS-Europe 2013*.

[9] Andreini, A., Bianchini, C., Facchini, B., Giusti, A., and Turrini, F., 2013. "A multi-coupled Eulerian-Lagrangian solver for airblast injectors including liquid film evolution and primary breakup - Application". *Proceedings of the ILASS-Europe 2013*.

[10] Jenny, P., Roekaerts, D., and Beishuizen, N., 2012. "Modeling of turbulent dilute spray combustion". *Progress in Energy and Combustion Science,* ***38***, pp. 846–887.

[11] Doerr, T., 2012. "Introduction to aero-engine gas turbine combustion". In *Combustion in aero-engines*, Lecture Series 2012-04. von Karman Institute for Fluid Dynamics.

[12] Sankaran, V., and Menon, S., 2002. "Turbulence-chemistry interactions in spray combustion". *Proceedings of the ASME Turbo Expo 2002*(GT-2002-30091).

[13] Carrotte, J., 2012. "Aerodynamics, unsteadiness and mixing". In *Combustion in aero-engines*, Lecture Series 2012-04. von Karman Institute for Fluid Dynamics.

[14] Senoner, J. M., Sanjosé, M., Lederlin, T., Jaegle, F., Garcia, M., Riber, E., Cuenot, B., Giquel, L., Pitsch, H., and Poinsot, T., 2009. "Eulerian and Lagrangian Large Eddy Simulations of an evaporating two-phase flow". *C. R. Mecanique,* ***337***, pp. 458–468.

[15] Jaegle, F., J.-M. Senoner, Garcia, M., Bismes, F., Lecourt, R., Cuenot, B., and Poinsot, T., 2011. "Eulerian and Lagrangian spray simulations of an aeronautical multipoint injector". *Proceedings of the Combustion Institute,* ***33***, pp. 2099–2107.

[16] Faeth, G. M., 1983. "Evaporation and combustion of sprays". *Prog. Energy Combustion Science,* ***9***, pp. 1–76.

[17] Chrigui, M., Sadiki, A., Batarseh, F. Z., Roisman, I., and Tropea, C., 2008. "Numerical and experimental study of spray produced by an airblast atomizer under elevated pressure conditions". *Proceedings of the ASME Turbo Expo 2008*(GT2008-51305).

[18] Klose, G., Schmehl, R., Meier, R., Meier, G., Koch, R., Wittig, S., Hettel, M., Leuckel, W., and Zarzalis, N., 2000. "Evalutation of advanced two-phase flow and combustion models for predicting low emission combustors". *Proceedings of the ASME Turbo Expo 2000*(2000-GT-0133).

[19] Andreini, A., Ceccherini, A., Facchini, B., Turrini, F., and Vitale, I., 2009. "Assessment of a set of numerical tools for the design of aero-engines combustors: study of a tubular test rig". *Proceedings of the ASME Turbo Expo 2009*(GT2009-59539).

[20] Schmehl, R., Rosskamp, H., Willmann, M., and Wittig, S., 1999. "CFD analysis of spray propagation and evaporation including wall film formation and spray/film interactions". *International Journal of Heat and Fluid Flow,* ***20***, pp. 520–529.

[21] Bai, C. X., and Gosman, A. D., 1995. "Development of Methodology for Spray Impingement Simulation". *SAE Paper*(950283).

[22] Lebas, R., Menard, T., Beau, P. A., Berlemont, A., and Demoulin, F. X., 2009. "Numerical simulation of primary breakup and atomization: DNS and modelling study". *International Journal of Multiphase Flow,* ***35***, pp. 247–260.

[23] Fuster, D., Bagué, A., Boeck, T., Le Moyne, L., Leboissetier, A., Popinet, S., Ray, P., Scardovelli, R., and Zaleski, S., 2009. "Simulation of primary atomization with an octree adaptive mesh refinement and VOF method". *International Journal of Multiphase Flow,* ***35***, pp. 550–565.

[24] van Hinsberg, N. P., Budakli, M., Göhler, S., Berberović, E., Roisman, I. V., Gambaryan-Roisman, T., Tropea, C., and

Stephan, P., 2010. "Dynamics on the cavity and the surface film for impingement of single drops on liquid films of various thicknesses". *Journal of Colloid and Interface Science,* ***350***, pp. 336–343.

[25] Sauer, B., Spyrou, N., Sadiki, A., and Janicka, J., 2013. "Numerical Analysis of the Primary Breakup under High-Altitude Relight Conditions applying the embedded DNS (eDNS) Approach to a generic Prefilming Airblast Atomizer". *Proceedings of the ASME Turbo Expo 2013*(GT2013-94446).

[26] Bai, C., and Gosman, A. D., 1996. "Mathematical Modelling of Wall Films Formed by Impinging Sprays". *SAE Technical Papers*(960626).

[27] LEMCOTEC European Project, 2011. Description of work and internal reports. Confidential documents.

[28] Lefebvre, A. H., 1998. *GAS Turbine Combustion, Second Edition.* Taylor & Francis.

[29] Haselbach, F., and Parker, R., 2012. "Hot end technology for advanced, low emission large civil aircraft engines". *Proceedings of the ICAS 2012.*

[30] McKinney, R. G., Sepulveda, D., Sowa, W., and Cheung, A. K., 2007. "The Pratt & Whitney TALON X Low Emissions Combustor: Revolutionary Results with Evolutionary Technology". *Proceedings of the 45th AIAA Aerospace Sciences Meeting and Exhibit*(AIAA 2007-386).

[31] Lilley, D. G., 1977. "Swirl Flows in Combustion: A Review". *AIAA Journal,* ***15***(8), pp. 1063–1078.

[32] Lefebvre, A. H., 1988. *Atomization and Sprays.* Combustion (Hemisphere Publishing Corporation). Taylor & Francis.

[33] Lefebvre, A. H., 1980. "Airblast atomization". *Prog. Energy Combust. Sci.,* ***6***, pp. 233–261.

[34] Rizk, N. K., Chin, J. S., and Razdan, M. K., 1996. "Influence of design configuration on hybrid atomizer performance". *AIAA Paper*(96-2628).

[35] Batarseh, F. Z., Roisman, I. V., and Tropea, C., 2007. "Spray generated by an airblast atomizer at high-pressure conditions". *Proceedings of the ASME Turbo Expo 2007*(GT2007-27803).

[36] Li, X., Soteriou, M. C., Kim, W., Cohen, J., Herrmann, M., Ham, F., Kim, D., Le, H., and Spyropoulos, J. T., 2013. "High fidelity simulation of the spray generated by a realistic swirling flow injector". *Proceedings of the ASME Turbo Expo 2013*(GT2013-96000).

[37] Meier, U., Heinze, J., and Hassa, C., 2007. "Response of spray and heat release to forced air flow fluctuations in a gas turbine combustor at elevated pressure". *Proceedings of the ASME Turbo Expo 2007*(GT2007-27310).

[38] Ebner, J., Schober, P., Shäfer, O., Koch, R., and Wittig, S., 2004. "Modelling of shear-driven liquid films: effect of accelerated air flow on the film flow propagation". *Progress in Computational Fluid Dynamics,* ***4***(3–5), pp. 183–190.

[39] Hage, M., Dreizler, A., and Janicka, J., 2007. "Flow fields and droplet diameter distribution of water and n-heptane sprays at varied boundary conditions in a generic gas turbine combustor". *Proceedings of the ASME Turbo Expo 2007*(GT2007-27108).

[40] Buelow, P., Williams, B., Bretz, D., Spooner, M., Mohamed, C., and Gill, H., 2010. Lean direct injection atomizer for gas turbine engines, Aug. 24. US Patent 7,779,636.

[41] Meier, U., Freitag, S., Heinze, J., Lange, L., Magens, E., Schroll, M., Willert, C., Hassa, C., Bagchi, I. K., Lazik, W., and Whiteman, M., 2013. "Characterization of Lean Burn Module Air Blast Pilot Injector With Laser Techniques". *Journal of Engineering for Gas Turbines and Power,* ***135***.

[42] Mongia, H. C., 2003. "TAPS - A 4th Generation Propulsion Combustor Technology for Low Emissions". *Proceedings of*

AIAA/ICAS International Air and Space Symposium and Exposition(AIAA Paper 2003-2657).

[43] Li, S., Hsieh, S., Hsiao, G., and Mongia, H., 2010. Pilot mixer for mixer assembly of a gas turbine engine combustor having a primary fuel injector and a plurality of secondary fuel injection ports, July 27. US Patent 7,762,073.

[44] Hura, H., Sabla, P., Cooper, J., Duncan, B., Mongia, H., and Lohmueller, S., 2002. Fuel nozzle assembly for reduced exhaust emissions, May 21. US Patent 6,389,815.

[45] Foust, M., and Mongia, H., 2002. Method and apparatus for controlling combustor emissions, July 16. US Patent 6,418,726.

[46] Providakis, T., Zimmer, L., Scouflaire, P., and Ducruix, S., 2011. "Effect of fuel distribution on spray dynamics in a rwo-staged multi-injection burner". *Proceedings of the ASME Turbo Expo 2011*(GT2011-46519).

[47] Mawid, M. A., and Lee, F. P., 2012. "Development of a "SAWBLAST®" Fuel Nozzle Concept for Improved Fuel Atomization and Mixing in High Performance Gas Turbine Combustors: Part-I Conceptual Design". *Proceedings of the ASME Turbo Expo 2012*(GT2012-69897).

[48] Koch, R., 2011. "Spray combustion". In *Turbulent combustion*, Lecture Series 2011-03. von Karman Institute for Fluid Dynamics.

[49] Chrigui, M., 2005. "Eulerian-lagrangian approach for modeling and simulations of turbulent reactive multi-phase flows under gas turbine combustor conditions". PhD thesis, Technische Universität Darmstadt.

[50] Lavergne, G., 2012. "Fuel injection and spray evaporation". In *Combustion in aero-engines*, Lecture Series 2012-04. von Karman Institute for Fluid Dynamics.

[51] Kralj, C., 1995. "Numerical simulation of diesel spray processes". PhD thesis, Imperial College London.

[52] Dumouchel, C., 2005. "On the experimental investigation on primary atomization of liquid streams". *Exp Fluids,* ***45***, pp. 371–422.

[53] Rayleigh, L., 1878. "On the instability of jets". *Proceedings of London Mathematical Society,* ***10***, pp. 4–13.

[54] Reitz, R. D., 1978. "Atomization and other breakup regimes of a liquid jet". PhD thesis, Princeton University.

[55] Marmottant, P. H., and Villermaux, E., 2004. "On spray formation". *Journal of Fluid Mechanics,* ***498***, pp. 73–111.

[56] Carvalho, I. S., Heitoyr, M. V., and Santos, D., 2002. "Liqud film disintegration regimes and proposed correlations". *International Journal of Multiphase Flow,* ***28***, pp. 773–789.

[57] Sirignano, W. A., and Mehring, C., 2000. "Review of theory of distortion and disintegration of liquid streams". *Progress in Energy and Combustion Science,* ***26***, pp. 609–655.

[58] Ashgriz, N., Li, X., and Sarchami, A., 2011. "Instability of liquid sheets". In *Handbook of Atomization and Sprays*. Springer.

[59] Dombrowski, N., and Johns, W. R., 1963. "The aerodynamic instability and disintegration of viscous liquid sheets". *Chemical Engineering Science,* ***18***, pp. 203–214.

[60] Senecal, P. K., Schmidt, D. P., Nouar, I., Rutland, C. J., Reitz, R. D., and Corradini, M. L., 1999. "Modeling high-speed viscous liquid sheet atomization". *International Journal of Multiphase Flow,* ***25***, pp. 1073–1097.

[61] Ashgriz, N., and Yarin, A. L., 2011. "Capillary instability of free liquid jets". In *Handbook of Atomization and Sprays*. Springer.

[62] Guildenbecher, D. R., Lopez-Rivera, C., and Sojka, P. E., 2009. "Secondary atomization". *Exp Fluids,* ***46***, pp. 371–402.

[63] Brodkey, R. O., 1967. *The Phenomena of fluid Motion*. Addison-Wesley, Reading, MA.

[64] Hinze, J. O., 1955. "Fundamentals of the Hydrodynamic Mechanism of Splitting in Dispersion Process". *AIChE J.,* ***1***(3), pp. 289–295.

[65] Prevish, T. D., and Santavicca, D. A., 1998. "Turbulent breakup of hydrocarbon droplets at elevated pressures". *Proceedings of the ILASS-Americas 1998.*

[66] Moreira, A. L. N., Moita, A. S., and Panão, M. R., 2010. "Advances and challenges in explaining fuel spray impingement: How much of single droplet impact research is useful?". *Progress in Energy and Combustion Science,* ***36***, pp. 554–580.

[67] Buckingham, E., 1915. "Model experiments and the forms of empirical equations". *Transactions of the American Society of Mechanical Engineers,* ***37***, pp. 263–296.

[68] Bai, C. X., Rusche, H., and Gosman, A. D., 2002. "Modeling of Gasoline Spray Impingement". *Atomization and Sprays,* ***12***, pp. 1–27.

[69] Rioboo, R., Tropea, C., and Marengo, M., 2001. "Outcomes from a drop impact on solid surfaces". *Atomization and Sprays,* ***11***, pp. 155–165.

[70] Tropea, C., and Marengo, M., 1999. "The impact of drops on walls and films". *Multi Sci. Tech.,* ***11***(1), pp. 19–36.

[71] Yarin, A. L., 2006. "Drop Impact Dynamics: Splashing, Spreading, Receding, Bouncing ...". *Annu. Rev. Fluid Mech.,* ***38***, pp. 159–192.

[72] Rosin, P., and Rammler, E., 1933. "The Laws Governing the Fineness of Powdered Coal". *J. Inst. Fuel.,* ***7***(31), pp. 29–36.

[73] Gepperth, S., Koch, R., and Bauer, H. J., 2013. "Analysis and comparison of primary droplet characteristics in the near field of a prefilming airblast atomizer". *Proceedings of the ASME Turbo Expo 2013*(GT2013-94033).

[74] Liu, B., Mather, D., and Reitz, R. D., 1993. "Effects of Drop Drag and Breakup on Fuel Sprays". *SAE Technical Paper*(930072).

[75] Hoefler, C., Braun, S., Koch, R., and Bauer, H., 2012. "Modeling spray formation in gas turbines - a new meshless approach". *Proceedings of the ASME Turbo Expo 2012*(GT2012-68489).

[76] Braun, S., Hoefler, C., Koch, R., and Bauer, H., 2013. "Modeling fuel injection in gas turbines using the meshless Smoothed Particle Hydrodynamics method". *Proceedings of the ASME Turbo Expo 2013*(GT2013-94027).

[77] Vallet, A., Burluka, A. A., and Borghi, R., 2001. "Development of a Eulerian model for the "Atomization" of a liquid jet". *Atomization and Sprays,* ***11***(6), pp. 619–642.

[78] Andreini, A., Bianchini, C., Facchini, B., and Giusti, A., 2012. "A steady-state Eulerian-Lagrangian solver for non-reactive sprays". *Proceedings of the ICLASS 2012*.

[79] Ferziger, J. H., and Perić, M., 2002. *Computational Methods for Fluid Dynamics*, third ed. Springer.

[80] Hansell, D., Kennedy, I. M., and Kollmann, W., 1992. "A simulation of particle dispersion in a turbulent jet". *Int. Journal of Multiphase Flow,* ***18***(4), pp. 559–576.

[81] Gosman, A. D., and Ioannides, E., 1983. "Aspects of Computer Simulation of Liquid-Fueled Combustors". *J. Energy*(6).

[82] Veynante, D., and Vervisch, L., 2002. "Turbulent combustion modeling". *Progress in Energy and Combustion Science,* ***28***, pp. 193–266.

[83] Poinsot, T., and Veynante, D., 2005. *Theoretical and Numerical Combustion*, second ed. Edwards.

[84] Patankar, S., 1980. *Numerical Heat Transfer and Fluid Flow*. Hemisphere Pub. Corp. McGraw-Hill.

[85] Kohnen, G., Rüger, M., and Sommerfeld, M., 1994. "Convergence behavior for numerical calculations by the EULER/LAGRANGE Method for strongly coupled phases". *Numerical Methods in Multiphase Flows*(FED-Vol185).

[86] Liu, Z., Zheng, C., and Zhou, L., 2002. "A joint PDF model for turbulent spray evaporation/combustion". *Proceedings of the Combustion Institute,* ***29***, pp. 561–568.

[87] ANSYS Inc., 2012. ANSYS Fluent 14.5 Theory Guide, Oct.

[88] Abramzon, B., and Sirignano, W. A., 1989. "Droplet vaporization model for spray combustion calculations". *Int. J. Heat and Mass Transfer,* ***32***(9), pp. 1605–1618.

[89] Faeth, G. M., 1977. "Current status of droplet and liquid combution". *Prog. Energy Combustion Science,* ***3***, pp. 191–224.

[90] Yuen, M. C., and Chen, L. W., 1976. "On drag of evaporating liquid droplets". *Combust. Sci. Technol.,* ***14***, pp. 147–154.

[91] Miller, R. S., Harstad, K., and Bellan, J., 1998. "Evaluation of equilibrium and non-equilibrium evaporation models for many-droplet gas-liquid flow simulations". *International Journal of Multiphase Flow,* ***24***, pp. 1025–1055.

[92] Borman, G. L., and Johnson, J. H., 1962. "Unsteady vaporization histories and trajectories of fuel drops injected into swirling air". *SAE*(598C).

[93] Spalding, D., 1954. "The combustion of liquid fuels". *Proceedings of the 4th Symposium (Int.) on Combustion*, pp. 847–864.

[94] Ranz, W. E., and Marshall, W. R., 1952. "Evaporation from drops". *Chem Eng. Prog.,* ***48***, pp. 141–146.

[95] Ghassemi, H., Baek, S. W., and Khan, Q. S., 2009. "Experimental study on evaporation of kerosene droplets at elevated pressures and temperatures". *Combust. Sci. and Tech.,* ***178***, pp. 1669–1684.

[96] Burger, M., Schmehl, R., Prommersberger, K., Shäfer, O., Koch, R., and Wittig, S., 2003. "Droplet evaporation modeling by distillation curve model: accounting for kerosene fuel and elevated pressures". *International Journal of Heat and Mass Transfer,* ***46***, pp. 4403–4412.

[97] Kulick, J. D., Fessler, J. R., and Eaton, J. K., 1994. "Particle response and turbulence modification in fully-developed channel flow". *J. Fluid Mech.,* ***277***, pp. 109–134.

[98] Hardalupas, Y., Taylor, A. M. K. P., and Whitelaw, J. H., 1989. "Velocity and particle-flux characteristics of turbulent particle-laden jets". *Proceedings of the Royal Society of London A Mat,* ***426***, pp. 31–78.

[99] Amsden, A. A., O'Rourke, P. J., and Butler, T. D., 1989. *KIVA-II: A Computer Program for Chemically Reactive Flows with Sprays.* Los Alamos National Laboratory, Los Alamos, New Mexico 87545.

[100] Crowe, C. T., 2000. "On models of turbulence modulation in fluid-particle flows". *Int. J. Multiphase Flow,* ***26***, pp. 719–727.

[101] Lain, S., and Sommerfeld, M., 2002. "Turbulence modulation in dispersed two-phase flow laden with solids from a Lagrangian perspective". *Int. J. Heat and Fluid Flow.*

[102] O'Rourke, P. J., and Amsden, A. A., 1987. "The TAB Method for Numerical Calculation of Spray Droplet Breakup". *SAE Technical Paper Series*(872089).

[103] Tanner, F. X., 1997. "Liquid jet atomization and droplet breakup modeling of non-evaporating diesel fuel sprays". *SAE Technical paper*(970050).

[104] Tanner, F. X., 2004. "Development and validation of a cascade atomization and drop breakup model for high-velocity and dense sprays". *Atomization and Sprays,* ***14***(3), pp. 1–32.

[105] Kumzerova, E., and Esch, T., 2008. "Extension and validation of the CAB droplet breakup model to a wide Weber number range". *Proceedings of the ILASS-Europe 2008.*

[106] Chiu, H. H., Kim, H. Y., and Croke, E. J., 1982. "Internal group combustion of liquid droplets". *19th Symposium (International) on Combustion, The Combustion Institute*, pp. 971–980.

[107] Sirignano, W. A., 1983. "Fuel droplet vaporization and spray combustion theory". *Prog. Energy Combust. Sci.,* ***9***, pp. 291–322.

[108] Chiu, H. H., 2000. "Advances and challenges in droplet and spray combustion. I Toward a unified theory of droplet aerothermochemistry". *Progress in Energy and Combustion Science,* ***26***, pp. 381–416.

[109] Chrigui, M., Moesl, K., Ahmadi, W., and Janicka, J., 2010. "Partially premixed prevaporized kerosene spray combustion in turbulent flow". *Exp. Therm. Fluid Sci.,* ***34***(3), pp. 308–315.

[110] Gutheil, E., and Sirignano, W. A., 1998. "Counterflow Spray Combustion Modeling with Detailed Transport and Detailed Chemistry". *Combustion and Flame,* ***113***, pp. 92–105.

[111] Beck, C. H., Koch, R., and H.-J. Bauer, 2009. "Identification of droplet burning modes in lean, partially prevaporized swirl-stabilized spray flames". *Proceedings of the Combustion Institute,* ***32***, pp. 2195–2203.

[112] Collazo, J., Porteiro, J., Patiño, D., Miguez, J. L., Granada, E., and Moran, J., 2009. "Simulation and experimental validation of a methanol burner". *Fuel,* ***88***, pp. 326–334.

[113] De, S., Lakshmisha, K. N., and Bilger, R. W., 2011. "Modeling of nonreacting and reacting turbulent spray jets using a fully stochastic separated flow approach". *Combustion and FLame,* ***158***, pp. 1992–2008.

[114] Sadiki, A., Chrigui, M., Janicka, J., and Maneshkarimi, M., 2005. "Modeling and simulation of effects of turbulence on vaporization, mixing and combustion of liquid-fuel sprays". *Flow Turbul. Combust.,* ***75***, pp. 105–10.

[115] Magnussen, B. F., 1981. "On the structure of turbulence and a generalized eddy dissipation concept for chemical reaction in turbulent flow". *19th AIAA Meeting, St Louis.*

[116] Spalding, D. B., 1976. "Development of the Eddy-Break-Up model of turbulent combustion". *16th Symp. (Int.) on Combustion, The Combustion Institute.*

[117] Sommerfeld, M., and Qiu, H., 1991. "Detailed measurements in a swirling particulate two-phase flow by a phase-Doppler anemometer". *Int. Journal of Heat and Fluid Flow,* ***12***(1), pp. 20–28.

[118] Menter, F. R., 1994. "Two-Equation Eddy-Viscosity Turbulence Models for Engineering Applications". *AIAA Journal,* ***32***(8), pp. 1598–1605.

[119] Sommerfeld, M., and Qiu, H., 1993. "Characterization of particle-laden, confining swirling flows by phase-doppler anemometry and numerical calculation". *Int. Journal of Multiphase Flow,* ***19***(6), pp. 1093–1127.

[120] Sommerfeld, M., and Qiu, H., 1998. "Experimental studies of spray evaporation in turbulent flow". *Int. Journal of Heat and Fluid Flow,* ***19***, pp. 10–22.

[121] de Villiers, E., 2006. "The potential of large eddy simulation for the modeling of wall bounded flows". PhD thesis, Imperial College London.

[122] Gounder, J. D., Kourmatzis, A., and Masri, A. R., 2012. "Turbulent piloted dilute spray flames: Flow fields and droplet dynamics". *Combustion and FLame,* ***159***, pp. 3372–3397.

[123] Starner, S. H., Gounder, J., and Masri, A. R., 2005. "Effects of turbulence and carrier fluid on simple, turbulent spray jet flames". *Combustion and Flame,* ***143***, pp. 420–432.

[124] Masri, A. R., and Gounder, J. D., 2010. "Turbulent Spray Flames of Acetone and Ethanol Approaching Extinction". *Combust. Sci. Technol.,* ***182***, pp. 702–715.

[125] Scardovelli, R., and Zaleski, S., 1999. "Direct Numerical Simulation of Free-Surface and Interfacial Flow". *Ann. Rev. Fluid Mech.,* ***31***, pp. 567–603.

[126] O'Rourke, P. J., and Amsden, A. A., 1996. "A particle numerical model for wall films dynamics in port-injected engines". *SAE Fuels and Lubricants meeting, San Antonio, Texas.*

[127] Andreini, A., Bianchini, C., Facchini, B., Giusti, A., and Turrini, F., 2013. "A multi-coupled Eulerian-Lagrangian solver for airblast injectors including liquid film evolution and primary breakup - Numerical model". *Proceedings of the ILASS-Europe 2013.*

[128] Inamura, T., Shirota, M., Tsushima, M., and Kato, M., 2012. "Spray Characteristics of Prefilming Type of Airblast Atomizer". *Proceedings of the ICLASS 2012.*

[129] Rayana, B. F., Cartellier, A., and Hopfinger, E., 2006. "Assisted atomization of a liquid layer: investigation of the parameters affecting the mean drop size prediction". *Proceedings of the ICLASS 2006.*

[130] Ebner, J., Schober, P., Shäfer, O., and Wittig, S., 2003. "Modelling of Shear-Driven Liquid Wall Films on Curved Surfaces: Effect of Accelerated Air Flow and Variable Film Load". *Proceeding of the ICLASS03.*

[131] Bai, C. X., and Gosman, A. D., 1999. "Prediction of spray wall impingement in reciprocating engines". *Proceedings of the ILASS-Europe 1999.*

[132] Matsumoto, S., and Saito, S., 1970. "On the mechanism of suspension of particles in horizontal conveying: Monte Carlo simulation based on the irregular bouncing model". *J. Chem. Engng. Japan,* ***3***, pp. 83–92.

[133] Gepperth, S., Müller, A., Koch, R., and Bauer, H. J., 2012. "Ligament and Droplet Characteristics in Prefilming Airblast Atomization". *Proceedings of the ICLASS 2012.*

[134] Owen, I., and Ryley, D. J., 1985. "The flow of thin liquid films around corners". *Int. J. Multiphase Flow,* ***11***(1), pp. 51–62.

[135] Carvalho, I. S., and Heitor, M. V., 1998. "Liquid film breakup in a model of a prefilming airblast nozzle". *Experiments in Fluids,* ***24***, pp. 408–415.

[136] White, F., 1991. *Viscous Fluid Flow.* McGraw-Hill series in mechanical engineering. McGraw-Hill.

[137] Rizkalla, A. A., and Lefebvre, A. H., 1975. "The influence of air and liquid properties on airblast atomization". *Journal of Fluids Engineering,* ***97***(3), pp. 316–320.

[138] Rizk, N. K., and Lefebvre, A. H., 1980. "The influence of Liquid Film Thickness on Airblast Atomization". *Transactions of the ASME,* ***102***, pp. 706–710.

[139] El-Shanawany, M. S., and Lefebvre, A. H., 1980. "Airblast atomization: The effect of linear scale on mean drop size". *Journal of Energy,* ***4***(4), pp. 184–189.

[140] Gepperth, S., Guildenbecher, D., Koch, R., and Bauer, H. J., 2010. "Pre-filming primary atomization: Experiments and modeling". *Proceedings of the ILASS-Europe 2010.*

[141] Rizk, N. K., and Mongia, H. C., 1991. "Model for Airblast Atomization". *J. Propulsion,* ***7***(3), pp. 305–311.

[142] Bhayaraju, U., and Hassa, C., 2006. "Surface wave propagation and breakup in planar liquid sheets of prefilming airblast atomizers". *Proceedings of the ICLASS 2006.*

[143] Wollgarten, J. C., Gebretsadik, M., Zarzalis, N., Nuri Sara, Turrini, F., and Di Martino, P., 2013. "Experimental Investigation of Airblast Atomization by Variation of Dynamic Pressure and a Geometrical Scaling Factor". *Proceedings of the ILASS-Europe 2013.*

[144] Wollgarten, J. C., and Gebretsadik, M., 2013. "Private communication". *FIRST project, confidential material.*

[145] Lopez de Bertodano, M. A., C.-S. Jan, and Beus, S. G., 1997. "Annular flow entrainment rate experiment in a small vertical pipe". *Nuclear Engineering and Design,* ***178***, pp. 61–70.

[146] Dallman, J. C., Jones, B. G., and Hanratty, T. J., 1979. "Interpretation of entrainment measurements in annular gas-liquid flows". In *Two-Phase Momentum, Heat and Mass Transfer in Chemical, Process and Energy Engineering Systems*, F. Durst, G. V. Tsiklauri, and N. Afgar, eds., Vol. 2. Hemisphere, Washington DC, pp. 681–693.

[147] Kataoka, I., and Ishii, M., 1982. "Mechanism and correlation of droplet entrainment and deposition in annular two-phase flow". *NUREG/CR-2885, ANL-82-84.*

[148] Valachovic, T. G., 1993. "Numerical prediction of idle power emissions from gas turbine combustors". *Proceedings of the ASME Turbo Expo*(1993-GT-175).